We are IntechOpen,
the world's leading publisher of
Open Access books
Built by scientists, for scientists

4,800
Open access books available

122,000
International authors and editors

135M
Downloads

Our authors are among the

154
Countries delivered to

TOP 1%
most cited scientists

12.2%
Contributors from top 500 universities

BOOK
CITATION
INDEX
CLARIVATE ANALYTICS
INDEXED

WEB OF SCIENCE™

Selection of our books indexed in the Book Citation Index
in Web of Science™ Core Collection (BKCI)

Interested in publishing with us?
Contact book.department@intechopen.com

Numbers displayed above are based on latest data collected.
For more information visit www.intechopen.com

Tribological Aspects of Rolling Bearing Failures

Jürgen Gegner
SKF GmbH, Department of Material Physics
Institute of Material Science, University of Siegen
Germany

Dedicated to Dipl.-Phys. Wolfgang Nierlich on the occasion of his 70th birthday

1. Introduction

Rolling (element) bearings are referred to as *anti-friction* bearings due to the low friction and hence only slight energy loss they cause in service, especially compared to sliding or *friction* bearings. The minor wear occurring in proper operation superficially seems to suggest the question how rolling contact tribology should be of relevance to bearing failures. Satisfactorily proven throughout the 20th century primarily on small highly loaded ball bearings, the life prediction is actually based on material fatigue theories. Nonetheless, resulting subsurface spalling is usually called fatigue wear and therefore included in the discussion below. The influence of friction on the damage of rolling bearings, at first, is strikingly reflected, for instance, in foreign particle abrasion and smearing adhesion wear under improper running or lubrication conditions. On far less affected, visually intact raceways, however, temporary frictional forces can also initiate failure for common overall friction coefficients below 0.1. Larger size roller bearings with extended line contacts operating typically at low to moderate Hertzian pressure, generally speaking, are most susceptible to this surface loading. As large roller bearings are increasingly applied in the 21st century, e.g. in industrial gears, an attempt is made in the following to incorporate the rolling-sliding nature of the tribological contact into an extended bearing life model. By holding the established assumption that the stage of crack initiation still dominates the total lifetime, the consideration of the proposed competing normal stress hypothesis is deemed appropriate.

The present chapter opens with a general introduction of the subsurface and (near-) surface failure mode of rolling bearings. Due to its particular importance to the identification of the damage mechanisms, the measuring procedure and the evaluation method of the material response analysis, which is based on an X-ray diffraction residual stress determination, are described in detail. In section 4, a metal physics model of classical subsurface rolling contact fatigue is outlined. Recent experimental findings are reported that support this mechanistic approach. The accelerating effect of absorbed hydrogen on rolling contact fatigue is also in agreement with the new model and verified by applying tools of material response analysis. It uncovers a remarkable impact of serious high-frequency electric current passage through bearings in operation, previously unnoticed in the literature. Section 5 provides an overview of state-of-the-art research on mechanical and chemical damage mechanisms by tribological

stressing in rolling-sliding contact. The combined action of mixed friction and corrosion in the complex loading regime is demonstrated. Mechanical vibrations in bearing service, e.g. from adjacent machines, increase sliding in the contact area. Typical depth distributions of residual stress and X-ray diffraction peak width, which indicate microplastic deformation and (low-cycle) fatigue, are reproduced on a special rolling bearing test rig. The effect of vibrationally increased sliding friction on near-surface mechanical loading is described by a tribological contact model. Temperature rise and chemical lubricant aging are observed as well. Gray staining is interpreted as corrosion rolling contact fatigue. Material weakening by operational surface embrittlement is proven. Three mechanisms of *tribocracking* on raceways are discussed: tribochemical dissolution of nonmetallic inclusions and crack initiation by either frictional tensile stresses or shear stresses. Deep branching crack growth is driven by another variant of corrosion fatigue in rolling contact.

2. Failure modes of rolling bearings

Bearings in operation, in simple terms, experience pure rolling in elastohydrodynamic lubrication (EHL) or superimposed surface loading. With respect to the differing initiation sites of fatigue damage, a distinction is made between the classical subsurface and the (near-) surface failure mode (Muro & Tsushima, 1970). In the following simplified analysis, the evaluation of material stressing due to rolling contact (RC) loading is based on an extended static yield criterion by means of the distribution of the equivalent stress. The more complex surface failure mode, which predominates in today's engineering practice also due to the improved steelmaking processes and the tendency to use energy saving lower viscosity lubricants, comprises several damage mechanisms. Raceway indentations or boundary lubrication, for instance, respectively add edge stresses on Hertzian micro contacts and frictional sliding loading to the ideal elastohydrodynamic operating conditions.

2.1 Subsurface failure mode

The Hertz theory of elastic contact deformation between two solid bodies, specifically a rolling element and a ring of a bearing, is used to analyze the spatial stress state (Johnson, 1985). Initial yielding and generation of compressive residual stresses (CRS) is governed by the distortion energy hypothesis. In a normalized representation, Figure 1 plots the distance distributions of the three principal normal stresses σ_x, σ_y and σ_z and the resulting v. Mises equivalent stress $\sigma_e^{\text{v.Mises}}$ below the center line of a purely radially loaded frictionless elastic line contact, where the maximum normal stress, i.e. the Hertzian pressure p_0, occurs. In the coordinate trihedral, x, y and z respectively indicate the axial (lateral), tangential (overrolling) and radial (depth) direction. The v. Mises equivalent stress reaches its maximum $\sigma_{e,a}^{\max} = 0.56 \times p_0$ in a distance $z_0^{\text{v.Mises}} = 0.71 \times a$ from the surface, which is valid in good approximation for roller and ball bearings (Hooke, 2003). The load is expressed as p_0 and a stands for the semiminor axis of the contact ellipse.

As illustrated in Figure 1 for a through hardened grade ($R_{p0.2}$=const.), the v. Mises equivalent stress can locally exceed the yield strength $R_{p0.2}$ of the steel that ranges between 1400 and 1800 MPa, depending, e.g., on the heat treatment and the degree of deformation of the material (segregations) or the operating temperature. From Hertzian pressures p_0 of about 2500 to 3000 MPa, therefore, compressive residual stresses are built up. An example of a measured distance profile is shown in Figure 2a. By identifying the maximum position of the v. Mises and compressive residual stress, the Hertzian pressure is estimated to be 3500 MPa.
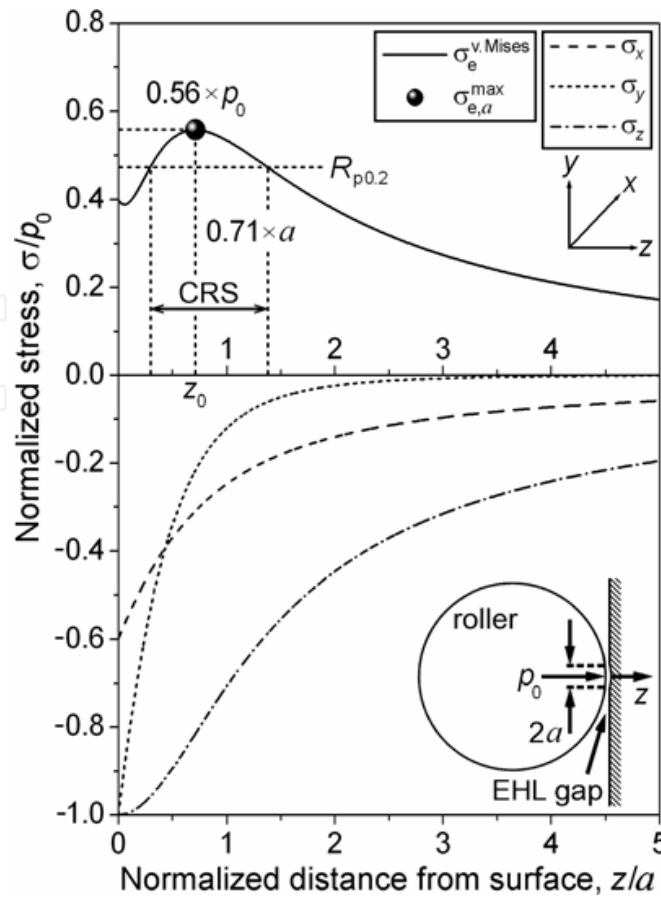
Fig. 1. Normalized plot of the depth distribution of the σ_x, σ_y, and σ_z main normal and of the v. Mises equivalent stress below the center line of the Hertzian contact area
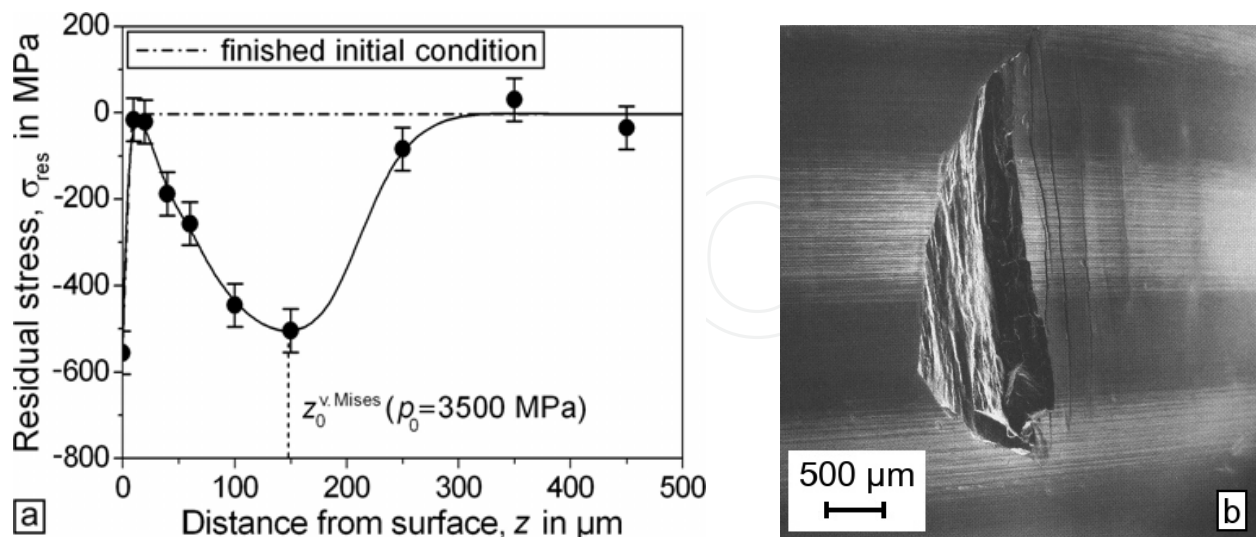

Fig. 2. Subsurface material loading and damage characterized, respectively, by (a) the residual stress distribution below the inner ring (IR) raceway of a deep groove ball bearing (DGBB) tested in an automobile gearbox rig, where the part is made of martensitically through hardened bearing steel and (b) a SEM image (secondary electron mode, SE) of fatigue spalling on the IR raceway of a rig tested DGBB with overrolling direction from left to right

Up to a depth z of 20 μm, the indicated initial state after hardening and machining is not changed, which manifests good lubrication. The residual stress is denoted by σ_{res}.

Fatigue spalling is eventually caused by subsurface crack initiation and growth to the surface in overrolling direction (OD), as evident from Figure 2b (Voskamp, 1996). In the scanning electron microscope (SEM) image, the still intact honing structure of the raceway confirms the adjusted ideal EHL conditions.

2.2 Surface failure mode

Hard (ceramic) or metallic foreign particles contaminating the lubricating gap at the contact area, however, result in indentations on the raceway due to overrolling in bearing operation. The SEM images of Figures 3a and 3b, taken in the SE mode, show examples of both types:
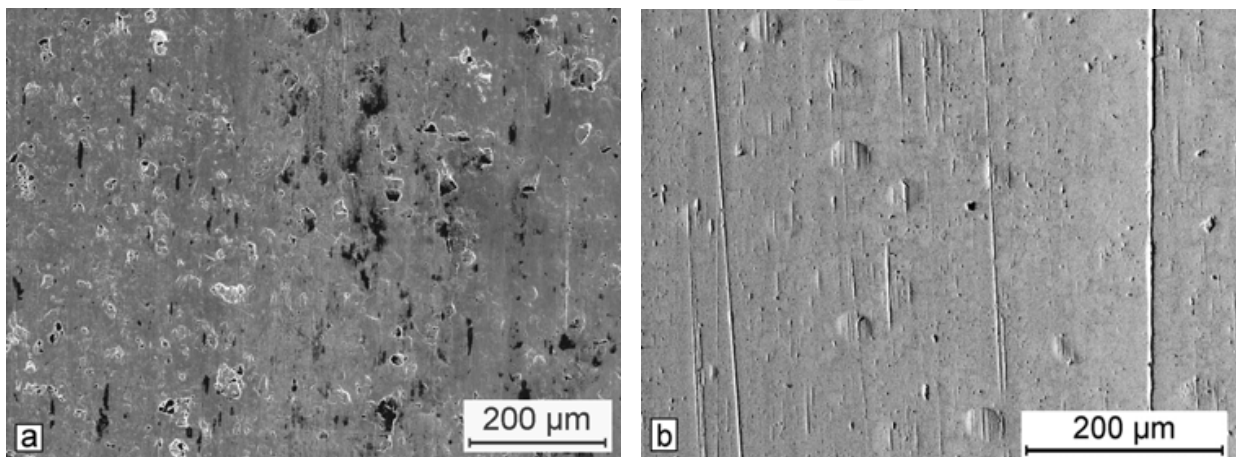

Fig. 3. SEM images (SE mode) of (a) randomly distributed dense hard particle raceway indentations (also track-like indentation patterns can occur, e.g. so-called frosty bands) from contaminated lubricant and (b) indentations of metallic particles on the smoothed IR raceway of a cylindrical roller bearing (CRB) that clearly reveal earlier surface conditions of better preserved honing structure
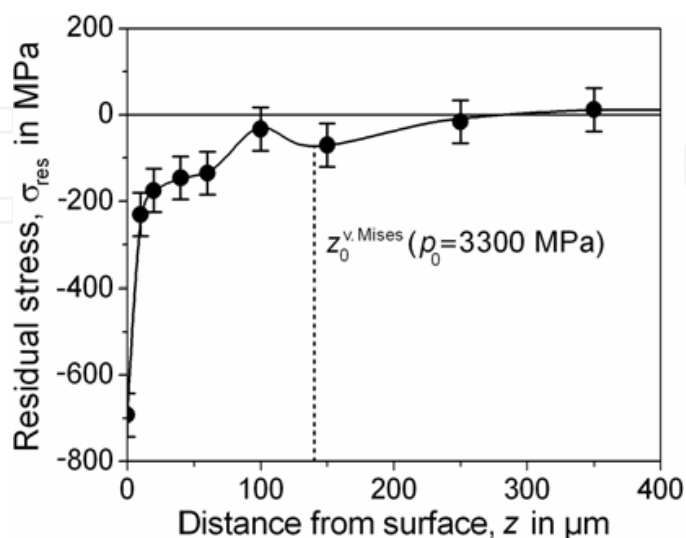

Fig. 4. Residual stress depth distribution of the martensitically hardened IR of a taper roller bearing (TRB) indicating foreign particle (e.g., wear debris) contamination of the lubricant

Cyclic loading of the Hertzian micro contacts induces continuously increasing compressive residual stresses near the surface up to a depth that is connected with the regular (e.g., lognormal) size distribution of the indentations. In the case of Figure 4, the superimposed profile modification by the basic macro contact is marginal, which means that the maximum Hertzian pressure of 3300 MPa is only applied for a short time. Compressive residual stresses in the edge zone are generated up to 60 μm depth. The high surface value reflects polishing of the raceway, associated with plastic deformation.

The stress analysis for evaluation of the v. Mises yield criterion in Figure 1 refers to the ideal undisturbed EHL rolling contact in a bearing with fully separating lubricating film, where (fluid) friction only occurs. In an extension of this scheme, the surface mode of rolling contact fatigue (RCF) is illustrated in Figure 5 on the example of indentations (size a_{micro}) that cover the raceway densely in the form of a statistical waviness at an early stage of operation:
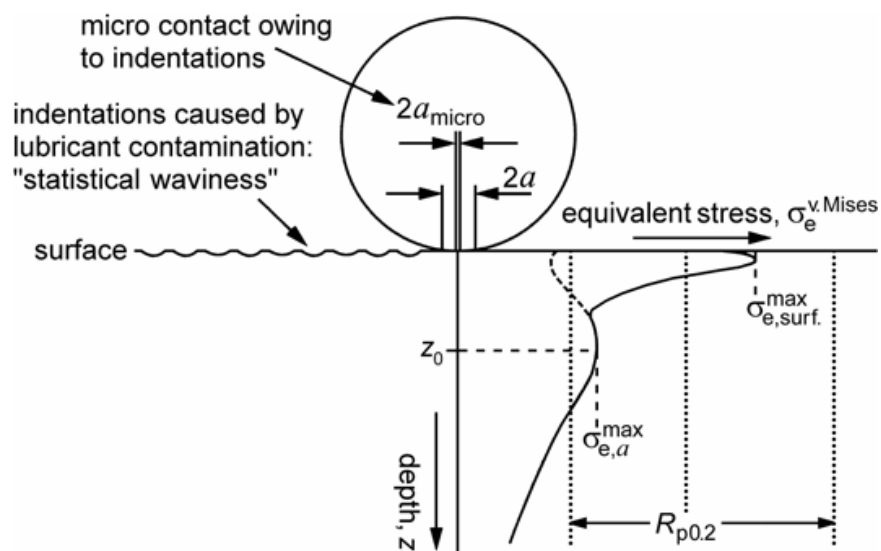

Fig. 5. Scheme of the v. Mises stress as a function of the distance from the Hertzian contact with and without raceway indentations (roller on a smaller scale)

The resulting peak of the v. Mises equivalent stress, $\sigma_{e,surf.}^{max}$, is influenced by the sharp-edged indentations of hard foreign particles (cf. Figure 3a). However, lubricant contamination by hardened steel acts most effectively because of the larger size. The contact area of the rolling elements also exhibits a statistical waviness of indentations. The stress concentrations on the edges of the Hertzian micro contacts promote material fatigue and damage initiation on or near the surface. Consequently, bearing life is reduced (Takemura & Murakami, 1998). It is shown in section 5.1 that, by creating tangential forces, additional sliding in frictional rolling contact can cause equivalent and hence residual stress distributions similar to Figures 5 and 4, respectively, on indentation-free raceways. The occurrence or dominance of the competing (near-) surface and subsurface failure mode depends on the magnitude of $\sigma_{e,surf.}^{max}$ and the relative position of the (actually not varying) yield strength $R_{p0.2}$, as indicated in Figure 5.

The ground area of an indentation is unloaded. On the highly stressed edges, the lubricating film breaks down and metal-to-metal contact results in locally most pronounced smoothing of the honing marks. Figure 6a reveals the back end of a metal span indentation in overrolling direction. Strain hardening by severe plastic deformation leads to material

embrittlement and subsequent crack initiation on the surface. Further failure development produces a so-called V pit of originally only several μm depth behind the indentation, as documented in Figure 6b. It is instructive to compare this shallow pit and the clearly smoothed raceway with the subsurface fatigue spall of Figure 2b that evolves from a depth of about 100 μm below an intact honing structure.
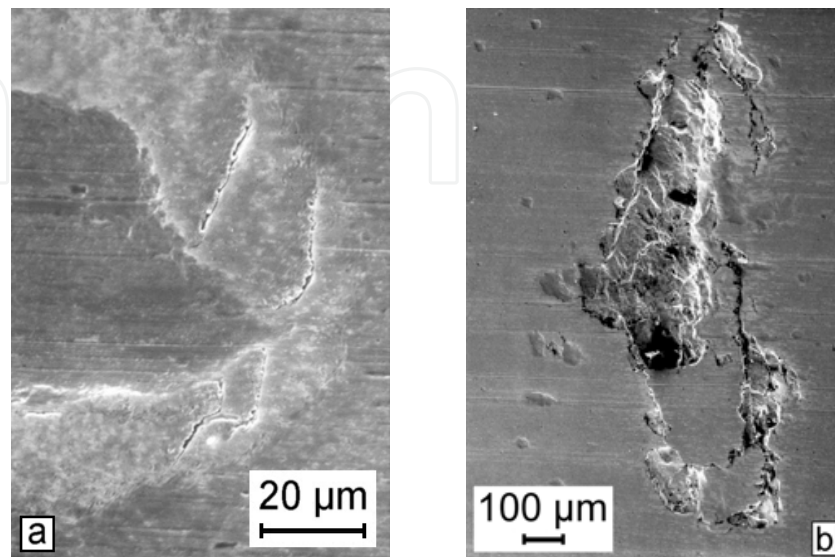

Fig. 6. SEM image (SE mode) of (a) incipient cracking and (b) beginning V pitting behind an indentation on the IR raceway of a TRB. Note the overrolling direction from left to right

3. Material based bearing performance analysis

Stressing, damage and eventually failure of a component occur due to a response of the material to the applied loading that generally acts as a combination of mechanical, chemical and thermal portions. The reliability of Hertzian contact machine elements, such as rolling bearings, gears, followers, cams or tappets, is of particular engineering significance. Advanced techniques of physical diagnostics permit the evaluation of the prevailing material condition on a microscopic scale. According to the collective impact of fatigue, friction, wear and corrosion and thus, for instance, depending on the type of lubrication, the degree of contamination, the roughness profile and the applied Hertzian pressure, failures are initiated on or below the raceway surface (see section 2). An operating rolling bearing represents a cyclically loaded tribological system. Depth resolved X-ray diffraction (XRD) measurements of macro and micro residual stresses provide an accurate estimation of the stage of material aging. The XRD material response analysis of rolling bearings is experimentally and methodologically most highly evolved. A quantitative evaluation of the changes in the residual stress distribution is proposed in the literature, for instance by integrating the depth profile to compute a characteristic deformation number (Böhmer et al., 1999). In the research reported in this chapter, however, the alternative XRD peak width based conception is used. The established procedure described in the following may be, due to its development to a powerful evaluation tool for scientific and routine engineering purposes in the SKF Material Physics laboratory under the guidance of *Wolfgang Nierlich,* referred to as the *Schweinfurt* methodology of XRD material response bearing performance analysis.

3.1 Intention and history of XRD material response analysis

The investigation aims at characterizing the response of the steel in the highly stressed edge zone to rolling contact loading. Plastification (local yielding) and material aging (defect accumulation) is estimated by the changes of the (macro) residual stresses and the XRD peak width, respectively. Failure is related to mechanical damage by fatigue and tribological loading, (tribo-) chemical and thermal exposure. Mixed friction or boundary lubrication in rolling-sliding contact is reflected, for instance, by polishing wear on the surface. The operating condition of cyclically Hertzian loaded machine parts shall be analyzed. The key focus is put on rolling bearings but also other components, like gears or camshafts, can be examined. XRD material response analysis permits the identification of the relevant failure mode. In the frequent case of surface rolling contact loading, the acting damage mechanism, such as vibrations, poor or contaminated lubrication, is also deducible. The quantitative remaining life estimation in rig test evaluation supports, for instance, product development or design optimization. This analysis option receives great interest especially in automotive engineering. Drawing a comparison with the calculated nominal life is of high significance. Also, not too heavily damaged (spalled) field returns can be investigated in the framework of failure analysis and research.

The practicable evaluation tools provided and applied in the following sections are derived from the basic research work of *Aat Voskamp* (Voskamp, 1985, 1996, 1998), who concentrates on residual stress evolution and microstructural alterations during classical subsurface rolling contact fatigue, and *Wolfgang Nierlich* (Nierlich et al., 1992; Nierlich & Gegner, 2002, 2008), who studies the surface failure mode and aligns the X-ray diffractometry technique from the 1970's on to meet industry needs. The application of the XRD line broadening for the characterization of material damage and the introduction of the peak width ratio as a quantitative measure represent the essential milestone in method development (Nierlich et al., 1992). The bearing life calibration curves for classical and surface rolling contact fatigue, deduced from rig test series, also make the connection to mechanical engineering failure analysis and design (Nierlich et al., 1992; Voskamp, 1998). The three stage model of material response allows the attribution of the residual stress and microstructure changes (Voskamp, 1985). With substantial modification on the surface (Nierlich & Gegner, 2002), this today accepted scheme proves applicable to both failure modes (Gegner, 2006a). The interdependent joint evaluation of residual stress and peak width depth profiles in the subsurface region of classical rolling contact fatigue completes the *Schweinfurt* methodology (Gegner, 2006a). Further developments of the XRD material response analysis, such as the application to other cyclically Hertzian loaded machine elements, are reported in the literature (Gegner et al., 2007; Nierlich & Gegner, 2006).

3.2 Residual stress measurement

To discuss the principles of material based bearing performance analysis, first a synopsis of the XRD measurement technique is provided. Data interpretation is subsequently described in section 3.3. The evaluation of a high number of measurements on run field and test bearings is necessary to create the appropriate scientific, engineering, and methodological foundations of XRD material response analysis. For efficient performance, the applied XRD technique must thus take into account the required fast specimen throughput at sufficient data accuracy. The rapid industrial-suited XRD measurement of residual stresses outlined below incorporates suggestions from the literature (Faninger & Wolfstieg, 1976). Usually, around ten depth positions are adequate for a profile determination. Residual stress free

material removal with high precision occurs by electrochemical polishing. The spatial resolution is given by the low penetration power of the incident X-ray radiation to about 5 μm that is appropriate for the application.

XRD residual stress analysis is widely used in bearing engineering since the 1970's (Muro et al., 1973). In the investigations of the present chapter, computer controlled Ω goniometers with scintillation type counter tube are applied, which work on the principle of the focusing Bragg-Brentano coupled θ–2θ diffraction geometry (Bragg & Bragg, 1913; Hauk & Macherauch, 1984). The X-ray source is fixed and the detector gradually rotates with twice the angular velocity $\dot{\theta}$ of the specimen to preserve a constant angle of 2θ between the incident and reflected beam.

3.2.1 High intensity diffractometer

The positions of major modifications of the conventional goniometer design are numbered consecutively in Figure 7. The severe difficulties of XRD measurements of hardened steels in the past from the broad asymmetrical diffraction lines of martensite are well known (Macherauch, 1966; Marx, 1966). Exploiting the negligible instrumental broadening, however, these large peak widths of about 5° to 7.5° only permit the implementation of such fundamental interventions in the beam path to increase the intensity of the incident and emergent X-ray radiation by tailoring the required resolution. In position 1, the square instead of the line focal spot is used. Thus, the intensity loss by vertical masking at the beam defining slit is reduced. Position 2 is also labeled in Figure 7. The distance from the horizontally and vertically adjustable defining slit to the focal spot is extended to two-thirds of the diffractometer (or measuring) circle radius. Whereas the lower resolution is of no significance, the intensity of the primary beam is further enhanced. The aperture α is indicated. The depicted scattering and Soller slits limit peak width and divergence of the diffracted beam on the expense of intensity loss. Position 3 signifies that parallelization of the radiation is dispensed with. For the same purpose, the receiving slit is opened to a
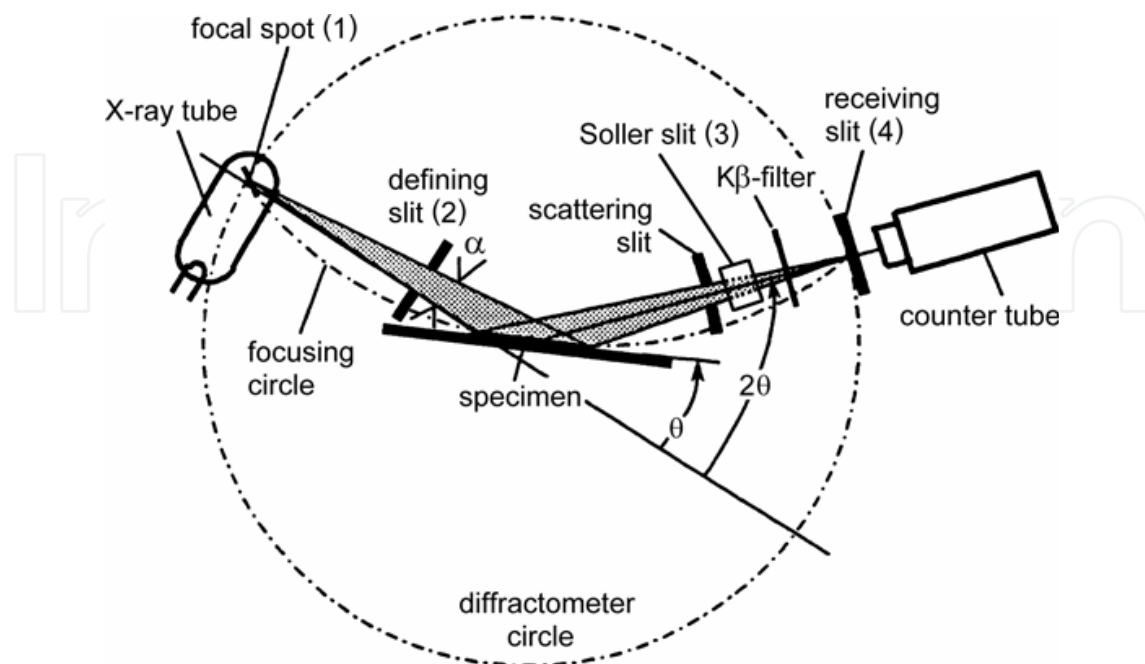

Fig. 7. Schematic diffractometer beam path with indicated modifications (1 to 4)

detection angle of 2° in position 4. The adapted diffractometer arrangement, optimized with the courage to problem-oriented simplification, eventually provides a 10 times higher recorded X-ray intensity without noticeable loss in accuracy for the broad interference lines of hardened bearing steels. The effect on determining peak position and width is negligible. The dispersion, defining the line shift relevant to residual stress evaluation, remains uninfluenced. The intensity corrections are not further discussed.

3.2.2 Implementation of the $\sin^2\psi$ method

Stress determinations are generally based on the measurement of strain (Dally & Riley, 2005). The conversion occurs by elasticity theory. Residual stresses of the first kind result in lattice strains of the order of 1‰. This elastic distortion of the unit cell causes an anisotropic peak shift of interference lines, which is determinable by the XRD technique. The macro or volume residual stresses of a polycrystalline material are derived by measuring and evaluating the relative interplanar spacing for multiple specimen orientations bringing differently oriented sets of lattice plane into reflection. Larger line shifts preferable for a more sensitive strain determination occur in the backscattering region for $2\theta>130°$, as obvious from the total differential of the Bragg condition for the monochromatic radiation:

$$\frac{\mathrm{d}D}{D} = -\cot\theta\,\mathrm{d}\theta \tag{1}$$

According to Figure 7, θ and 2θ respectively denote the glancing Bragg and the diffraction angle. Such favorable lattice spacings D of the reflecting planes increase the measuring accuracy. For martensitic or bainitic microstructures, the recorded α-Fe (211) diffraction peak, excited by the long-wave Cr Kα radiation (wavelength $\lambda=0.229$ nm), best meets this requirement with $2\theta_0=156.1°$ and is analyzable even for incomplete line detection (see Figure 8) when the rotating detector would touch the X-ray tube at $2\theta>162°$. Since its introduction in 1961 (Macherauch & Müller, 1961), the applied $\sin^2\psi$ method is further developed and, for accuracy reasons (Macherauch, 1966), predominantly used for XRD macro residual stress measurements (Hauk, 1997; Noyan & Cohen, 1987). Due to the small penetration depth of the X-ray radiation of a few µm, a biaxial stress state exists in the specimen surface in good approximation. The strain can be measured from the line shift by Eq. (1). Poisson's ratio and Young's modulus are denoted ν and E, respectively. Applying Hooke's law, elemental geometry provides the fundamental equation of X-ray residual stress analysis:

$$-(\theta-\theta_0)\cot\theta_0 = \frac{D_{\varphi,\psi}-D_0}{D_0} = \varepsilon_{\varphi,\psi} = \frac{1+\nu}{E}\sigma_\phi\sin^2\psi - \frac{\nu}{E}(\sigma_1+\sigma_2) \tag{2}$$

The azimuth and inclination Euler angles, φ and ψ, characterize the direction of the interplanar spacing $D_{\varphi,\psi}$ and the lattice strain $\varepsilon_{\varphi,\psi}$. Furthermore, σ_1 and σ_2 are the principle stresses parallel to the specimen surface ($\sigma_3=0$). The values D_0 and θ_0 refer to the strain-free undeformed lattice. For the surface stress component ($\psi=90°$) corresponding to φ, a trigonometric relationship holds:

$$\sigma_\varphi = \sigma_1\cos^2\varphi + \sigma_2\sin^2\varphi \tag{3}$$

Substituting the X-ray elastic constants (XEC):

$$\frac{1}{2}S_2 = \frac{1+\nu}{E}, \quad S_1 = -\frac{\nu}{E} \tag{4}$$

into Eq. (2) ends up with the following expression:

$$\varepsilon_{\varphi,\psi} = \frac{1}{2}S_2\sigma_\varphi \sin^2\psi + S_1\left(\sigma_1 + \sigma_2\right) \tag{5}$$

For hardened steel, isotropic grain distribution is assumed. The measurement of seven specimen tilt angles ψ from $-45°$ to $+45°$ symmetric about $\psi=0°$ in equidistant $\sin^2\psi$ steps is sufficient to reliably derive the desired σ_φ value from the slope of the straight line fitted to the data of a $D_{\varphi,\psi}$ or $\varepsilon_{\varphi,\psi}$ plot against $\sin^2\psi$ for constant φ (Nierlich & Gegner, 2008). High accuracy is already achieved by replacing D_0 with the experimental $D_{\varphi,\psi}$ at $\psi=0°$ (Voskamp, 1996). Recommendations for the X-ray elastic constants of the relevant steel microstructure are given in the literature (Hauk & Wolfstieg, 1976; Macherauch, 1966). For the XRD analyses reported in the present chapter, $\frac{1}{2}S_2=5.811\times10^{-6}$ MPa^{-1} is applied.

3.2.3 Two stage diffraction line analysis and peak maximum method

Besides X-ray intensity gain in the beam path, the second major task of rapid macro residual stress measurement is thus an efficient routine for the involved line shift evaluations. Accelerated determination of the diffraction peak position 2θ is achieved by an automated self-adjusting analysis technique tailored to the α-Fe (211) interference. The method is explained by means of Figure 8:
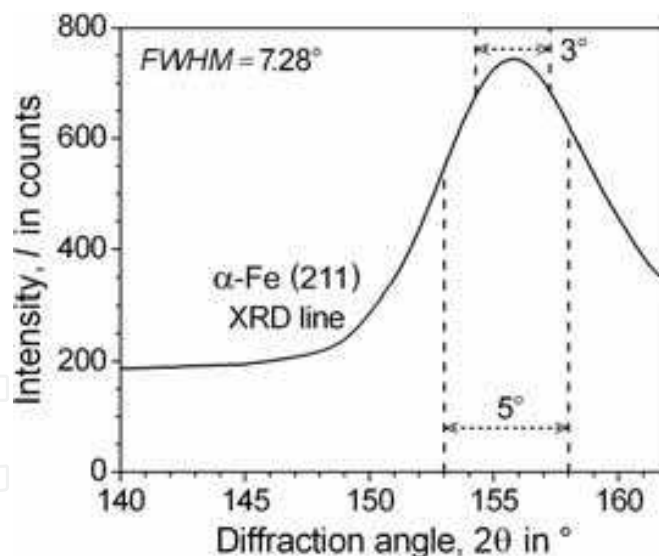

Fig. 8. Illustration of the self-developed peak finding procedure with a martensite diffraction reflex of full width at half maximum (*FWHM*) line breadth of 7.28°

The pre-measurement at reduced counting statistics across the indicated fixed angular range of 5° provides the peak maximum with an error of ±0.2°. This rough localization suffices to define appropriate symmetric evaluation points in an interval of 3° around the identified center for the subsequent highly accurate pulse controlled main run. The peak position is deduced from a fitting polynomial regression. A significant additional saving in acquisition time of 60%, compared to the standard procedure, is achieved by this skillful analysis

strategy with the modified arrangement of Figure 7, which equals the fastest up-to-date equipment also applied for the analyses in the present paper. Each individual residual stress determination on an irradiated area of 2×3 mm² takes approximately 5 min. The single measured value scatter, expressing the measurement uncertainty by the standard deviation, is found to be about ±50 MPa, as correspondingly reported elsewhere in the literature (Voskamp, 1996).

Unlike, for instance, several production processes (e.g., milling), rolling contact loading usually leads to the formation of similar depth distributions of the circumferential and axial residual stresses (Voskamp, 1987). Aside from rare exceptions such as the additional impact of severe three-dimensional vibrations (Gegner & Nierlich, 2008), deviations of maximum 20% to 30% reflect experience. As also the course of the depth profile is more important for the XRD material response analysis than the actual values of the single measurements, in the following the residual stresses are only determined in the circumferential (i.e., overrolling) direction.

3.2.4 Automated XRD peak width evaluation

Due to the geometrical restrictions of the goniometer in Figure 7, the XRD line is only collected up to a diffraction angle of 162°. The peak width, expressed as *FWHM*, is measured at a specimen tilt of $\psi=0°$ and provides information on the third kind (micro) residual stresses. For the extrapolation shown in Figure 9a, the background function is determined by a linear fit on the left of the line center. In the automated measurement procedure, the scintillation counter then moves to the onset of the diffraction peak. For the sake of simplicity, the background subtracted data of the subsequent line recoding in Figure 9b are fitted by an interpolating polynomial of high degree. The acquisition time per *FWHM* value and the measuring accuracy (one-fold standard deviation) amount to 3 to 5 min and 0.06° to 0.09°, respectively.
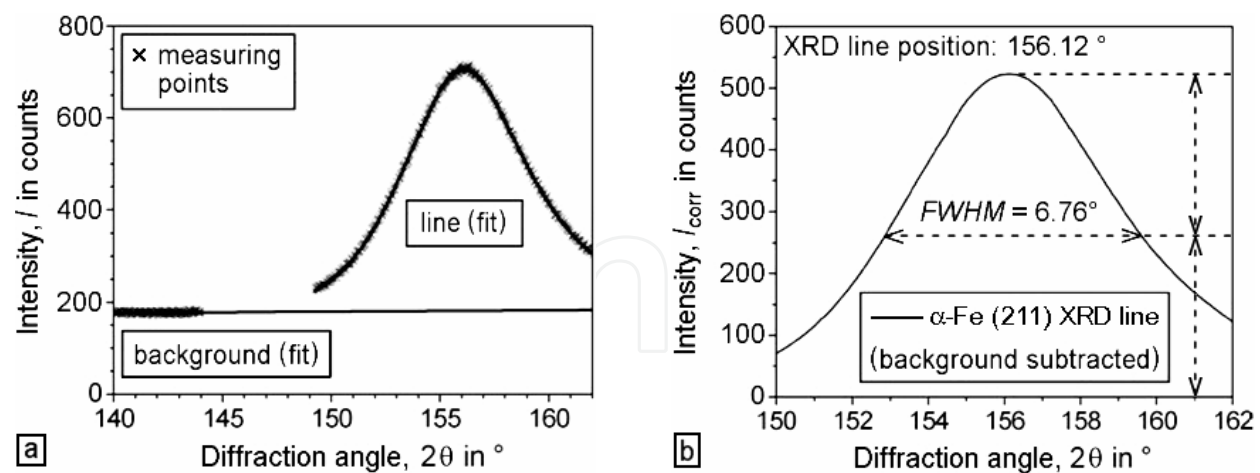

Fig. 9. Illustration of (a) the programmed XRD peak width analysis with intervals of data fitting and (b) the evaluation of the *FWHM* value for the diffraction line of Figure 9a

3.2.5 Completion of investigation methods for material response analysis

It becomes clear in the following that the reliable interpretation of the measured depth distributions of residual stresses and XRD peak width, aside from optional auxiliary retained austenite determinations to further characterize material aging (Gegner, 2006a;

Jatckak & Larson, 1980), requires supportive investigation techniques for the condition of the raceway surface, microstructure, and oil or grease. Visual inspection, failure metallography, imaging and analytical scanning electron microscopy (SEM) and infrared spectroscopy of used lubricants are employed. Concrete examples of the application of these additional examination methods in the framework of XRD based material response bearing performance analysis are also discussed extensively in the literature (Gegner, 2006a; Gegner et al., 2007; Gegner & Nierlich, 2008, 2011a, 2011b, 2011c; Nierlich et al., 1992; Nierlich & Gegner, 2002, 2006, 2008).

3.3 Evaluation methodology of XRD material response analysis

The XRD peak width based *Schweinfurt* material response analysis (MRA) provides a powerful investigation tool for run rolling bearings. An actual life calibrated estimation of the loading conditions in the (near-) surface and subsurface failure mode represents the key feature of the evaluation conception (Nierlich et al., 1992; Voskamp, 1998).

The random nature of the effect of the large number of unpredictably distributed defects in the steel indicates a statistical risk evaluation of the failure of rolling bearings (Ioannides & Harris, 1985; Lundberg & Palmgren, 1947, 1952). The Weibull lifetime distribution is suitable for machine elements. The established mechanical engineering approach to RCF deals with stress field analyses on the basis, for instance, of tensor invariants or mean values (Böhmer et al., 1999; Desimone et al., 2006). On the microscopic level, however, the material experiences strain development when exposed to cyclic loading, which suggests a quantitative evaluation of the changes in XRD peak width during operation (Nierlich et al, 1992). Disregarding the intrinsic instrumental fraction, the physical broadening of an X-ray diffraction line is connected with the microstructural condition of the analyzed material (region) by several size and strain influences (Balzar, 1999). The peak width thus represents a measuring quantity for changing properties and densities of crystal defects. Lattice distortion provides the dominating contribution to the high line broadening of hardened steels. The average dimension of the coherently diffracting domains in martensite amounts to about 100 to 200 nm. Therefore, the XRD peak width is not directly correlated with the prior austenite grain size of few μm. The observed reduction of the line broadening by plastic deformation signifies a decrease of the lattice distortion. The minimum XRD peak width ratio, b/B, is the calibrated damage parameter of rolling contact fatigue that links materials to mechanical engineering (Weibull) failure analysis. The derived XRD equivalent values of the actual (experimental) L_{10} life at 90% survival probability (rating reliability) of a bearing population equal about 0.64 for the subsurface as well as 0.83 and 0.86, respectively for ball and roller bearings, for the surface mode of RCF (Gegner, 2006a; Gegner et al., 2007; Nierlich et al., 1992; Voskamp, 1998). Figures 10 and 11 display b/B data from calibrating rig tests. Here, b and B respectively denote the minimum *FWHM* in the depth region relevant to the considered (subsurface or near-surface) failure mode and the initial *FWHM* value. B is taken approximately in the core of the material or can be measured separately, e.g. below the shoulder of an examined bearing ring. The correlation between the statistical parameters representing a population of bearings under certain operation conditions and the state of aging damage (fatigue) of the steel matrix by the XRD peak width ratio measured on an accidentally selected part also reflects the intrinsic determinateness behind the randomness.

Based on Voskamp's three stage model for the subsurface and its extension to the surface failure mode (Gegner, 2006a; Voskamp, 1985, 1996), Figures 10 and 11 schematically illustrate
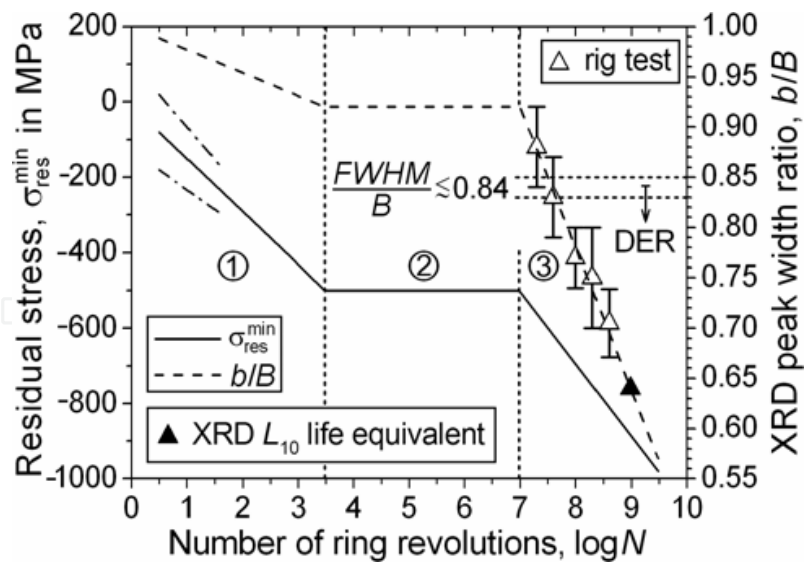
Fig. 10. Three stage model of subsurface RCF with XRD peak width ratio based indication of dark etching region (DER) formation in the microstructure and L_{10} life calibration (DGBB)
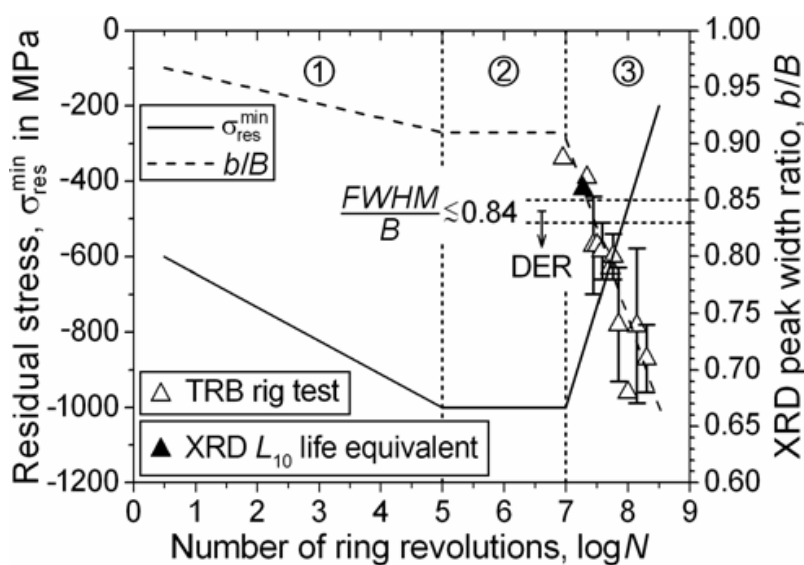

Fig. 11. Three stage model of surface RCF with XRD peak width ratio based DER indication and actual L_{10} life calibration (roller bearings) that refers to the higher loaded inner ring

the progress of material loading in rolling contact fatigue with running time, expressed by the number N of inner ring revolutions. The changes are best described by the development of the maximum compressive residual stress, σ_{res}^{min}, and the RCF damage parameter, b/B, measured respectively in the depth and on (or near) the surface. The underlying alterations of the $\sigma_{res}(z)$ and $FWHM(z)$ distributions are demonstrated in Figure 12 for competing failure modes. The characteristic values are indicated in the profiles that in the subsurface region of classical RCF reveal an asymmetry towards higher depths (cf. Figure 1). The response of the steel to rolling contact loading is divided into the three stages of mechanical conditioning shakedown (1), damage incubation steady state (2), and material softening instability (3). Figures 10 to 12 provide schematic illustrations. The prevalently observed re-reduction of the compressive residual stresses in the instability phase of the surface mode, particularly

typical of mixed friction running conditions, suggests relaxation processes. From experience, a residual stress limit of about –200 MPa is usually not exceeded, as included in the diagrams of Figures 11 and 12. The conventional logarithmic plot overemphasizes the differences in the slopes between the constant and the decreasing curves in the steady state and the instability stage of Figures 10 and 11. The existence of a third phase, however, is indicated by the reversal of the residual stress on the surface (cf. Figures 11 and 12) and also found in RCF component rig tests (Rollmann, 2000).

The first stage of shakedown is characterized by microplastic deformation and the quick build-up of compressive residual stresses when the yield strength, $R_{p0.2}$, of the hardened steel is locally exceeded by the v. Mises equivalent stress representing the triaxial stress field in rolling contact loading (cf. section 2). Short-cycle cold working processes of dislocation rearrangement with material alteration restricted to the higher fatigue endurance limit, in which carbon diffusion is not involved, cause rapid mechanical conditioning (Nierlich & Gegner, 2008). Further details are discussed in section 4.2. The second stage of steady state arises as long as the applied load falls below the shakedown limit so that ratcheting is avoided (Johnson & Jefferis, 1963; Voskamp, 1996; Yhland, 1983). In this period of fatigue damage incubation, no significant microstructure, residual stress and XRD peak width alterations are observed. Elastic behavior of the pre-conditioned microstrained material is assumed. In the extended final instability stage, gradual microstructure changes occur (Voskamp, 1996). The phase transformations require diffusive redistribution of carbon on a micro scale, which is assisted by plastification. From $FWHM/B$ of about 0.83 to 0.85 downwards, a dark etching region (DER) occurs in the microstructure by martensite decay. Note that this is in the range of the XRD L_{10} value for the surface failure mode but well before this life equivalent is reached for subsurface RCF (cf. Figures 11 and 12).
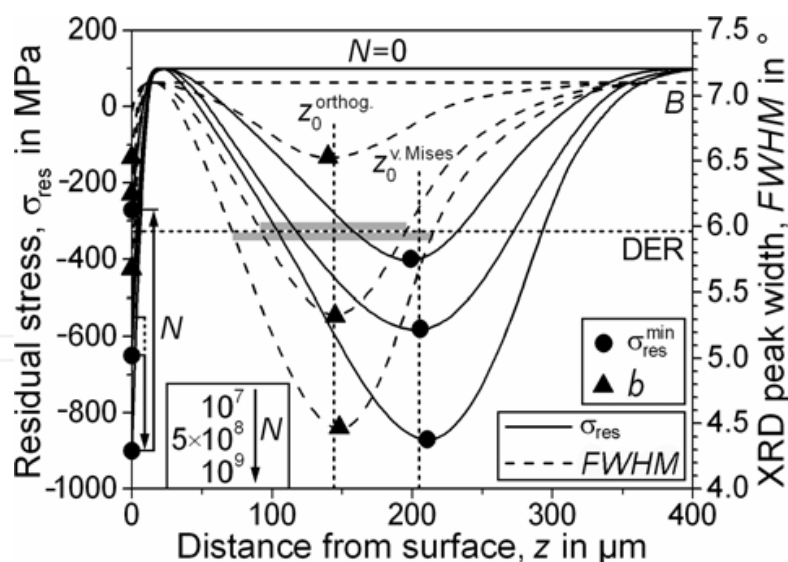

Fig. 12. Schematic residual stress and XRD peak width change with rising N during subsurface and surface RCF and prediction of the respective depth ranges (gray) of DER formation

Fatigue is damage (defect) accumulation under cyclic loading. Microplastic deformation is reflected in the XRD line broadening. The observed reduction of the peak width signifies a decrease of the lattice distortion. For describing subsurface RCF failure, the established Lundberg-Palmgren bearing life theory defines the risk volume of damage initiation on microstructural defects by the effect of an alternating load, thus referring to the depth of

maximum orthogonal shear stress (Lundberg & Palmgren, 1947, 1952). However, the v. Mises equivalent stress, by which residual stress formation is governed, as well as each principal normal stress (cf. Figure 1) are pulsating in time. In the region of classical RCF below the raceway, the minimum XRD peak width occurs significantly closer to the surface than the maximum compressive residual stress (Gegner & Nierlich, 2011b; Schlicht et al., 1987). It is discussed in the literature which material failure hypothesis is best suited for predicting RCF loading (Gohar, 2001; Harris, 2001): Lundberg and Palmgren use the orthogonal shear stress approach but other authors prefer the Huber-von Mises-Hencky distortion or deformation energy hypothesis (Broszeit et al., 1986). The well-founded conclusion from the XRD material response analyses interconnects both views in a kind of paradox (Gegner, 2006a): whereas residual stress formation and the beginning of plastification conform to the distortion energy hypothesis, RCF material aging and damage evolution in the steel matrix, manifested in the XRD peak width reduction, responds to the alternating orthogonal shear stress.

The detected location of highest damage of the steel matrix agrees with the observation that under ideal EHL rolling contact loading most fatigue cracks are initiated near the $z_0^{\text{orthog.}}$ depth (Lundberg & Palmgren, 1947). It is recently reported that the frequency of fracturing of sulfide inclusions in bearing operation due to the influence of the subsurface compressive stress field also correlates well with the distance distribution of the orthogonal shear stress below the raceway (Brückner et al., 2011). The three stages of the associated mechanism of butterfly formation, which occurs from a Hertzian pressure of about 1400 MPa, are documented in Figure 13: fracturing of the MnS inclusion (1), microcrack extension into the bulk material (2), development of a white etching wing microstructure along the crack (3). The light optical micrograph (LOM) and SEM image of Figures 14a and 14b, respectively, reveal in a radial (i.e., circumferential) microsection how the white etching area (WEA) of the butterfly wing virtually *emanates* from the matrix zone in contact with the pore like material separation of the initially fractured MnS inclusion into the surrounding steel microstructure.
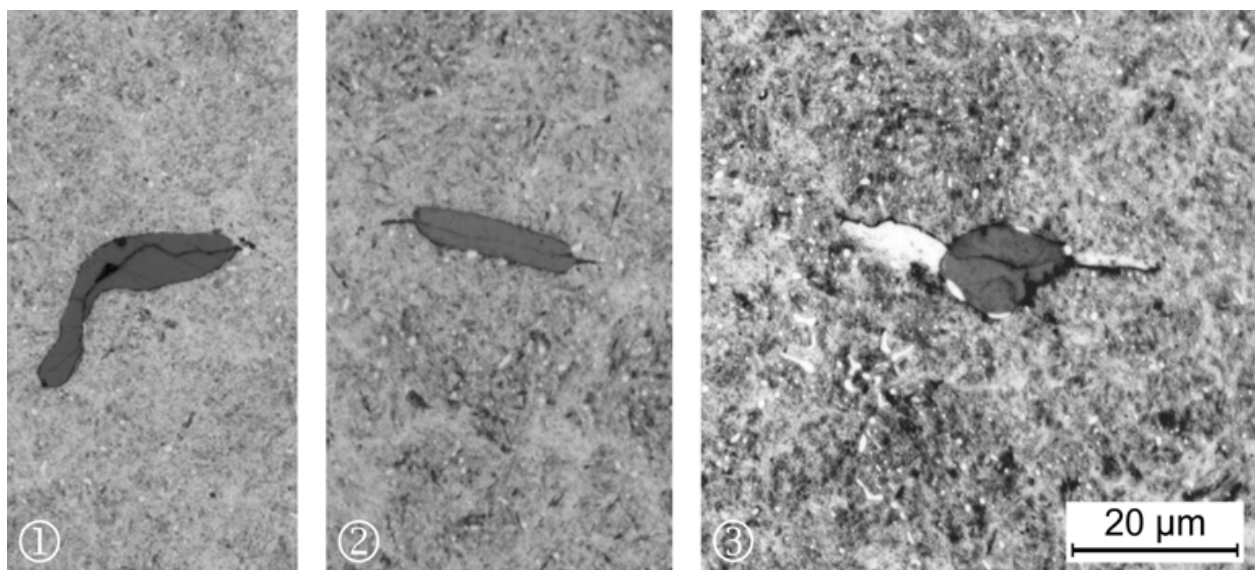

Fig. 13. Butterfly formation on sulfide inclusions observed in etched axial microsections of the outer ring of a CRB of an industrial gearbox after a passed rig test at p_0=1450 MPa

Butterflies become relevant in the upper bearing life range above L_{10}. Inclusions of different chemical composition, shape, size, mechanical properties and surrounding residual stresses are technically unavoidable in steels from the manufacturing process. The potential for their reduction is limited also from an economic viewpoint and virtually fully tapped in the today's high cleanliness bearing grades. Local peak stresses on nonmetallic inclusions, i.e. internal metallurgical notches, below the contact surface can cause the initiation of microcracks. Operational fracture of embedded MnS particles (see Figures 13, 14) is quite often observed and represents a potential butterfly formation mechanism besides, e.g., decohesion of the interphase (Brückner et al., 2011). Subsequent fatigue crack propagation is driven by the acting main shear stress (Schlicht et al., 1987, 1988; Takemura & Murakami, 1995). The growing butterfly wings thus follow the direction of ideally 45° to the raceway tangent. Figure 15 shows a textbook example from a weaving machine gearbox bearing at around the nominal L_{50} life. The overrolling direction in the micrograph is from right to left. The white etching constituents show an extreme hardness of about 75 HRC (1200 HV) and consist of carbide-free nearly amorphous to nano-granular ferrite with grain sizes up to 20 to 30 nm.
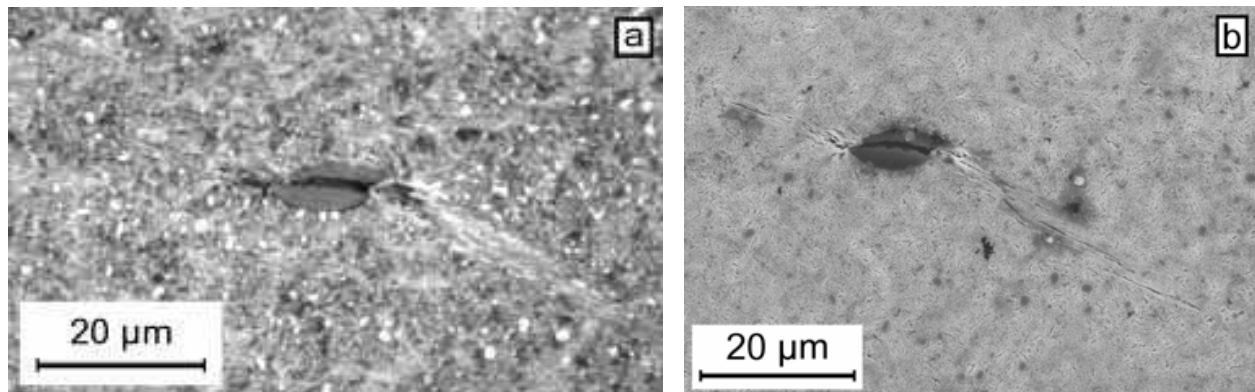

Fig. 14. LOM micrograph (a) and corresponding SEM-SE image (b) of butterfly development on a cracked MnS inclusion in the etched radial microsection of the stationary outer ring of a spherical roller bearing (SRB) after a passed rig test at a Hertzian pressure p_0 of 2400 MPa
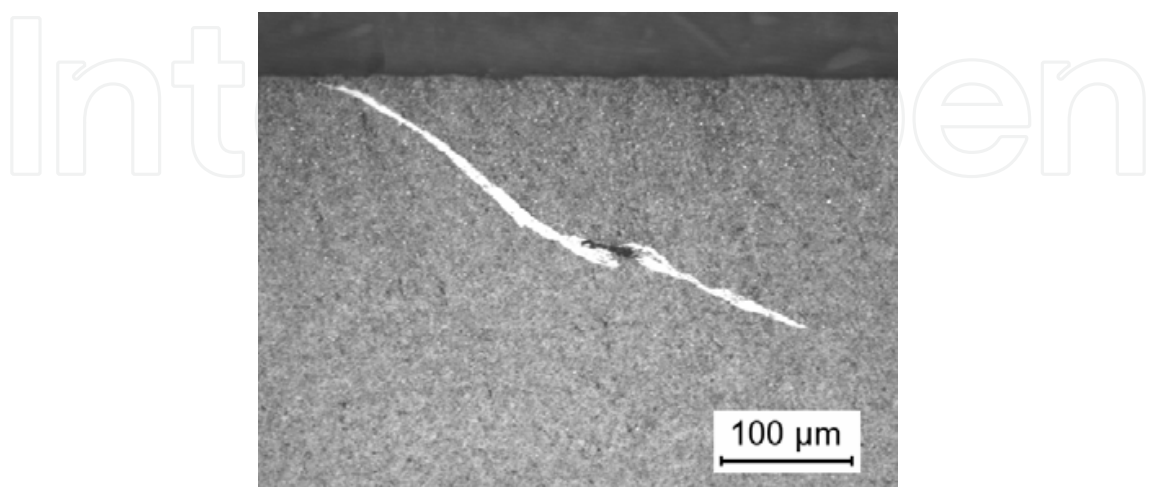

Fig. 15. Butterfly wing growth from the depth to the raceway surface in overrolling direction (right-to-left) in the etched radial microsection of the IR of a CRB loaded at p_0=1800 MPa

Critical butterfly wing growth up to the surface (see Figure 15), which leads to bearing failure by raceway spalling eventually, occurs very rarely (Schreiber, 1992). The metallurgically unweakened steel matrix in some distance to the inclusion can cause crack arrest. Multiple damage initiation, however, is found in the final stage of rolling contact fatigue. Subsurface cracks may then reach the raceway (Voskamp, 1996). Butterfly RCF damage develops by the microstructural transformation of low-temperature dynamic recrystallization of the highly strained regions along cracks rapidly initiated on stress raising nonmetallic inclusions in the steel (Böhm et al., 1975; Brückner et al., 2011; Furumura et al., 1993; Österlund et al., 1982; Schlicht et al., 1987; Voskamp, 1996), If this localized fatigue process occurs at Hertzian pressures below 2500 MPa (Brückner et al., 2011; Vincent et al., 1998), it is not recognizable alone by an XRD analysis that is sensitive to integral material loading (see section 3.2).

According to the Hertz theory, the depth $z_0^{\mathrm{orthog.}}$ of the maximum of the alternating orthogonal shear stress and its double amplitude depend on the footprint ratio between the semiminor and the semimajor axis of the pressure ellipse (Harris, 2001; Palmgren, 1964): the values respectively amount to $0.5 \times a$ and $0.5 \times p_0$ in line contact and are slightly lower for ball bearings. From $z_0^{\mathrm{orthog.}} = 0.5 \times a < z_0^{\mathrm{v.Mises}}$ follows that the *FWHM* distance curve reaches its minimum b significantly closer to the surface than the residual stresses, as it is illustrated in Figure 12 and apparent from the practical example of Figure 16a. This finding is exploited for XRD material response analysis (Gegner, 2006a). The residual stress and XRD peak width distributions are evaluated jointly in the subsurface region of classical rolling contact fatigue by applying the v. Mises and orthogonal shear stress interdependently. Data analysis is demonstrated in Figures 16a and 16b. Adjusting to the best fit improves the accuracy of deducing the Hertzian pressure p_0 from the measured profiles. Superposition with the load stresses results in a slight gradual shift of the residual stress and XRD peak width distribution to larger depths with run duration (Voskamp, 1996), which is neglected in the evaluation (see Figure 12). In the example of Figure 16a, material aging is within the scattering range of the L_{10} life equivalent value for both, thus in this case competing, failure
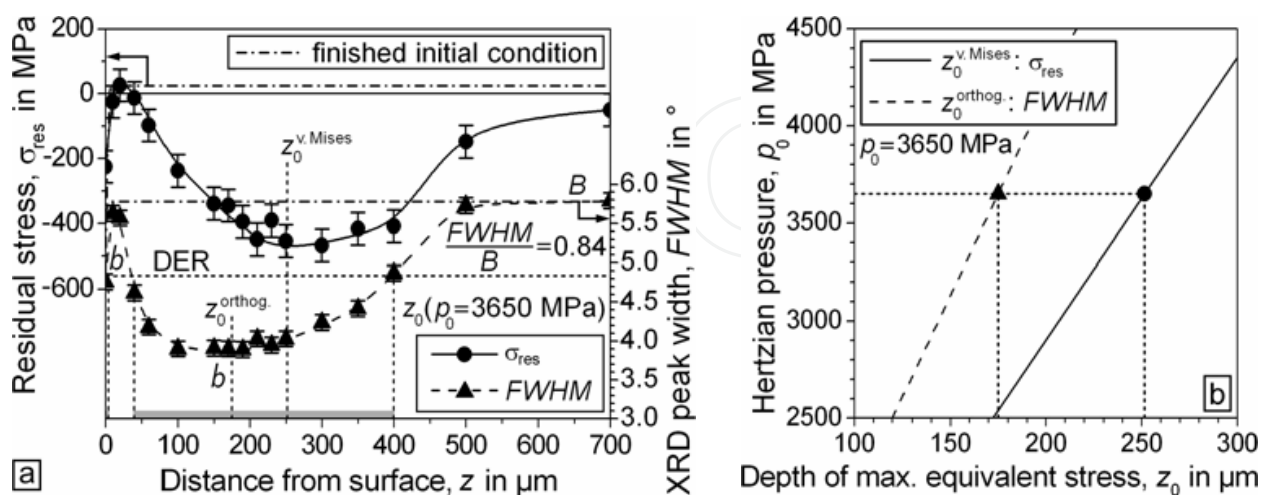

Fig. 16. Graphical representation of (a) the residual stress and XRD peak width depth distribution measured below the IR raceway of a DGBB tested in an automobile gearbox rig with indication of the initial as-delivered condition and (b) the joint subsurface profile evaluation

modes of surface ($b/B\approx0.83$) and subsurface RCF ($b/B\approx0.64$): a relative XRD peak width reduction of $b/B\geq0.82$ and $b/B=0.67$ is respectively taken from the diagram. The greater-or-equal sign for the estimation of the surface failure mode considers the unknown small *FWHM* decrease on the raceway due to grinding and honing of the hardened steel in the as-finished condition (see Figures 12 and 16a) so that the alternatively used reference *B* in the core of the material or another uninfluenced region (e.g., below the shoulder of a bearing ring) exceeds the actual initial value at *z*=0 typically by about 0.02°. The original residual stress and XRD peak width level below the edge zone results from the heat treatment. The inner ring of Figure 16a, for instance, is made out of martensitically through hardened bearing steel.

The predicted dark etching regions at the surface and in a depth between 40 and 400 µm are well confirmed by failure metallography, as evident from a comparison of Figure 16a with Figures 17a and 17b. The DER-free intermediate layer is clearly visible in the overview micrograph. The dark etching region near the surface ranges to about 10 to 12 µm depth.
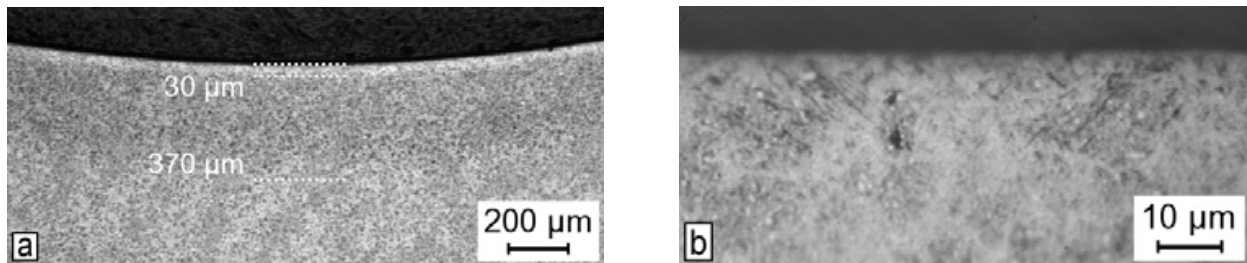

Fig. 17. LOM images of (a) the etched axial microsection of the inner ring of Figure 16a with evaluation of the extended subsurface DER and (b) a detail revealing the near-surface DER

4. Subsurface rolling contact fatigue

Since the historical beginnings with *August Wöhler* in the middle of the 19th century, today's research on material fatigue can draw from extensive experiences. Cyclic stressing in rolling contact, however, even eludes a theoretical description based on advanced multiaxial damage criteria, such as the Dang Van critical plane approach (Ciavarella et al., 2006; Desimone et al., 2006). Although little noticed in the young research field of very high cycle fatigue (VHCF) so far, RCF is the most important type of VHCF in engineering practice. Complex VHCF conditions occur under rapid load changes. The inhomogeneous triaxial stress state exhibits a large fraction of hydrostatic pressure $p_h=-(\sigma_x+\sigma_y+\sigma_z)/3$ (see Figure 1, maximum on the surface) and, in the ideal case of pure radial force transfer, no critical tensile stresses, which is favorable to brittle materials and makes the hardened steel behave ductilely. The number of cycles to failure defining the rolling bearing life is thus by orders of magnitude larger than in comparable push-pull or rotating bending loading (Voskamp, 1996). The RCF performance of hardened steels is difficult to predict. Fatigue damage evolution by gradual accumulation of microplasticity is associated with increasing probability of crack initiation and failure. Microstructural changes during RCF are usually evaluated as a function of the number of ring revolutions (Voskamp, 1996). For the scaled comparison of differently loaded bearings, however, the material inherent RCF progress measure of the minimum XRD peak width ratio, b/B, is more appropriate as it correlates with the statistical parameters of the Weibull life distribution of a fictive lot (see section 3.3).

The influence of hydrogen on rolling contact fatigue is also quantifiable this way, as applied to classical RCF in section 4.3.

4.1 Microstructural changes during subsurface rolling contact fatigue

The characteristic subsurface microstructural alterations in hardened bearing steels occur due to shear induced carbon diffusion mediated phase transformations (Voskamp, 1996), for which a mechanistic metal physics model is introduced in the following. The local material fatigue aging of butterfly formation is already discussed in section 3.3. In Figures 18a to 18c, the XRD material response analysis of a rig tested automobile gearbox ball bearing is evaluated in the region of subsurface RCF. A Hertzian pressure of 3400 MPa is deduced. The joint interdependent profile evaluation is shown in Figure 18b. At the found relative decrease of the X-ray diffraction peak width to $b/B \approx 0.71$, i.e. still above the XRD L_{10} life equivalent value of roughly 0.64, rolling contact fatigue produces a distinct DER in the microstructure in the depth range predicted by the $FWHM/B$ reduction below 0.84 (cf., Figures 10, 12 and 17a). This exact agreement is emphasized by a comparison of Figures 18a and 18c.
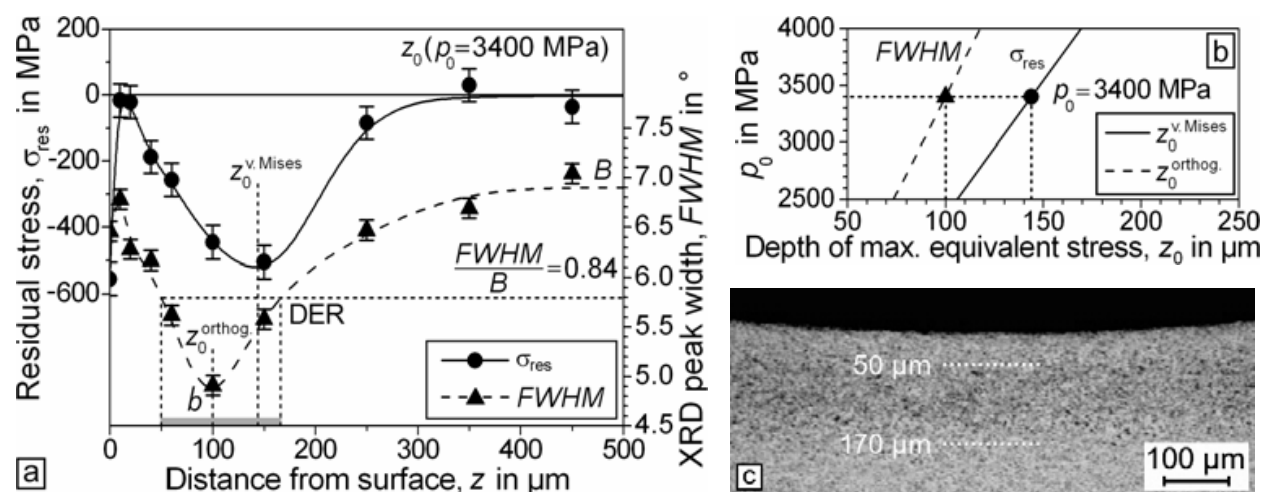
Fig. 18. Subsurface RCF analysis of the IR of a run DGBB including (a) the measured depth distribution of residual stress and XRD peak width ($b/B \approx 0.71$) with DER prediction, (b) the joint XRD profile evaluation and (c) an etched axial microsection with actual DER extension

Spatial differences in the etching behavior of the bearing steel matrix in metallographic microsections caused by high shear stresses below the raceway surface after a certain stage of material aging by cyclic rolling contact loading are known since 1946 (Jones, 1946). The localized weakening structural changes result from stress induced gradual partial decay of martensite into heavily plasticized ferrite, the development of regular deformation slip bands and alterations in the carbide morphology (Schlicht et al., 1987; Voskamp, 1996). Due to the appearance of the damaged zones after metallographic preparation in an optical microscope, these areas are referred to as dark etching regions (Swahn et al., 1976a). The small decrease in specific volume of less than 1% by martensite decomposition results in a tensile contribution to operational residual stress formation but the effects of opposed austenite decay and local yield strength reduction by phase transformation prevail (Voskamp, 1996). Recent reheating experiments also point to diffusion reallocation of carbon atoms from (partially) dissolving temper as well as globular carbides for dislocational

segregation in severely deformed regions (Gegner et al., 2009), which is assumed to be inducible by cyclic material loading in rolling contact (see section 4.2).

The overall quite uniformly appearing DER (see Figures 17a and 18c) is displayed at higher magnification in the LOM micrograph of Figure 19a. On the micrometer scale, affected dark etching material evidently occurs locally preferred in zones of dense secondary cementite. As well as the spatial and size distribution of the precipitation hardening carbides, micro-segregations (e.g., C, Cr) influence the formation of the DER spots.

Subsurface fatigue cracks usually advance in circumferential, i.e. overrolling, direction parallel to the raceway tangent in the early stage of their propagation (Lundberg & Palmgren, 1947), as exemplified in Figure 19b (Voskamp, 1996). The aged matrix material of the dark etching region exhibits embrittlement (see also section 5.5) that is most pronounced around the depth of maximum orthogonal shear stress, where the indicative X-ray diffraction line width is minimal and the microstructure reveals intense response to the damage sensitive preparative chemical etching process.
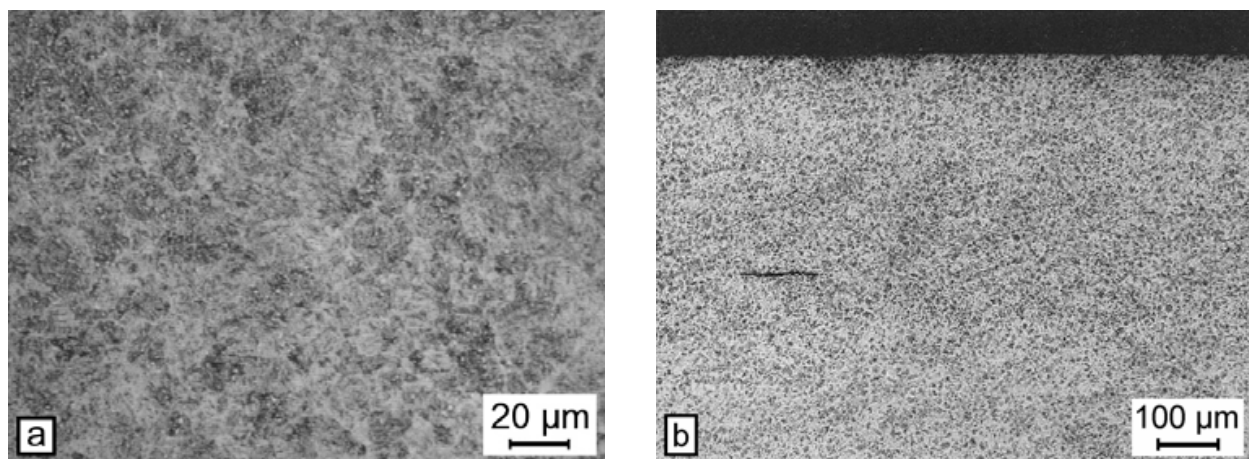
Fig. 19. LOM micrographs of (a) a detail of the DER of Figure 17a and (b) typical subsurface fatigue crack propagation parallel to the raceway around the depth of maximum orthogonal shear stress in the etched radial microsection of the inner ring of a deep groove ball bearing

In the upper subsurface RCF life range of the instability stage above the XRD L_{10} equivalent value, i.e. $b/B < 0.64$ according to Figure 10, shear localization and dynamic recrystallization (DRX) induce (100)[110] and (111)[211] rolling textures that reflect the balance of plastic deformation and DRX (Voskamp, 1996). Regular flat white etching bands (WEB) of elongated parallel carbide-free ferritic stripes of inclination angles β_f of 20° to 32° to the raceway tangent in overrolling direction occur inside the DER (Lindahl & Österlund, 1982; Swahn et al., 1976a, 1976b; Voskamp, 1996). For the automobile alternator and gearbox ball bearing from rig tests, N° 1 and N° 2 in Figure 20a, respectively, b/B equals about 0.61 and 0.57. Metallography of the investigated inner rings in Figures 20b and 20c confirms the dark etching region predicted by the relative XRD peak width reduction and indicates the discoid flat white bands (FWB) in the axial (N° 1) and radial microsection (N° 2).

Ferrite of the FWB is surrounded by reprecipitated highly carbon-rich carbides and remaining martensite (Lindahl & Österlund, 1982; Swahn et al., 1976a, 1976b). Note that the carbides originally dispersed in the hardened steel are dissolved in the WEB under the influence of the RCF damage mechanism (see section 4.2). The SEM images of Figures 21a and 21b imply that the aged DER microstructure, the embrittlement of which is reflected in
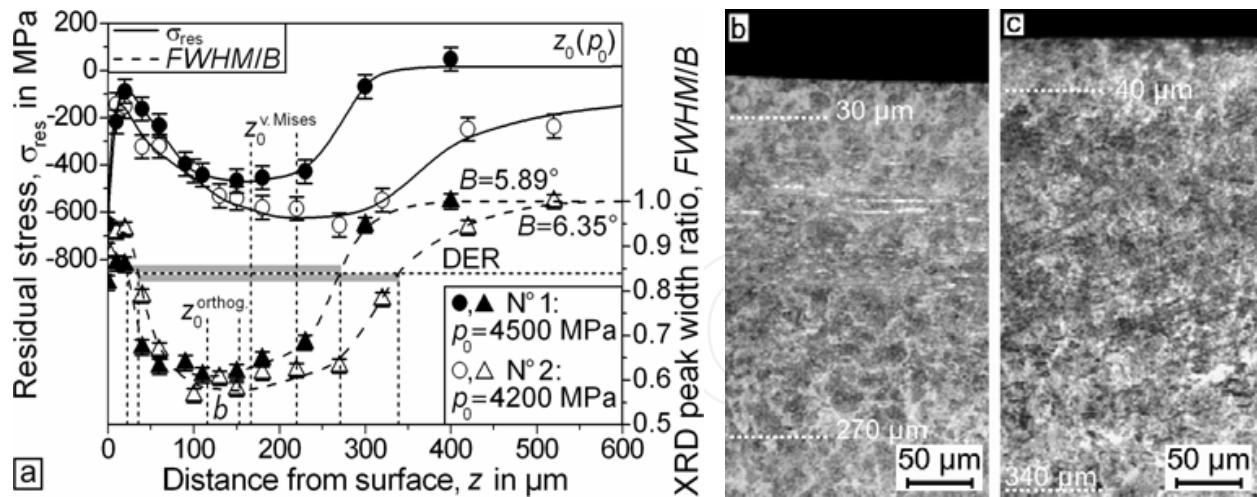
Fig. 20. Subsurface RCF analysis of the IR of two run DGBB (N° 1, N° 2) including (a) the evaluated depth distribution of residual stress and XRD peak width (N° 1: $b/B \approx 0.61$, N° 2: $b/B \approx 0.57$, the given B values reflect different tempering temperature of martensite hardening of bearing steel) with DER prediction, (b) an etched axial microsection of IR-N° 1 and (c) an etched radial microsection of IR-N° 2, respectively with DER indication and visible FWB
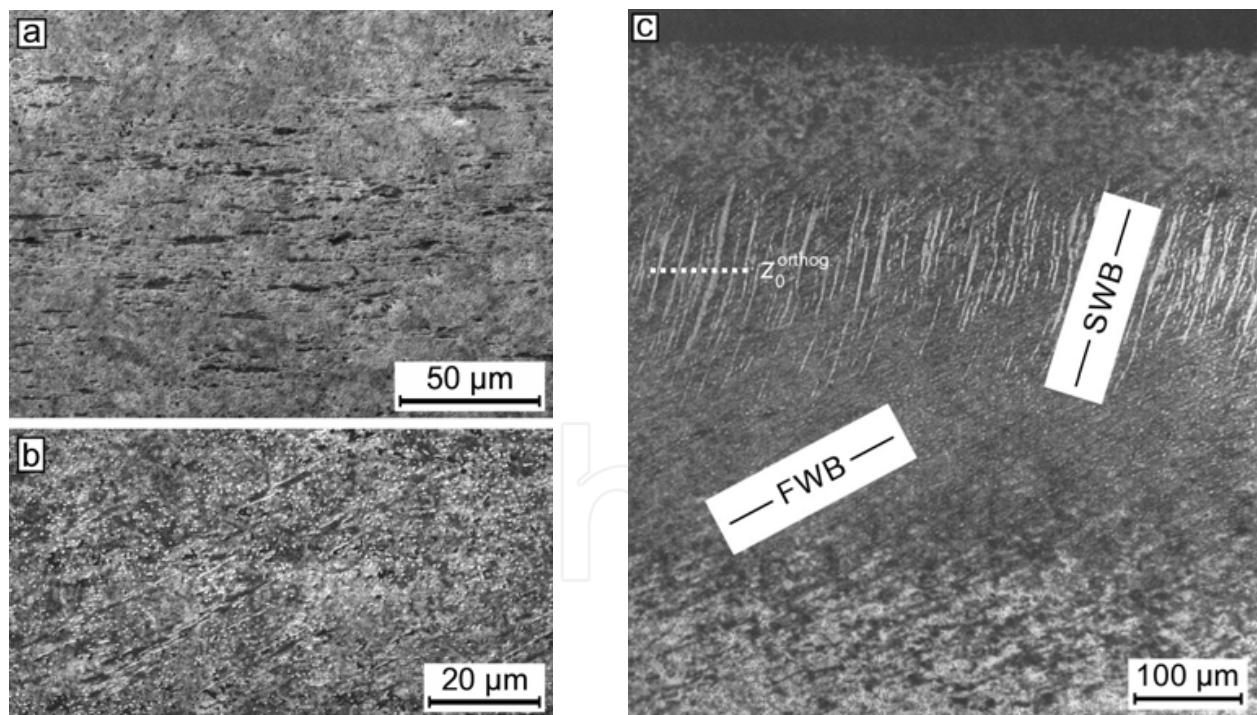

Fig. 21. SEM-SE detail of (a) Figure 20b (preparatively initiated cracks expose the DER) and (b) Figure 20c ($\beta_f = 22°$) and (c) an etched radial microsection of the IR of a DGBB rig tested at a Hertzian pressure of 3700 MPa with indicated depth of maximum orthogonal shear stress

the preparatively lacerated material from the chemical attack by the etching process, acts as precursor of WEB formation (dark appearing phase, SEM-SE). The angles β_f are determined

to be 29° and 22° (see Figures 20c, 21b) for the inner ring of bearing N° 1 and N° 2, respectively. Texture development as initiating step of WEA evolution is suggested. Steep white bands (SWB) as shown in Figure 21c occur at an advanced RCF state, once a critical FWB density is reached, not until the actual L_{50} life (Voskamp, 1996), which amounts to 5.54×L_{10} for ball bearings with a typical Weibull modulus of 1.1. The inclination β_s of 75° to 85° to the raceway in overrolling direction again relates to the stress field. The included angle β_{s-f} between the FWB (30°-WEB) and the SWB (80°-WEB) thus equals about 50°. Note that in Figures 20c, 21b and 21 c, the overrolling direction is respectively from left to right. FWB appear weaker in the etched microstructure. The hardness loss is due to the increasing ferrite content. SWB reveal larger thickness and mutual spacing. The ribbon-like shaped carbide-free ferrite is highly plastically deformed (Gentile et al., 1965; Swahn et al., 1976a, 1976b; Voskamp, 1996).

4.2 Metal physics model of rolling contact fatigue and experimental verification

The classical Lundberg-Palmgren bearing life theory is empirical in nature (Lundberg & Palmgren, 1947, 1952). The application of continuum mechanics to RCF is limited. Material response to cyclic loading in rolling contact involves complex localized microstructure decay and cannot be explained by few macroscopic parameters. Moreover, fracture mechanics does not provide an approach to realistic description of RCF. The stage of crack growth, representing only about 1% of the total running time to incipient spalling (Yoshioka, 1992; Yoshioka & Fujiwara, 1988), is short compared to the phase of damage initiation in the brittle hardened steels. Without a fundamental understanding of the microscopic mechanisms of lattice defect accumulation for the prediction of material aging under rolling contact loading, which is reflected in (visible) changes of the cyclically stressed microstructure that are decisive for the resulting fatigue life, therefore, measures to increase bearing durability, for instance, by tailored alloy design cannot be derived. Physically based RCF models, however, are hardly available in the literature (Fougères et al., 2002). The reason might be that hardened bearing steels reveal complex microstructures of high defect density far from equilibrium. Precipitation strengthening due to temper carbides of typically 10 to 20 nm in diameter governs the fatigue resistance of the material in tempered condition. The mechanism proposed in the following therefore focuses on the interaction between dislocations and carbides or carbon clusters in the steel matrix.

The stress-strain hysteresis from plastic deformation in cyclic loading reflects energy dissipation (Voskamp, 1996). The vast majority of about 99% is generated as heat (Wielke, 1974), which produces a limited temperature increase under the conditions of bearing operation. The remaining 1% is absorbed as internal strain energy. This amount is associated with continuous lattice defect accumulation during metal fatigue and, therefore, damaging changes to the affected microstructure eventually. Gradual decay of retained austenite, martensite and cementite occurs in the instability stage of RCF (see Figure 10), with the dislocation arrangement of a fine sub-grain (cell) structure in the emerging ferrite and white etching band as well as texture development inside the DER in the upper life range (Voskamp, 1996). The phase transformations require diffusive redistribution of carbon on a micro scale, which is assisted by plastification. Strain energy dissipation and microplastic damage accumulation in rolling contact fatigue is described by the mechanistic Dislocation Glide Stability Loss (DGSL) model introduced in Figure 22. The different stages of compressive residual stress formation, XRD peak width reduction and microstructural alteration during advancing RCF are discussed in the framework of this metal physics scheme in the following.
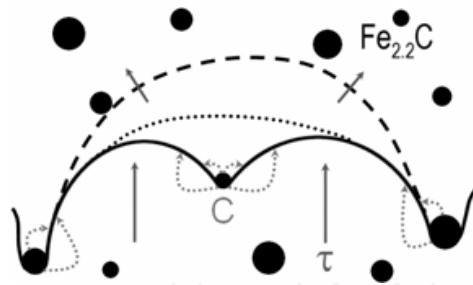
Fig. 22. In the dislocation glide stability loss (DGSL) model of rolling contact fatigue, according to which gradual dissolution of (temper) carbides (spheres) occurs by diffusion (dotted arrows) mediated continuous carbon segregation at pinned dislocations (lines) bowing out under the influence of the cyclic shear stress τ (solid arrows), the smallest particles tend to disappear first due to their higher curvature-dependent surface energy so that the obstacles are passed successively and the level of localized microplasticity is increased accordingly

Rolling contact fatigue life is governed by the microcrack nucleation phase. Gradual dissolution of $Fe_{2.2}C$ temper carbides (spheres in Figure 22) driven by carbon segregation at initially pinned dislocations (lines), which bow out under the acting cyclic shear stress τ (arrows), causes successive overcoming of the obstacles and local restarting of plastic flow until activation of Frank-Read sources. Fatigue damage incubation in the steady state of apparent elastic material behavior is followed in the instability stage by the microstructural changes of DER formation, decay of globular secondary cementite (in the DGSL model due to dislocation-carbide interaction) and regular ferritic white etching bands developing inside the DER. Strain hardening, which embrittles the aged steel matrix and thus promotes crack initiation, compensates for the diminishing precipitation strengthening in the progress of rolling contact fatigue. This process results in further compressive residual stress build-up from the shakedown level and newly decreasing XRD peak width (see Figure 10). Gradual concentration of local microplasticity and microscopic accumulation of lattice defects characterize proceeding RCF damage. According to the DGSL model, Cottrell segregation of carbon atoms released from dissolving carbides at uncovered cores of dislocations, which are regeneratively generated by the glide movements during yielding, provides an additional contribution to the XRD peak width reduction by cyclic rolling contact loading (Gegner et al., 2009). The experimental proof of this essential prediction is discussed in detail below by means of Figures 23 and 24. The gradually increasing amount of localized dislocation microplasticity represents the fatigue defect accumulation mechanism of the DGSL model of RCF. It is thus associated with a rising probability for bearing failure (cf. Figure 10) due to material aging. The DGSL criterion for local microcracking is based on a critical dislocation density. Orientation and speed of fatigue crack propagation can then also be analyzed.

The proposed dislocation-carbide interaction mechanism explains (partial) fragmentation of uncuttable globular carbides of μm size, which is occasionally observed in microsections, and the increased energy level in the affected region. Localized microplastic deformation is related to energy dissipation. Note that the DGSL fatigue model involves the basic internal friction mechanism of Snoek-Köster dislocation damping under cyclic rolling contact loading. The increasing dislocation density of the aged, highly strained material eventually causes local dynamic recrystallization into the nanoscale microstructure of white etching areas, where carbides are completely dissolved. This approach also adumbrates an
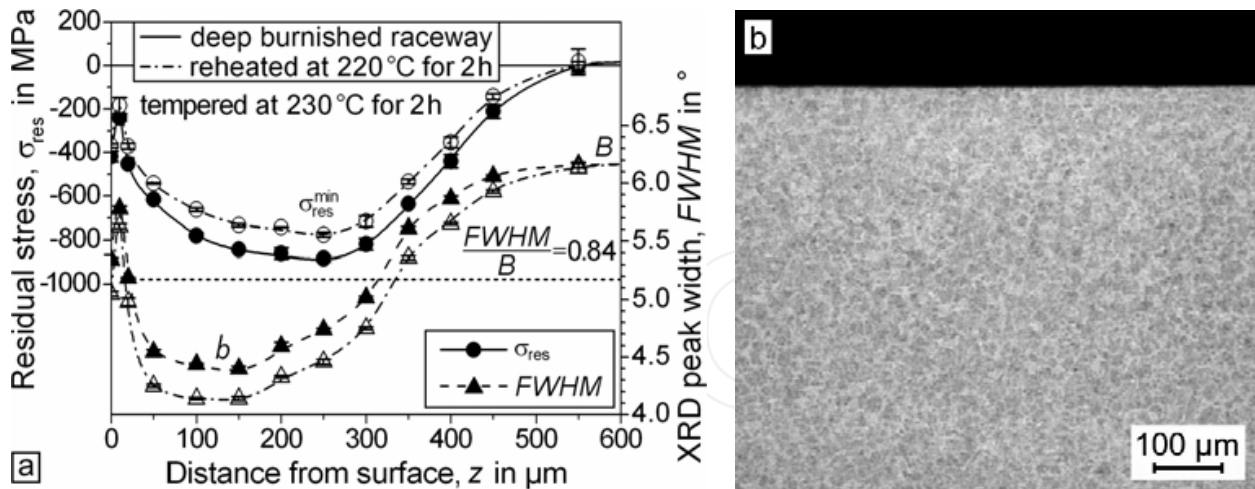
Fig. 23. Investigation of cold working of a martensite hardened OR revealing (a) the residual stress and XRD peak width distributions, respectively after deep ball burnishing ($b/B \approx 0.71$) and subsequent reheating below the tempering temperature (unchanged hardness: 61 HRC) and (b) an etched axial microsection after burnishing free of visible microstructural changes
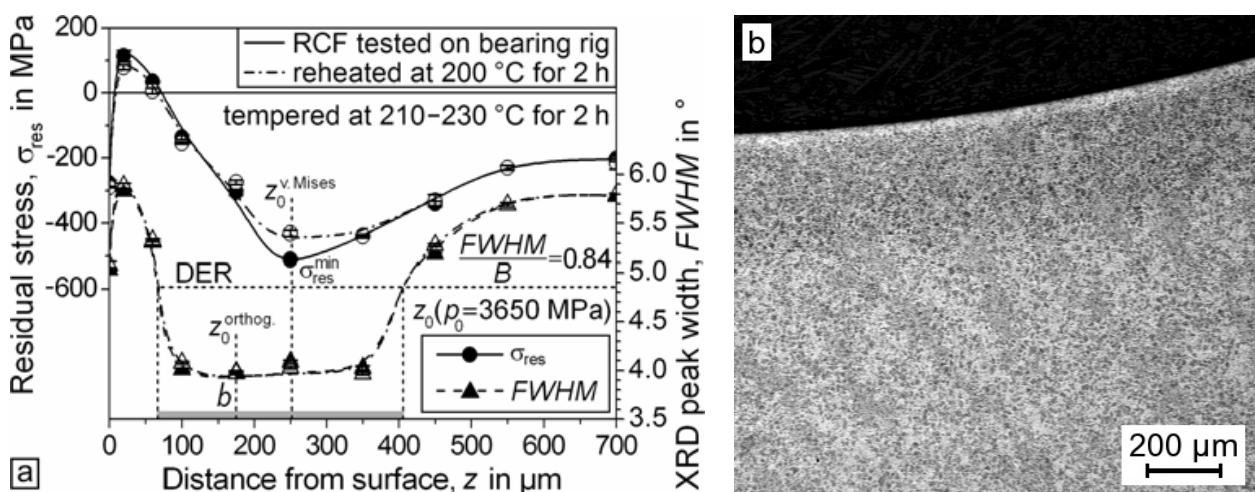

Fig. 24. Experimental investigation of reheating below tempering temperature (unchanged hardness: 60.5 HRC) after RCF loading on the martensite hardened IR of the endurance life tested DGBB of Figures 16 and 17 revealing (a) the initial and final residual stress and XRD peak width distributions ($b/B \approx 0.68$) and (b) an etched axial microsection (DER indicated)

interpretation of the development of (steep) white bands (see Figure 21c) differently from adiabatic shearing (Schlicht, 2008). The DGSL model suggests strain induced reprecipitation of carbon in the form of carbides at a later stage of RCF damage (Lindahl & Österlund, 1982; Shibata et al., 1996). Former austenite or martensite grain boundaries represent sites for heterogeneous nucleation. Reprecipitated carbide films tend to embrittle the material.

Shakedown in Figure 10 can be considered to be a cold working process (Nierlich & Gegner, 2008). As discussed in section 3.3, the XRD line broadening is sensitive to changes of the lattice distortion. The rapid peak width reduction during shakedown occurs due to glide induced rearrangement of dislocations to lower energy configurations, such as multipoles. This dominating influence, which surpasses the opposing effect of the limited dislocation

density increase in the defect-rich material of hardened bearing steel, reflects microstructure stabilization. An example of intense shakedown cold working is high plasticity ball burnishing. Figure 23a presents the result of the XRD measurement on the treated outer ring (OR) raceway of a taper roller bearing. The residual stress profile obeys the distribution of the v. Mises equivalent stress below the Hertzian contact (cf. Figure 1). The minimum XRD peak width b occurs closer to the surface. The applied Hertzian pressure is in the range of 6000 MPa (6 mm ball diameter). At the same b/B level of about 0.71 as in Figure 18a, in contrast to rolling contact fatigue, deep ball burnishing does not produce visible changes in the microstructure. The difference is evident from a comparison of the corresponding etched microsections in Figures 18c and 23b. Material alteration owing to mechanical conditioning by the build-up of compressive residual stresses in the shakedown cold working process is restricted to the higher fatigue endurance limit and based on yielding induced stabilization of the dislocation configuration but does not involve carbon diffusion (Nierlich & Gegner, 2008). Therefore, no dark etching region from martensite decay develops in the microstructure of the burnished ring displayed in Figure 23b, even in the depth zone indicated in Figure 23a by the XRD peak width relationship $FWHM/B \leq 0.84$. Mechanical surface enhancement treatments, like deep burnishing, shot peening, drum deburring and rumbling, as well as finishing operations (e.g. grinding, honing) and manufacturing processes, such as hard turning or (high-speed) cutting, are not associated with microstructural fatigue damage (Gegner et al., 2009; Nierlich & Gegner, 2008).

Figure 23a indicates that an additional stabilization of the plastically deformed steel matrix by dislocational carbon segregation can also be induced thermally by reheating after deep ball burnishing. The associated slight compressive residual stress reduction does not affect a bearing application. The positive effect of this thermal post-treatment on RCF life, in the literature reported for surface finishing (Gegner et al., 2009; Luyckx, 2011), suggests only subcritical partial carbide dissolution. According to the DGSL model, the corresponding amount of $FWHM$ decrease should be included in the reduced b value in rolling contact fatigue (cf. Figure 22). Therefore, no additional effect by similar reheating below the applied tempering temperature is to be expected. This crucial prediction of the model is confirmed by the experiment. In Figure 24a, the small thermal reduction of the absolute value of the residual stresses is comparable with the alterations for burnishing shown in Figure 23a. However, reheating after RCF loading leaves the XRD peak width unchanged. In Figures 23a and 24a, the plotted σ_{res} and $FWHM$ values are deduced at separate sites of the raceway (i.e., one individual specimen for each depth) with increased reliability from three and eight repeated measurements, respectively, before and after the thermal treatment. The results of Figure 24a agree well with the XRD data of Figure 16a, determined by successive electrochemical polishing at one position of the racetrack of the same DGBB inner ring. This concordance is also evident for the indicated dark etching regions from a comparison of Figures 24b and 17a. The DGSL model is strongly supported by the discussed findings on the different $FWHM$ response to reheating after rolling contact fatigue and cold working.

4.3 Current passage through bearings − The aspect of hydrogen absorption and accelerated rolling contact fatigue

The passage of electric current through a bearing causes damage by arcing across the surfaces of the rings and rolling elements in the contact zone. Fused metal in the arc results in the formation of craters on the racetrack, the appearance of which depends on the frequency. In the literature, the origin of causative shaft voltages in rotating machinery and

the sources of current flows, the electrical characteristics of a rolling bearing and the influence of the lubricant properties as well as the development of the typical surface patterns are discussed in detail (Jagenbrein et al., 2005; Prashad, 2006; Zika et al., 2007, 2009, 2010). Complex chemical reactions occur in the electrically stressed oil film (Prashad, 2006). However, the ability of hydrogen released from decomposition products to be absorbed by the steel under the prevailing specific circumstances and subsequently to affect rolling contact fatigue is not yet investigated so far (Gegner & Nierlich, 2011b, 2011c).

Depending on the design of the electric generator, e.g. in diesel engines, alternator bearings may operate under current passage. Possible damage mechanisms become more important today because of the increased use of frequency inverters. Grease lubricated deep groove ball bearings with stationary outer ring, stemming from an automobile alternator rig test, are investigated in the following. The running period is in accordance with the nominal L_{10} life. Rings and balls are made out of martensitically hardened bearing steel. The racetrack in Figure 25a suffers from severe high-frequency electric current passage. Arc discharge in the lubricating gap causes a gray matted surface. The resulting shallow remelting craters of few μm in diameter and depth cover the racetrack densely. The indicated isolated indentation, magnified in Figure 25b, reveals the earlier condition of a less affected area. The tribological properties of the contact surface are still sufficient. The microsection of Figure 25c confirms the small influence zone by a thin white etching layer. However, continuous chemical decomposition of the lubricant and surface remelting promote hydrogen penetration. Thus, a highly increased content of more than 3 ppm by weight is measured for the DGBB outer ring of Figure 25 by carrier gas hot extraction (CGHE). Typical concentrations in the as-delivered state, after through hardening and machining, range from 0.5 to 1.0 ppm H.
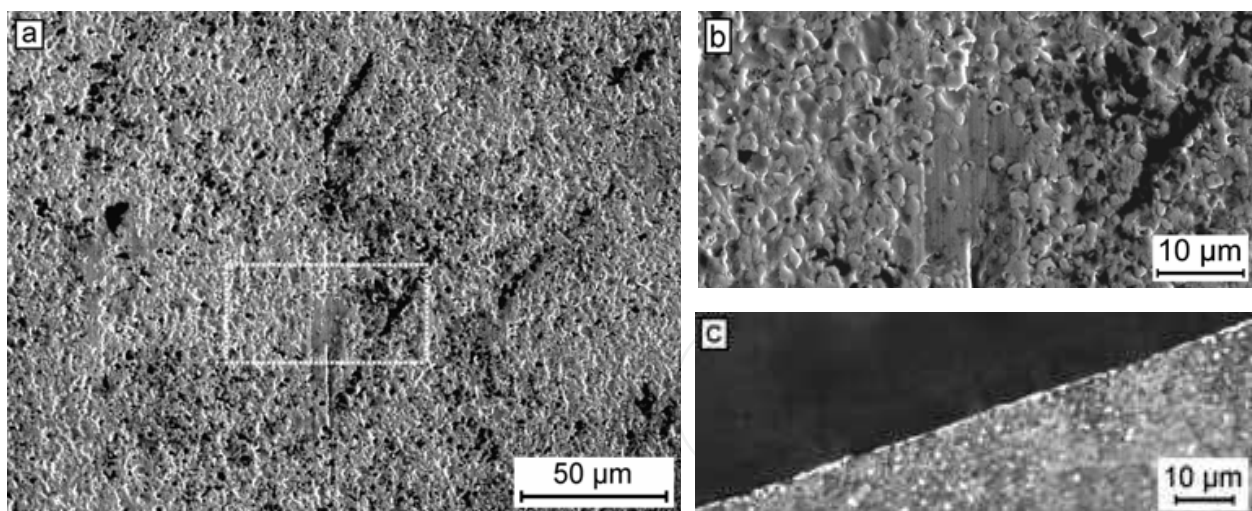

Fig. 25. Characterization of severe high-frequency electric current passage through a DGBB by (a) a SEM-SE overview and (b) the indicated SEM-SE detail of the remelted OR raceway track and (c) a near-surface LOM micrograph of an etched axial microsection

The amount of hydrogen absorbed by the steel depends on the release from the decomposition products of the aging lubricant and the available catalytically active blank metal surface (Kohara et al., 2006). Both affecting factors are enhanced by current passage in service. Fresh blank metal from remelting on the raceway enables the process step from physi- to chemisorption with abstraction of hydrogen atoms, which is otherwise effectively inhibited by the regenerative formation of a passivating protective reaction layer on the

surface. The weaker operational high-frequency electric current passage of another bearing from the same rig test series documented in Figure 26a results only in a slightly increased content of 1.3 ppm H. The original honing structure of the raceway is displayed in Figure 26b. For comparison, Figures 25a, 26a and 26b have similar magnification.

An XRD material response analysis is performed in the load zone of the raceway of the hydrogen loaded outer ring of the bearing of Figure 25. According to Figures 27a, a high Hertzian pressure above 5000 MPa is deduced.
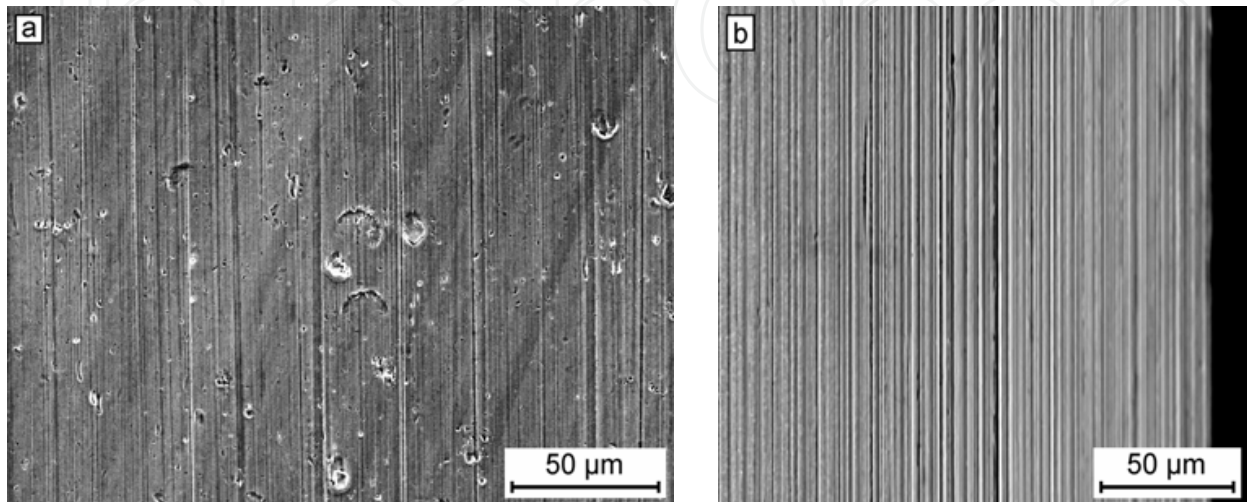
Fig. 26. SEM-SE image of the raceway (a) of the OR of an identical DGBB tested in the same alternator rig as the bearing of Figure 25 after moderate high-frequency electric current passage and (b) in as-delivered (non-overrolled) surface condition with original honing marks

The applied joint evaluation of the depth profiles of the residual stress and XRD peak width in the subsurface zone of classical rolling contact fatigue is shown in Figure 27b. The damage parameter equals $b/B \approx 0.71$. The XRD L_{10} life equivalent is thus not yet exceeded on the outer ring. The microsection in Figure 27c confirms a subsurface dark etching region, the position of which reflects the contact angle.
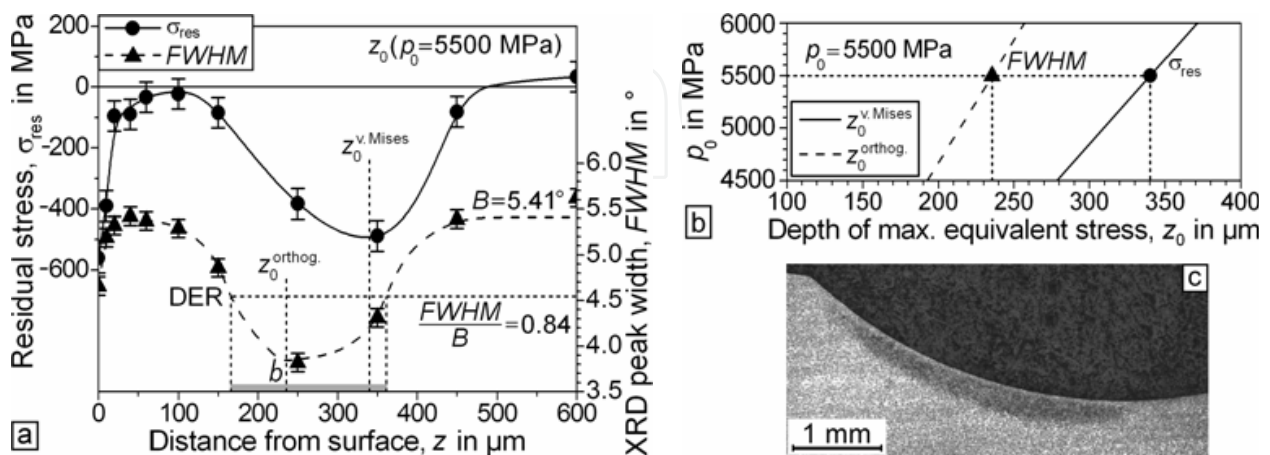
Fig. 27. Material response analysis of the OR of the tested DGBB of Figure 25 including (a) the residual stress and XRD peak width distribution ($b/B \approx 0.71$, B measured below the shoulder), (b) the joint profile evaluation and (c) an axial microsection with pronounced DER

Inside the wide DER of Figure 27c, extended white etching areas are located (cf. Figure 28a), which evolve from the steel matrix. In the used clean material, butterfly formation is irrelevant and only two early stages are found (see inset of Figure 28a). Etching accentuates the actual RCF damage: the DER identified as brittle by the observed preparative cracking is clearly distinguishable from the chemically less affected material above and below in the indicated SEM-SE detail of Figure 28b. The WEA inside the DER appear smooth black.
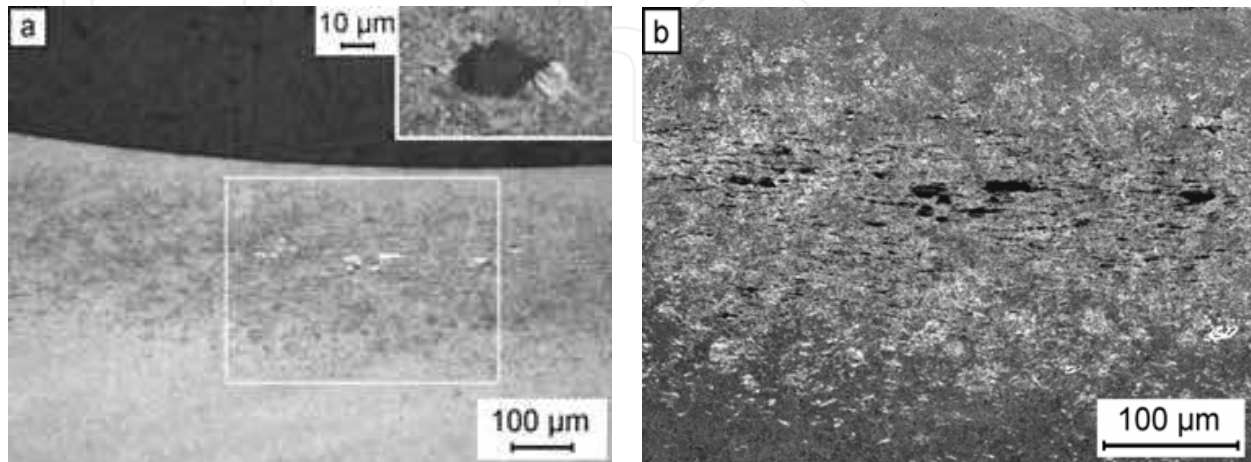
Fig. 28. Etched axial microsection of the DGBB outer ring of Figure 27c revealing (a) a LOM overview (the inset shows an embryo butterfly) and (b) the indicated SEM-SE detail

The LOM micrograph in Figure 29a reveals dense dark etching regions adjacent to the WEA zones. Although reported contrarily in the literature (Martin et al., 1966), the embrittled dark etching region evidently acts as precursor of further phase transformation. The SEM-SE detail of Figure 29b also points to interfacial delamination (see indication) as pre-stage of fatigue crack initiation.
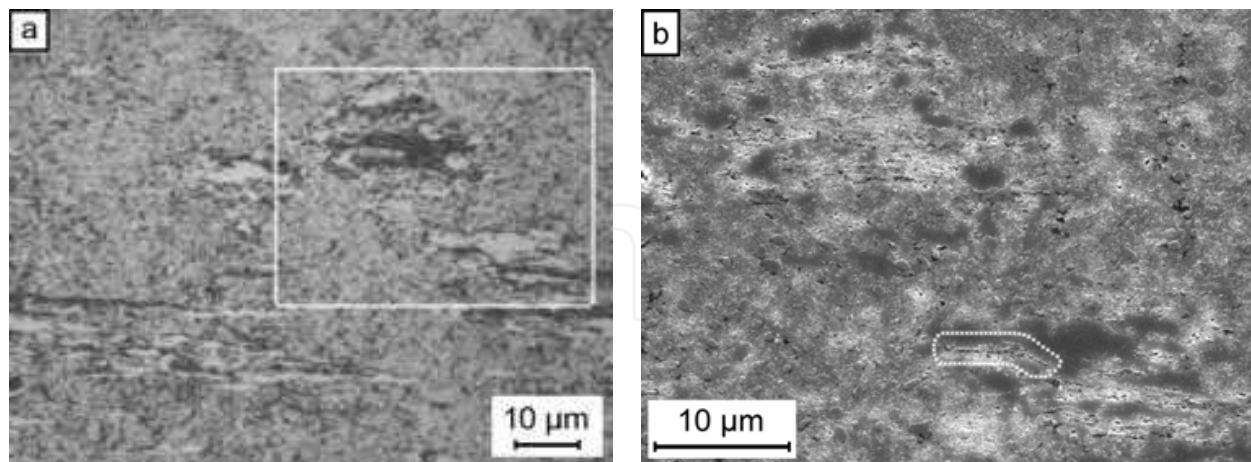
Fig. 29. Etched axial microsection of the DGBB outer ring of Figure 27c revealing (a) a LOM image and (b) the indicated SEM-SE detail

The development of white etching bands is identified in the radial microsection of the investigated outer ring shown in Figure 30a. Dense FWB and distinct SWB of inclinations $\beta_f=25°$ and $\beta_s=76°$, respectively, are visible inside the indicated DER. The central SEM-SE detail of Figure 30b reveals the included angle β_{s-f} of 51° (see section 4.1, Figure 21c). The

indication of microcrack initiation on white etching bands by interfacial delamination is confirmed by Figure 30c. It is not observed in pure mechanical rolling contact fatigue (Voskamp, 1996), where actually an influence of WEB (as well as of butterfly) formation on bearing life is not proven (Schlicht, 2008). Therefore, hydrogen induced cracking propensity on WEB suggests higher hardness of the white etching areas and hydrogen embrittlement. Note again the pronounced DER microstructure around the WEA in Figure 30c.
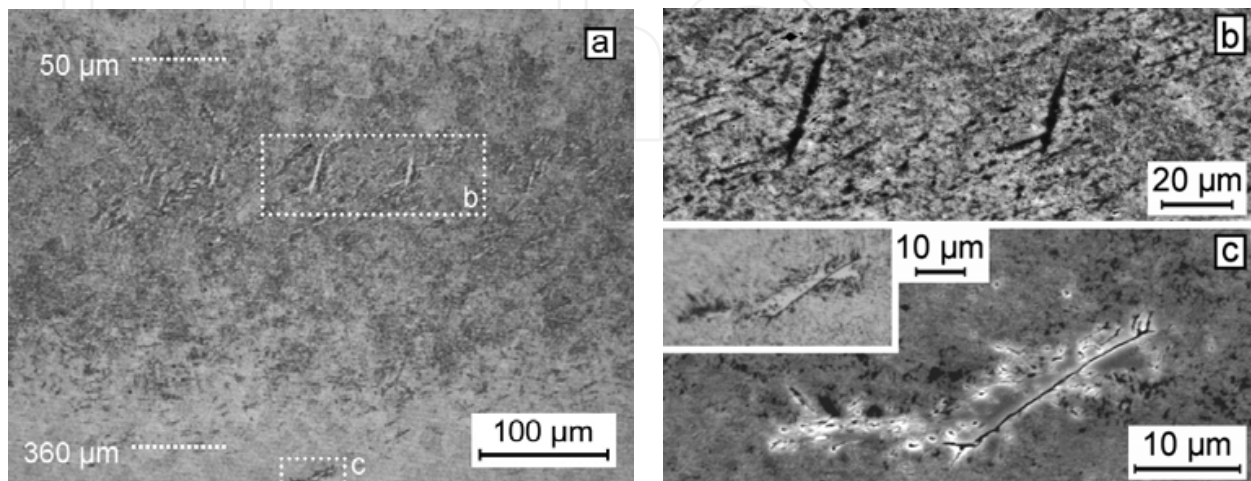

Fig. 30. Etched radial microsection of the OR of Figure 27c revealing (a) a LOM overview with indicated DER, (b) the SEM-SE detail b and (c) the SEM-SE detail c, where the corresponding LOM inset highlights the WEA precursor effect of the surrounding DER

As also emphasized in Figure 31a by grain boundary etching, flat and steep white bands evolve from the distinctive surrounding DER material. The SWB seem to develop in an earlier stage prior to the complete dense formation of FWB (cf. Figure 21c). Particularly the oriented slip bands of FWB exhibit more intense white etching microstructure (cf. Figure 21c). Figure 31b presents the corresponding SEM-SE image of this extended detail of Figure 30b in the center of Figure 30a. The gradual evolution of white etching bands from the DER precursor, as particularly evident from Figure 31a, indicates advancing fatigue processes, e.g. as outlined in section 4.2, presumably correlated with texture development and dynamic recrystallization during rolling contact loading (Voskamp, 1996). On the other hand, this microstructural finding speaks against causative adiabatic shearing (Schlicht, 2008). The preferred occurrence of white etching bands in ball bearings should rather be connected with the higher Hertzian pressure compared to a corresponding roller contact. Note that no WEA of premature rolling contact fatigue damage are formed in the case of Figure 26. This moderate high-frequency electric current passage in operation is connected with only slight hydrogen enrichment in the bearing steel.

Despite the occurrence of white etching bands in the outer ring of the rig tested DGBB of Figure 25, as documented in Figures 28 to 31, the XRD material aging parameter deduced from Figure 27a amounts to just $b/B \approx 0.71$. The same value is derived from the peak width distribution in Figure 18a, where for pure mechanical subsurface RCF, however, no WEA are formed inside the DER (see Figure 18c). As for the bearing operating under severe high-frequency electric current passage, the XRD L_{10} equivalent of classical rolling contact fatigue without additional chemical loading is not yet exceeded but well developed white etching bands, particularly SWB, already occur, hydrogen charging noticeably accelerates the

evolution of microstructural RCF damage (hydrogen accelerated rolling contact fatigue, H-RCF). The dark etching region extends to zones of $FWHM/B > 0.84$ near the surface, as evident from a comparison of Figures 27a, 28a and 30a. The calibration relationship between the L_{10} life and the evidently reduced b/B equivalent is modified by the hydrogen embrittled DER.
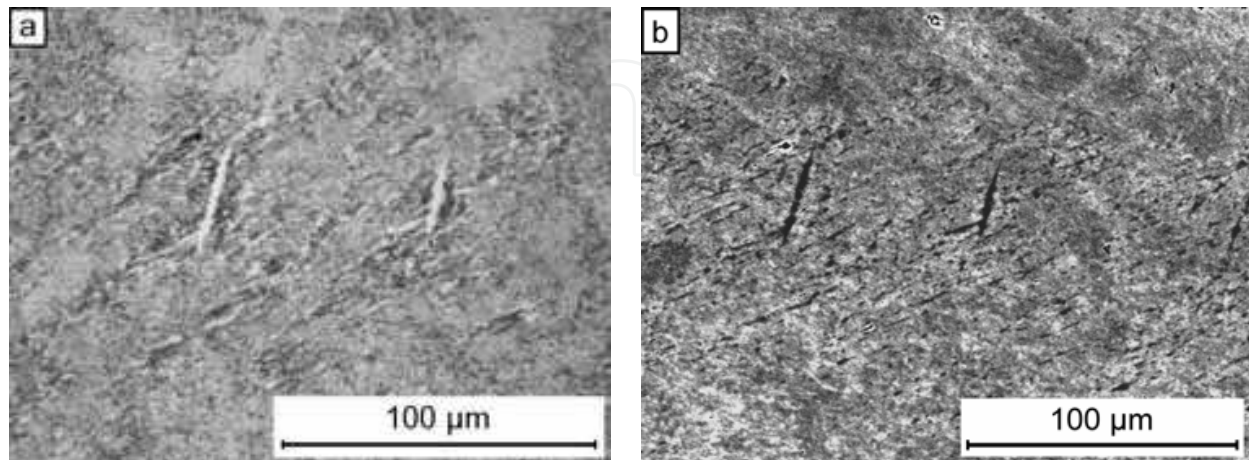

Fig. 31. Detail (approx. b) of Figure 30 comparing (a) a LOM and (b) a SEM-SE micrograph

The metal physics dislocation glide stability loss model, introduced in section 4.2, provides an approach to the mechanistic description of rolling contact fatigue in bearing steels. Hydrogen interacts with lattice defects (Gegner et al., 1996). The response to cyclic loading reflects its high atom mobility even at low temperature. The effect of hydrogen can be illustrated by the DGSL model of Figure 22. The microscopic fatigue processes are considerably promoted by intensifying the increase of dislocation density and glide mobility. Mechanisms of hydrogen enhanced localized plasticity (HELP) are discussed in the literature (Birnbaum & Sofronis, 1994). A comparison of chemically assisted with pure mechanical rolling contact fatigue and shakedown cold working at constant reference level of $b/B \approx 0.71$ in Figures 18, 23 and 27 to 31, completed by Figures 20, 21 and 24, suggests that material aging is accelerated by enhancing the microplasticity. At the same stage of b/B reduction, microstructural RCF damage is much more advanced. Premature formation of ribbon like or irregularly oriented white etching areas, for instance, might yet occur at lower loads.

5. Surface failure induced by mixed friction in rolling-sliding contact

The practically predominating surface failure mode involves various damage mechanisms. Besides indentations, discussed in detail in section 2.2, mixed friction or boundary lubrication in the rolling contact area occurs frequently in bearing applications. Polishing wear on the raceway, resulting in differently pronounced smoothing of the machining marks, is a characteristic visual indication. The depth of highest material loading is shifted towards the surface by sliding friction in rolling contact. The effect on the distribution and the maximum of the equivalent stress is similar to the scheme shown in Figure 5. The mechanisms of crack initiation on the surface are of utmost technical importance (Olver, 2005). New aspects of rolling contact tribology in bearing failures are presented in the following.

5.1 Vibrational contact loading and tribological model

Near-surface loading is often superimposed by the impact of externally generated three-dimensional mechanical vibrations that represents a common cause of disturbed EHL operating conditions, e.g., in paper making or weaving machines, coal pulverizers, wind turbines, cranes, trains, tractors and fans. Ball bearings in car alternators of four-cylinder diesel engines are another familiar example.

The SEM image of Figure 32a shows the completely smoothed raceway in the rotating main load zone of a CRB inner ring after a rig test time of about 40% of the calculated nominal L_{10} life (Nierlich & Gegner, 2002). Only parts of the deepest original honing grooves are left over on the surface. Causative mixed friction results from inadequate lubrication conditions without sufficient film formation (fuel addition to the oil). Initial micropitting by isolated material delamination of less than 10 μm depth is observed. Figure 32b provides a comparison with the non-overrolled as-finished raceway condition. On the damaged inner ring, a residual stress material response analysis is performed. The result is shown in Figure 33a. No changes of the measured XRD parameters in the depth of the material are found, whereas the XRD peak width on the surface decreases to $b/B{\geq}0.79$. The relation symbol accounts for the small *FWHM* reduction of about 0.2° due to the honing process (see section 3.3, Figure 16a). Material aging considerably exceeds the XRD L_{10} equivalent value of 0.86 for the relevant surface failure mode of RCF. The corresponding re-increase of the residual stress on the raceway, discussed in the context of Figures 11 and 12 in section 3.3, reaches −230 MPa.
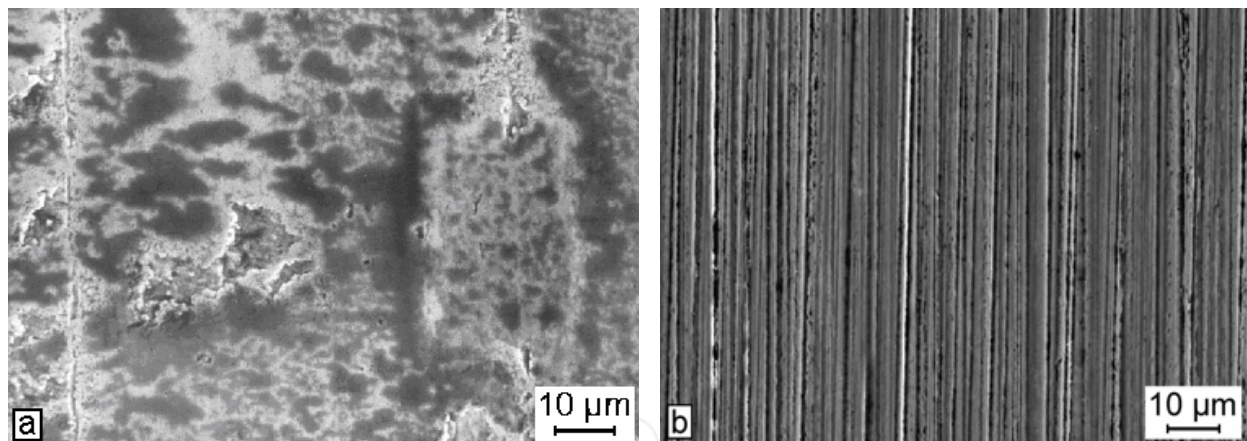

Fig. 32. SEM-SE image of (a) the damaged raceway of the inner ring of a CRB after rig testing under engine vibrations and (b) an original honing structure at the same magnification

The residual stress distribution of Fig. 33a is identified as a type B profile of vibrational loading in rolling-sliding contact (Gegner & Nierlich, 2008). The characteristic compressive residual stress side maximum in a short distance from the surface (here 40 μm), clearly above the depth $z_0^{\mathrm{v.Mises}}$ of maximum v. Mises equivalent stress for pure radial load, is reflected in the corresponding reduction of the XRD peak width. The monotonically increasing type A vibration residual stress profile occurs more frequently in practical applications. The result of a material response analysis on a CRB outer ring, the raceway of which does not reveal indentations, represents a prime example in Figure 33b. Bainitic through hardening of the bearing steel results in compressive residual stresses in the core of

the material. The XRD life parameter $b/B \geq 0.82$ is taken from the diagram. The running time of 2×10^8 revolutions indicates low-cycle fatigue under the influence of intermittently acting severe vibrations (Nierlich & Gegner, 2008). The residual stress analysis of the inner ring of a taper roller bearing from a harvester in Figure 34a provides another instructive example. Mixed short-term deeper reaching type A vibrational and near-surface Hertzian micro contact loading of the material are superimposed. Figure34b reveals indentations on the partly smoothed raceway. The applied Hertzian pressure p_0 amounts to 2000 MPa. For comparison, the depth of maximum v. Mises equivalent stress for incipient plastic deformation in pure radial contact loading, i.e. p_0 above 2500 to 3000 MPa, equals about 180 μm.
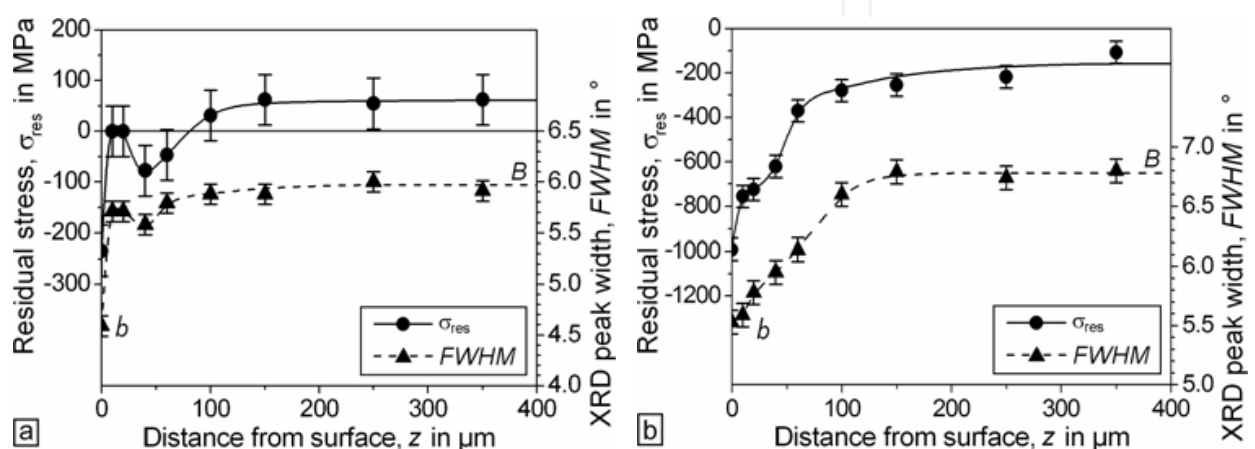
Fig. 33. The two types of vibration residual stress-XRD line width profiles, i.e. (a) type B with near-surface side peaks measured on the IR raceway of a CRB from a motorcycle gearbox test rig and (b) type A with monotonically increasing curves from a field application
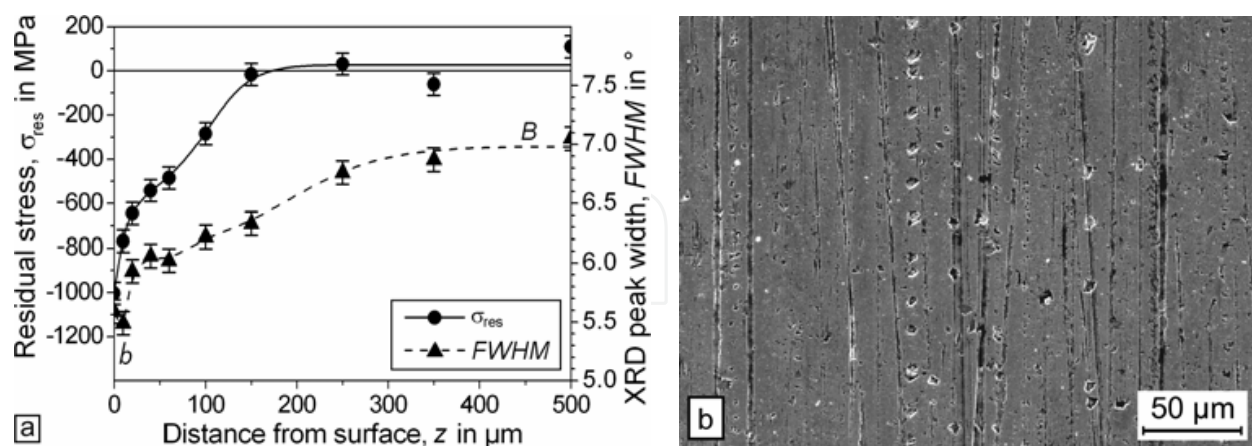
Fig. 34. Investigation of the IR of a vibration-loaded harvester TRB revealing (a) the obtained type A residual stress pattern and (b) a SEM-SE image of the raceway with indentations

Both types of residual stress distributions are simulated experimentally in a specially designed vibration test rig for rolling bearings (Gegner & Nierlich, 2008). A type N CRB is used. The stationary lipless outer ring of the test bearing is displaced and experiences high vibrational loading via the sliding contact to the rollers. It thus becomes the specimen. In

addition to the radial load, controlled uni- to triaxial vibrations can be applied in axial, tangential and radial direction. Figure 35 displays a photograph of the rig. It represents a view of the housing of the test bearing and the equipment for the transmission of axial and tangential vibrations (radial excitation from below) with thermocouples and displacement sensors.

A micro friction model of the rolling-sliding contact is introduced by means of Figure 36. It describes the effect of vibrational loading. As shown in Figure 36, tangential forces by sliding friction acting on a rolling contact increase the equivalent stress and shift its maximum toward the surface on indentation-free raceways (Broszeit et al., 1977). A transition, indicated by solid-line curves, occurs between friction coefficients μ of 0.2 and 0.3: above and below $\mu=0.25$, the increasing maximum of the Tresca equivalent stress is located directly on or near the surface, respectively. If the yield strength of the material is exceeded (cf. Figure 5), therefore, type A or B residual stress depth profiles are generated.
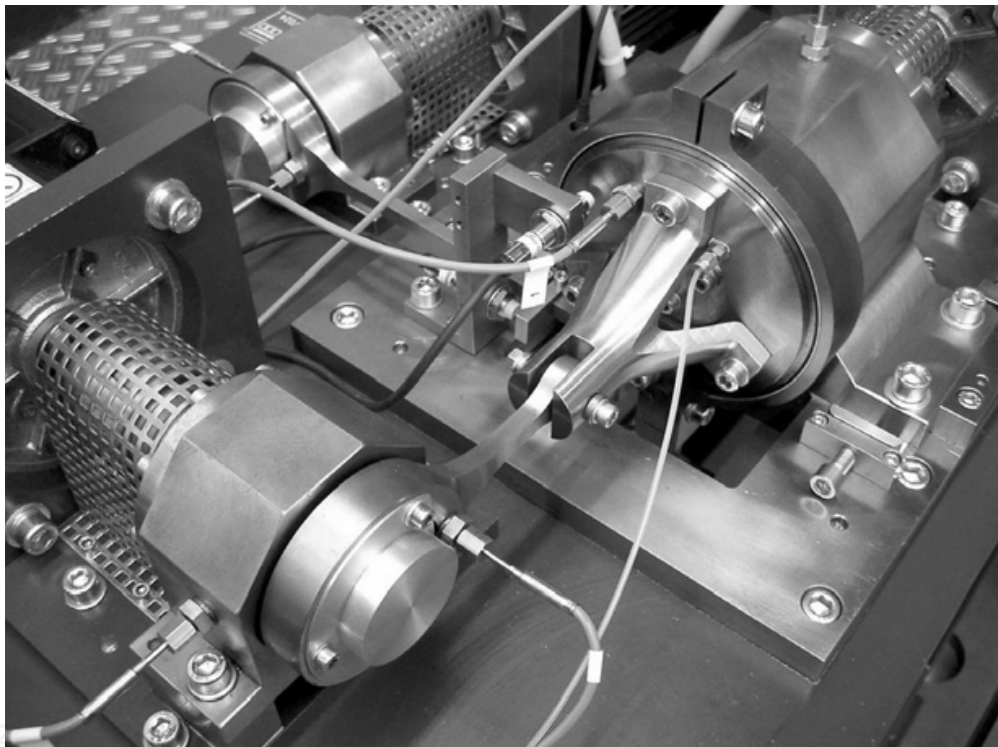
Fig. 35. Housing of the test bearing with devices for vibration generation

Material response to vibrational loading, which causes increased mixed friction, is described in the tribological model by partitioning the nominal contact area A into microscopic sections of different friction coefficients (Gegner & Nierlich, 2008). The inset of Figure 36 illustrates the basic idea. In some subdomains, arranged e.g. in the form of dry spots or bands, peak values from $\mu_> \approx 0.2$ (type B) to $\mu_> \geq 0.3$ (type A) are supposed to be reached intermittently for short periods. The thixotropy effect supports this concept because shearing of the lubricant by vibrational loading reduces the viscosity, which increases the tendency to mixed friction. In the other subareas of the contact, $\mu_<$ is much lower so that the average friction coefficient $\mu_{(eff)}$, meeting a mixing rule, remains below 0.1 as typical of running rolling bearings. Besides the verified compressive residual stress buildup, nonuniform cyclic mechanical loading of the contact area by, in general, complex three-

dimensional vibrations is also evident from occasionally observed dent-like plastic deformation on the surface, spots of dark etching regions in the microstructure of the outermost material and varying preferred orientation of yielding across the raceway width, reflected in differing tangential and axial components of the residual stresses in the affected edge zone (Gegner & Nierlich, 2008). Friction increase is confirmed by temperature rise in the lubricating gap that correlates with the power loss per contact area. This effect can be exploited to easily assess the vibration resistance of specific oils or greases on the adapted bearing test rig (Gegner & Nierlich, 2008).
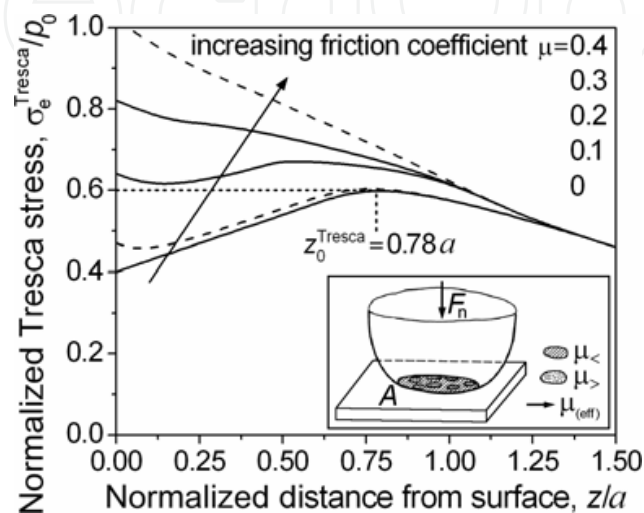
Fig. 36. Distribution of the Tresca equivalent stress below a rolling-sliding contact (z_0 depth indicated for pure radial load, i.e. $\mu=0$) and illustration of the tribological model of localized friction coefficient in the inset (F_n is the normal force)

Under the influence of vibrations, disturbance of proper contact operating conditions in a way that high shearing stresses are induced in the lubricating film can promote lubricant degradation (Kudish & Covitch, 2010). Reduced lubricity enhances the effect of sliding friction, e.g. described in the tribological model of Figure 36. Further to the discussed mechanical and thermal influence, vibration loading induces chemical aging of the lubricant and its additives (Gegner & Nierlich, 2008). Contaminations, like water or wear debris, increase the effect. The gradual decomposition process and associated acidification of the lubricant promote, for instance, the initiation of surface cracks on the raceway by tribochemical dissolution of nonmetallic MnS inclusion lines, which is discussed in the next section.

5.2 Tribochemically initiated surface cracks

First, Figure 37 gives a demonstrative example of a corrosive attack by a decomposed lubricant. The etching pattern on the raceway reveals chemical smoothing of the surface.

Copper contamination by abrasion from the graphite-brass ground brush of the diesel electric locomotive gets into the grease of the train wheel bearing and accelerates lubricant aging. As evident from Figure 37, the foreign particles also cause indentations on the raceway. An electrical oil sensor system can be used for online condition monitoring of the lubricant (Gegner et al., 2010). The application in industrial gearboxes, for instance of wind turbines, is of special practical interest. Note that the (e.g., extreme pressure) additives markedly influence the electrical properties of the lubricant (Prashad, 2006).
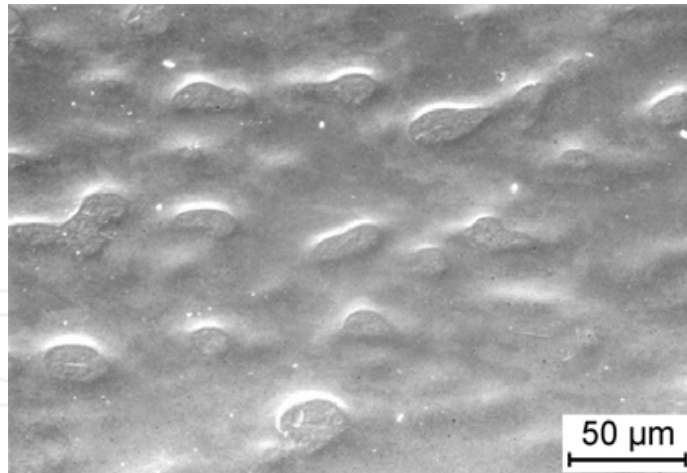
Fig. 37. SEM-SE image of a chemical surface attack on the outer ring raceway of a CRB

As exemplified by Figure 38, some manganese sulfide lines intersect the rolling contact surface. Such inclusions are manufacturing related from the steelmaking process, despite the high level of cleanliness of bearing grades.
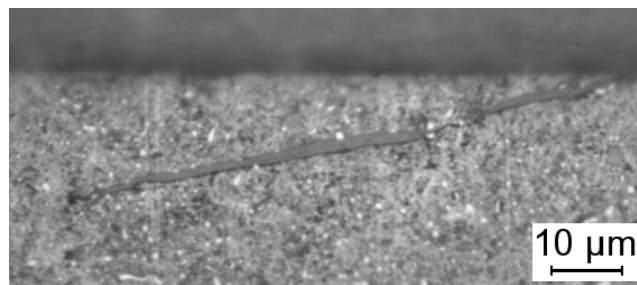

Fig. 38. LOM micrograph of the etched metallographic section of a sulfide inclusion line intersecting the surface of the inner ring raceway of a cylindrical roller bearing

On the inner ring raceway of a cylindrical roller bearing of a weaving machine examined in Figure 39, mixed friction is indicated by the mechanically smoothed honing structure. Due to aging of the lubricating oil, as detected under vibration loading, the gradually acidifying fluid attacks the steel surface. Tribochemical dissolution of manufacturing related MnS inclusion lines leaves crack-like defects on the raceway. Sulfur is continuously removed as gaseous H_2S by hydrogen from decomposition products of the lubricant:

$$MnS + H_2 \rightarrow H_2S^{\uparrow} + Mn \tag{6}$$

The remaining manganese is then preferentially corroded out. This new mechanism of crack formation on tribologically loaded raceway surfaces is verified by chemical characterization using energy dispersive X-ray (EDX) microanalysis on the SEM. The EDX spectra in Figure 39, recorded at an acceleration voltage of 20 kV, confirm residues of manganese and sulfur at four sites (S1 to S4) of an emerging crack, thus excluding accidental intersection. The ring is made of martensitically hardened bearing steel. Reaction layer formation on the raceway is reflected in the signals of phosphorus from lubricant additives and oxygen.

Crack initiation by tribochemical reaction is also found on lateral surfaces of rollers. In Figure 40, remaining manganese and sulfur are detected by elemental mapping in the insets on the right.
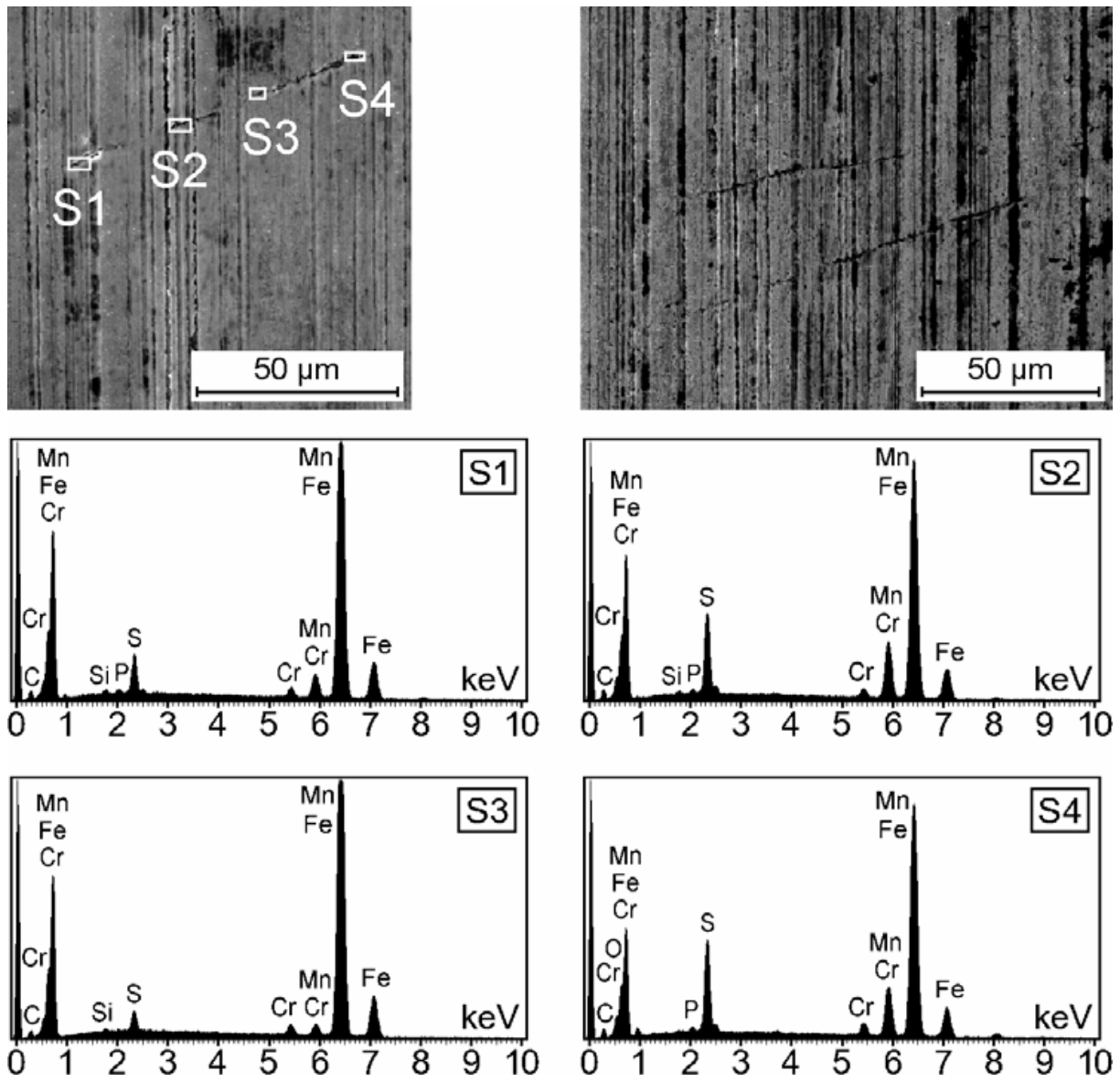
Fig. 39. SEM-SE images of cracks on the IR raceway of a CRB from the gearbox of a weaving machine and EDX spectra S1 to S4 taken at the indicated analysis positions
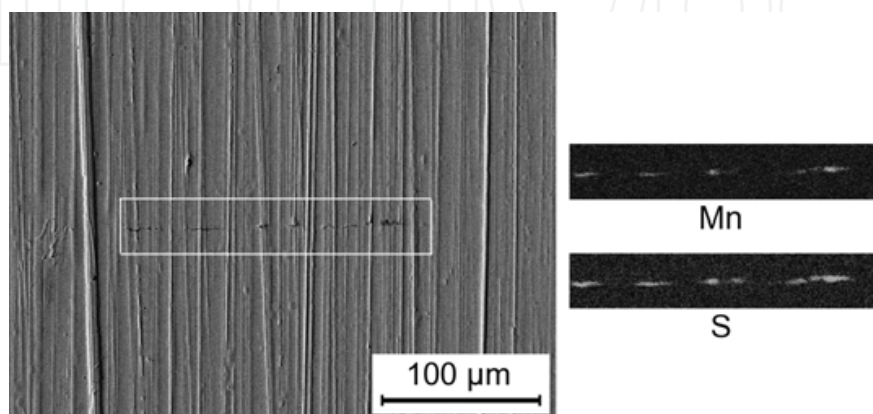

Fig. 40. SEM-SE image of a crack on a CRB roller and elemental mapping (area as indicated)

The tribochemical dissolution of MnS lines on raceway surfaces during the operation of rolling bearings also agrees with the general tendency that inclusions of all types reduce the corrosion resistance of the steel. The chemical attack occurs by the lubricant aged in service. The example of an early stage of defect evolution in Figure 41a points out that continuous dissolution but not fracturing of MnS inclusions gradually initiates a surface crack. Three analysis positions, where residues of manganese and sulfur are found, are indicated in the SEM image. An exemplary EDX spectrum is shown in Figure 41b. The inner ring raceway of the ball bearing from a car alternator reveals high-frequency electric current passage (cf. Figure 26a) that promotes lubricant aging (see section 4.3).
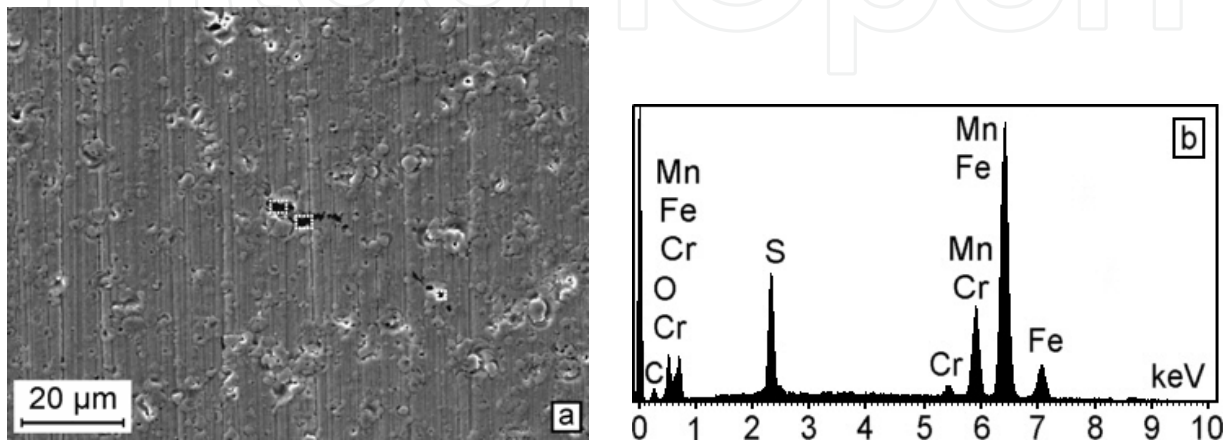
Fig. 41. Tribochemically induced crack evolution on the IR raceway of a DGBB revealing (a) a SEM-SE image with indicated sites where EDX analysis proves the presence of residues of MnS dissolution and (b) a recorded EDX spectrum exemplarily of the analysis results

After defect initiation on MnS inclusions, further damage development involves shallow micropitting (Gegner & Nierlich, 2008). Figure 42a also suggests crack propagation into the depth. Four sites of verified MnS residues are indicated, for which Figure 42b provides a representative detection example. The partly smoothed raceway reflects the effect of mixed friction.
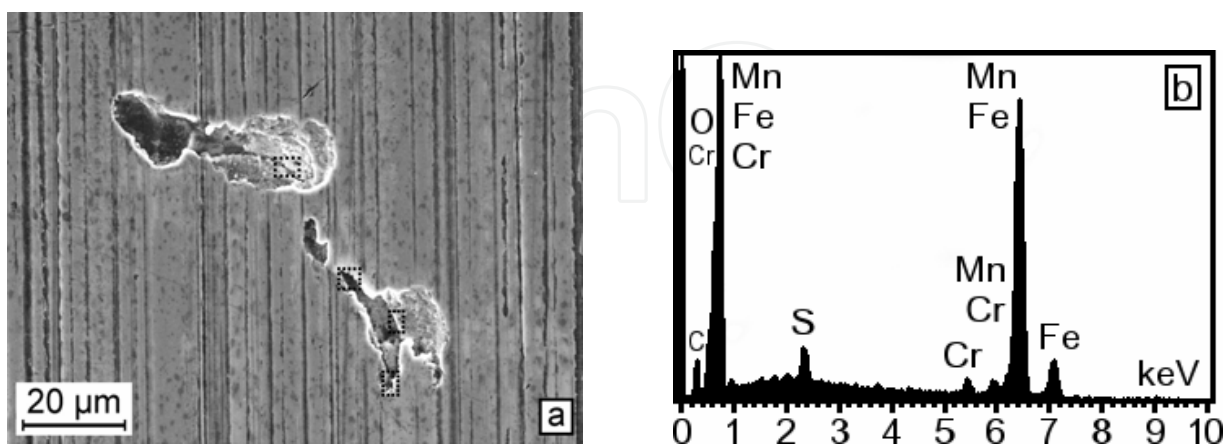

Fig. 42. Documentation of damage evolution by (a) a SEM-SE image of shallow material removals along dissolved MnS inclusions on the IR raceway of a TRB from an industrial gearbox with indication of four positions where EDX analysis reveals MnS residues and (b) EDX spectrum exemplarily of the analysis results recorded at the sites given in Figure 42a

The EDX reference analysis of bearing steel is provided in Figure 43. It allows comparisons with the spectra of Figures 39, 41b and 42b.
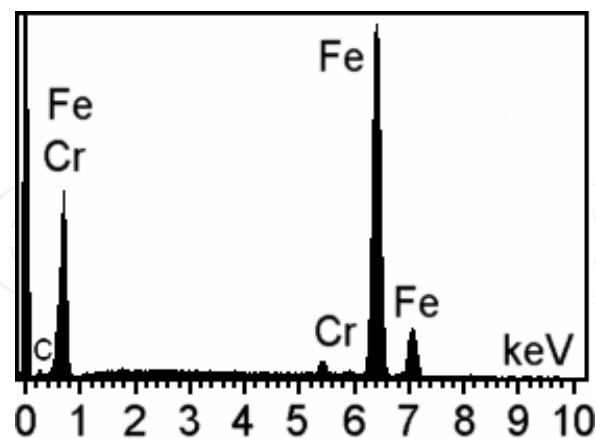

Fig. 43. EDX reference spectrum of bearing steel for comparison of the signals

5.3 Gray staining – Corrosion rolling contact fatigue

Gray staining by dense micropitting, well known as a surface damage on tooth flanks of gears, is also caused by mixed friction in rolling-sliding contact. The flatly expanded shallow material fractures of only few μm depth, which cover at least parts of an affected raceway, are frequently initiated along honing marks. In Figure 44a, propagation of material delamination to the right occurs into sliding direction. Typical features of the influence of corrosion are visible on the open fracture surfaces. The corresponding XRD material response analysis in Figure 44b shows that vibrational loading of the tribological contact can cause gray staining. Note that the shallow micropits do not affect the residual stress state considerably. The smoothed raceway of Fig. 44a, which indicates mixed friction, is virtually free of indentations. A characteristic type A vibration residual stress profile, maybe with some type B contribution in 100 μm depth (cf. Figures 33 and 36, z_0 much larger), is obtained. The XRD rolling contact fatigue damage parameter of $b/B \geq 0.83$ reaches or slightly exceeds the L_{10} equivalent value of 0.86 for the surface failure mode of roller bearings.
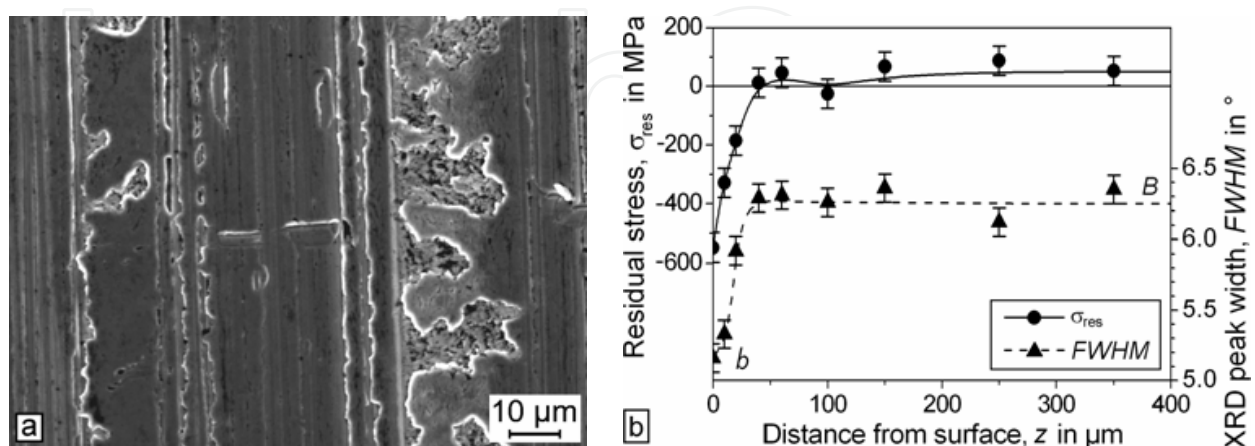

Fig. 44. Investigation of gray staining on the IR raceway of a CRB revealing (a) a SEM-SE image and (b) the measured type A vibration residual stress and XRD peak width distribution

The appearance of the micropits on the raceway is similar to shallow material removals on tribochemically dissolved MnS inclusions, as evident from a comparison of Figures 44a and 42a. Micropitting can occur on small cracks initiated on the loaded surface. The SEM image of Figure 45a indicates such causative shallow cracking induced by shear stresses, slightly inclined to the axial direction. The metallographic microsection in Figure 45b documents crack growth into the material in a flat angle to the raceway up to a small depth of few μm followed by surface return to form a micropit eventually.
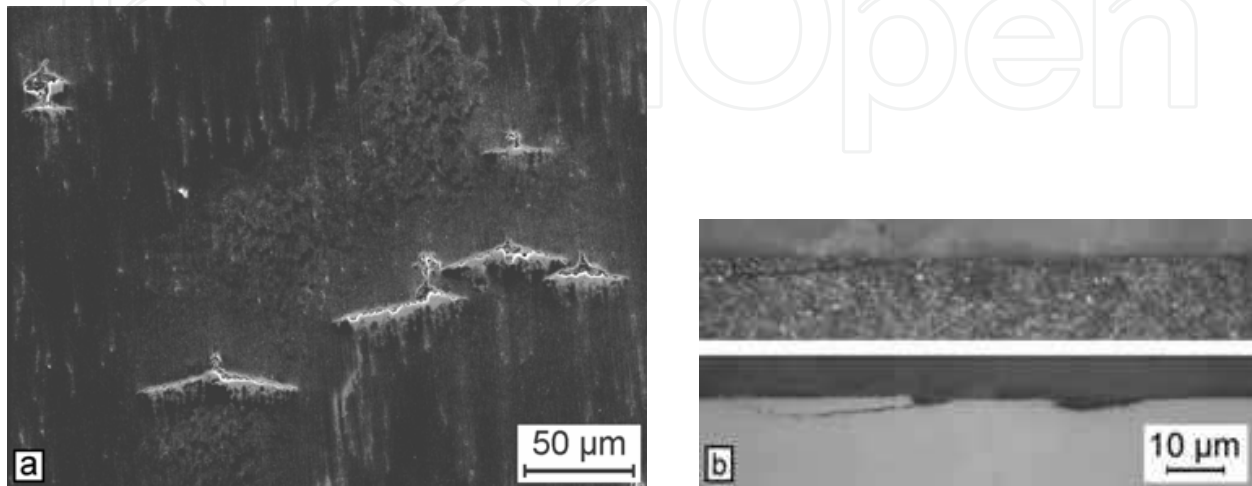

Fig. 45. Investigation of gray staining on the IR raceway of a rig tested automobile gearbox DGBB revealing (a) a SEM-SE image and (b) LOM micrographs of the etched (top) and unetched section of a developing micropit

The SEM overview in Figure 46a illustrates how dense covering of the raceway with micropits results in the characteristic dull matte appearance of the affected surface. On the bottom left hand side of the detail of Figure 46b, damage evolution on axially inclined microcracks results in incipient material delamination. Micropitting on a honing groove illustrates typical band formation. Note that the b/B parameter is reduced on the raceway surface to 0.69.
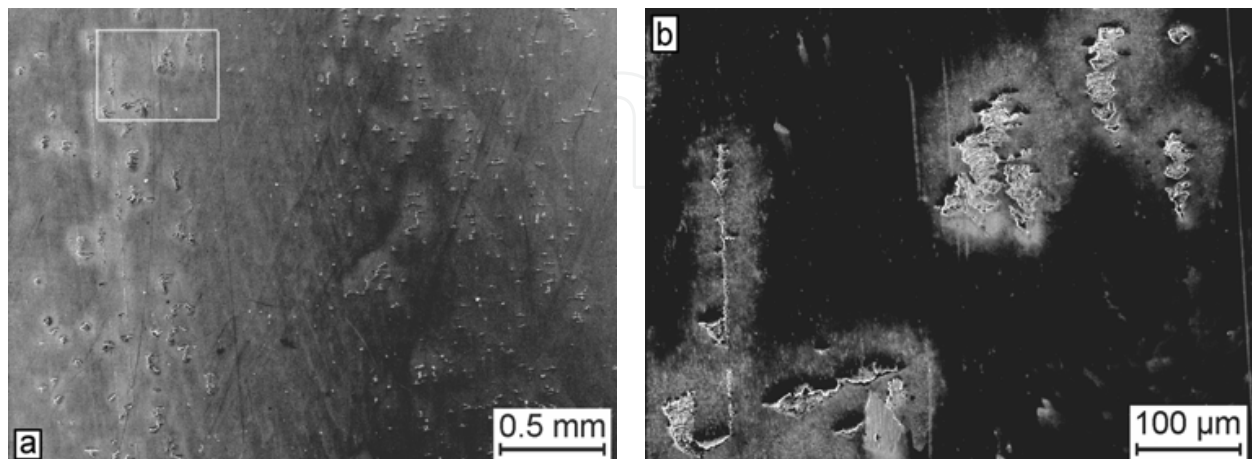

Fig. 46. Investigation of the smoothed damaged inner ring raceway of the deep groove ball bearing of Figure 45a presenting (a) a SEM-SE overview and (b) the indicated detail that reveals near-surface crack propagation in overrolling direction from the bottom to the top

Pronounced striations on the open fracture surfaces of micropits prove a significant contribution of mechanical fatigue to the crack propagation. The SEM details of Figures 47a and 47b confirm this finding. Therefore, it is concluded that a variant of corrosion fatigue is the driving force behind crack growth of micropitting in gray staining.
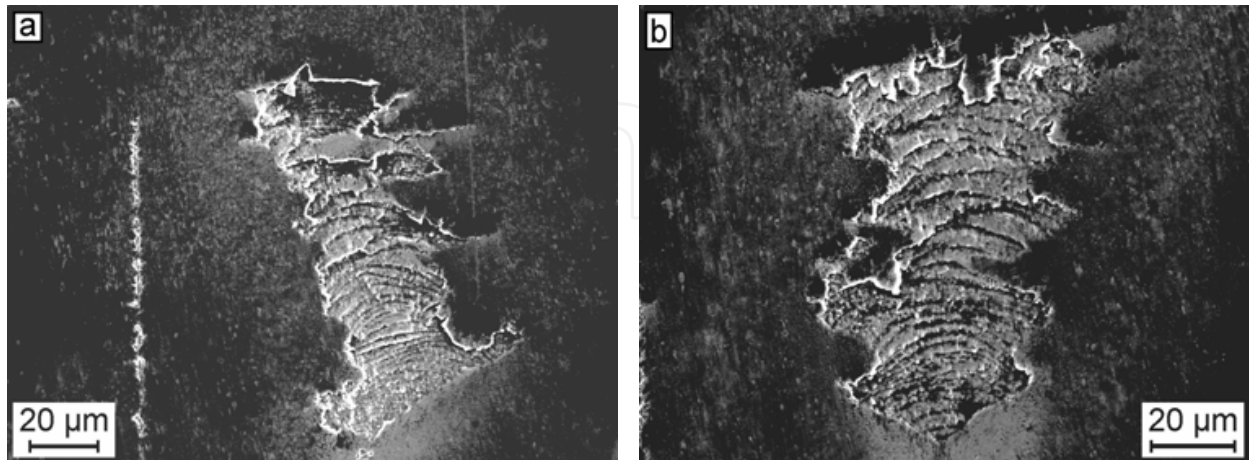

Fig. 47. SEM-SE details of the inner ring raceway of the deep groove ball bearing of Figure 46a revealing (a) distinct striations on a micropit fracture surface and (b) the same microfractographic feature on the open fracture face of another micropit

The additional chemical loading is not considered in fracture mechanics simulations of micropit formation by surface initiation and subsequent propagation of fatigue cracks (Fajdiga & Srami, 2009). The findings discussed above, however, suggest that gray staining can be interpreted as corrosion rolling contact fatigue (C-RCF).

5.4 Surface embrittlement in operation
Although quickly obscured by subsequent overrolling damage in further operation, shallow intercrystalline fractures are sporadically observed on raceway surfaces (Nierlich & Gegner, 2006). Illustrative examples are shown in the SEM images of Figures 48a and 48b.
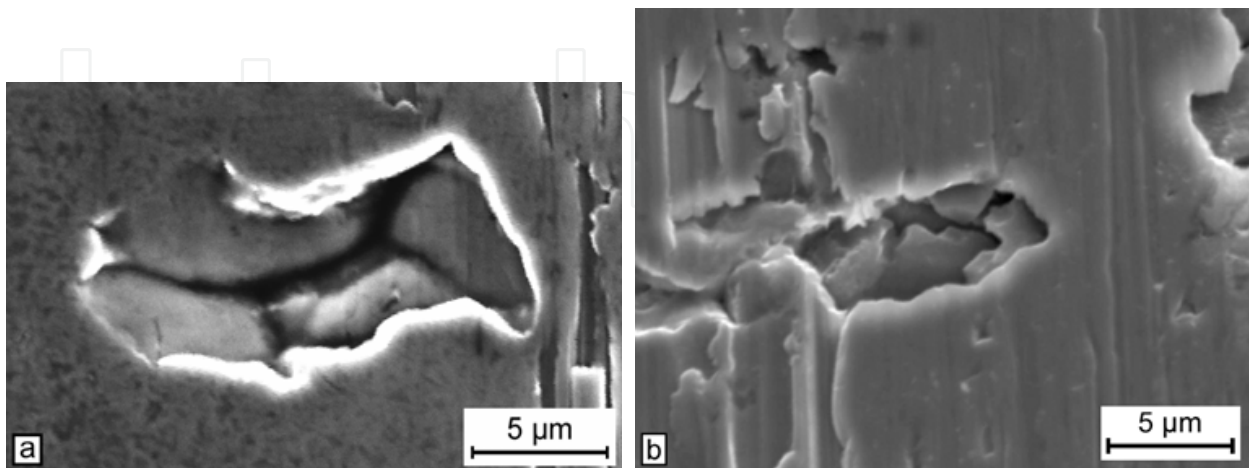

Fig. 48. SEM-SE images of the rolling contact surfaces of (a) a TRB roller and (b) a cam

The microstructure breaks open along former austenite grain boundaries. The affected raceway is heavily smoothed by mixed friction. Figure 48a and 48b characterize the lateral

surface of a roller from a rig tested TRB and gray staining on the cam race tracks of a camshaft, respectively. The even appearance of the separated grain boundaries points to intercrystalline cleavage fracture of embrittled surface material by frictional tensile stresses. The micropit on a raceway suffering from gray staining in Figure 49 suggests partly intercrystalline corrosion assisted crack growth. Striation-like crack arrest marks are clearly visible on the fracture surface. Microvoids in the indicated region point to corrosion processes (see section 5.3, C-RCF).
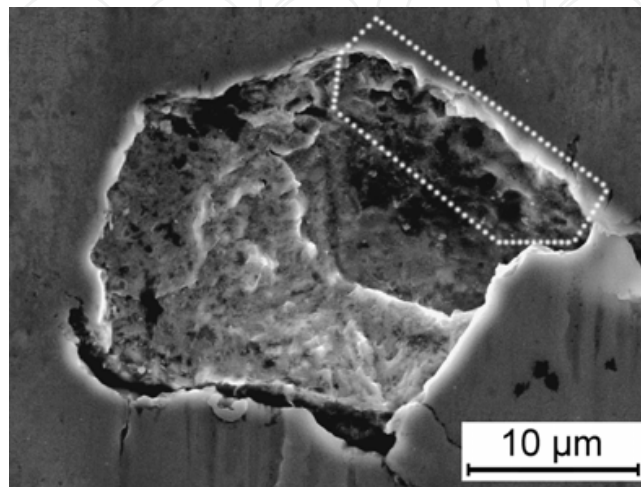

Fig. 49. SEM-SE image of a micropit on the IR raceway of a CRB from a field application

Possible mechanisms of gradual near-surface embrittlement during overrolling are (temper) carbide dissolution by dislocational carbon segregation (see section 4.2, Figure 22), carbide reprecipitation at former austenite or martensite grain boundaries, hydrogen absorption and work hardening by raceway indentations or edge zone plastification in the metal-to-metal contact under mixed friction. The occurrence of plate carbides, for instance, in micropits of gray staining is reported (Nierlich & Gegner, 2006). Due to lower chromium content than the steel matrix, these precipitates are obviously formed during rolling contact operation.

5.5 White etching cracks

Premature bearing failures, characterized by the formation of heavily branching systems of cracks with borders partly decorated by white etching microstructure, occur in specific susceptible applications typically within a considerably reduced running time of 1% to 20% of the nominal L_{10} life. Therefore, ordinary rolling contact fatigue can evidently be excluded as potential root cause, which agrees with the general finding that only limited material response is detected by XRD residual stress analyses. As shown in Figure 50, axial cracks of length ranging from below 1 to more than 20 mm, partly connected with pock-like spallings, are typically found on the raceway in such rare cases. For an affected application, for instance, it is reported in the literature that the actual L_{10} bearing life equals only six months, resulting in 60% failures within 20 months of operation (Luyckx, 2011).

Particularly axial microsections often suggest subsurface damage initiation. An illustrative example is shown in Figure 51.

In the literature, abnormal development of butterflies, material weakening by gradual hydrogen absorption through the working contact and severe plastic deformation in connection with adiabatic shearing are considered the potential root cause of premature

bearing damage by white etching crack (WEC) formation (Harada et al., 2005; Hiraoka et al., 2006; Holweger & Loos, 2011; Iso et al., 2005; Kino & Otani, 2003; Kohara et al., 2006; Kotzalas & Doll, 2010; Luyckx, 2011; Shiga et al., 2006). These hypotheses, however, conflict with essential findings from failure analyses (further details are discussed in the following). White etching cracks are observed in affected bearings without and with butterflies (Hertzian pressure higher than about 1400 MPa required, see section 3.3) so that evidently both microstructural changes are mutually independent. Depth resolved concentration determinations on inner rings with differently advanced damage show that hydrogen enrichment occurs as a secondary effect abruptly only after the formation of raceway cracks by aging reactions of the penetrating lubricant, i.e. rapidly during the last weeks to few months of operation but not continuously over a long running time (Nierlich & Gegner, 2011). Hydrogen embrittlement on preparatively opened raceway cracks, reflected in an
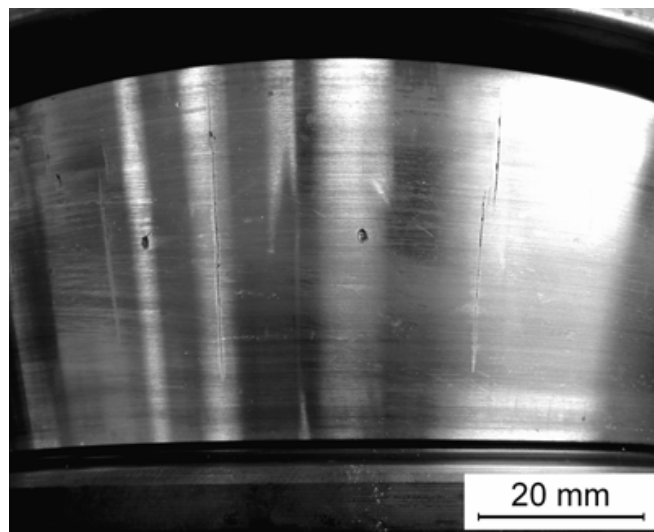

Fig. 50. Macro image of the raceway of a martensitically hardened inner ring out of bearing steel of a taper roller bearing from an industrial gearbox
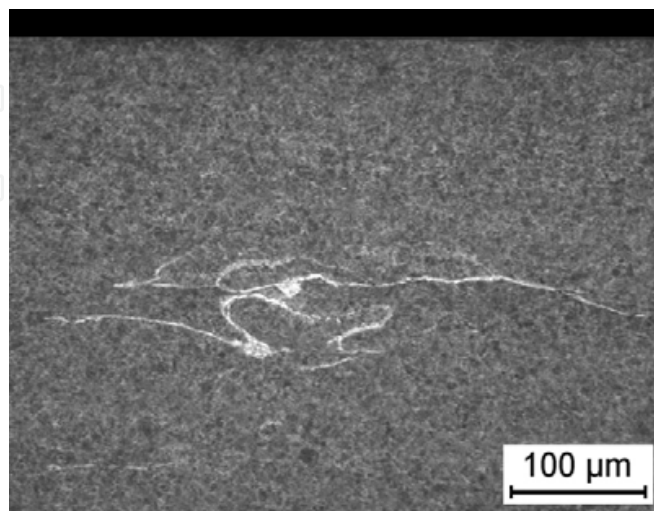

Fig. 51. LOM micrograph of the etched axial microsection of the bainitically hardened inner ring of a spherical roller bearing from a crane lifting unit

increased portion of intercrystalline fractures, is restricted to the surrounding area of the original cracks (Nierlich & Gegner, 2011). The undamaged rolling contact surface is protected by a regenerative passivating reaction layer. Adiabatic shear bands (ASB) develop by local flash heating to austenitising temperature due to very rapid large plastic deformation characteristic of, for instance, high speed machining or ballistic impact. Such extreme shock straining conditions obviously do not arise during bearing operation. WEC reveal strikingly branched crack paths, whereas ASB form essentially straight regular ribbons of length in the mm range. Adiabatic shearing represents a localized transformation into white etching microstructure possibly followed by cracking of the brittle new ASB phase. WEC evolve contrary by primary crack growth. Parts of the paths are subsequently decorated with white etching constituents.

The spidery pattern of the white etching areas in Figure 51 indicates irregular crack propagation prior to the microstructural changes on the borders. Equivalent stresses reveal uniform distribution in the subsurface region. The reason for the appearance of Figure 51 is the spreading and branching growth of the cracks in circumferential orientation. Cracks originated subsurface usually do not create axial raceway cracks but emerge at the surface mostly as erratically shaped spalling (cf. Figure 2b). Targeted radial microsections actually reveal the connection to the raceway. Figure 52 points to surface WEC initiation due to the overall orientation and depth extension of the crack propagation in overrolling direction from left to right. One can easily imagine how damage pattern similar to Figure 51 occur in accidentally located etched axial microsections.
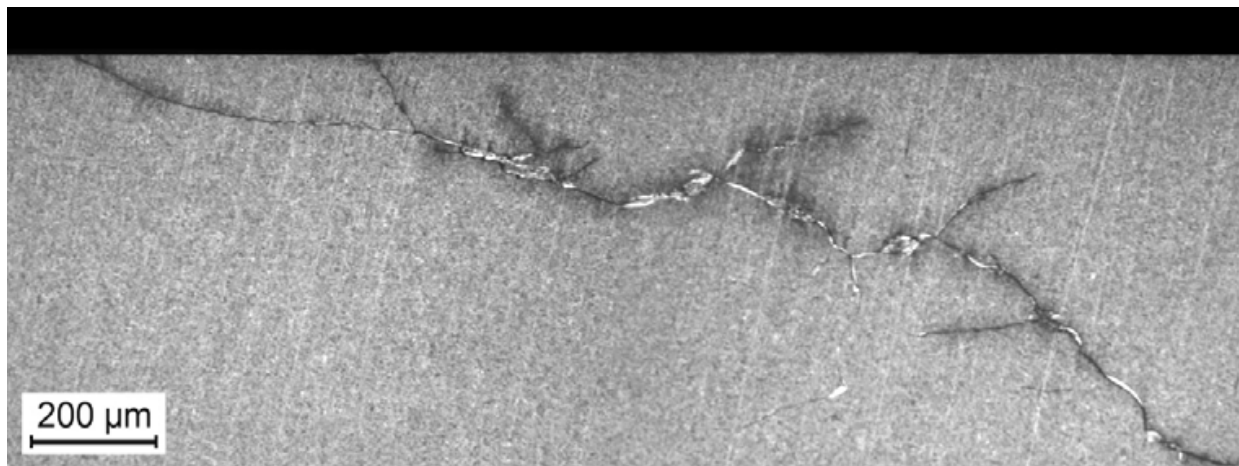

Fig. 52. LOM micrograph of the etched radial microsection of the case hardened inner ring of a CARB bearing from a paper making machine. The overrolling direction is left-to-right

Another example is shown in Figure 53a. The overrolling direction is from left to right so that crack initiation on the surface is evident. Figure 53b reveals the view of the edge of this microsection. No crack is visible at the initiation site on the raceway in the SEM (see section 5.5.1) so that also the detection probability question arises. The intensity of the white microstructure decoration of individual crack segments depends, for instance, on the depth (e.g., magnitude of the orthogonal shear stress) and the orientation to the raceway surface (friction and wear between the flanks). The pronounced tendency of the propagating cracks to branch indicates no pure mechanical fatigue but high additional chemical loading. Together with the regularly observed transcrystalline crack growth, this is typical of corrosion fatigue.
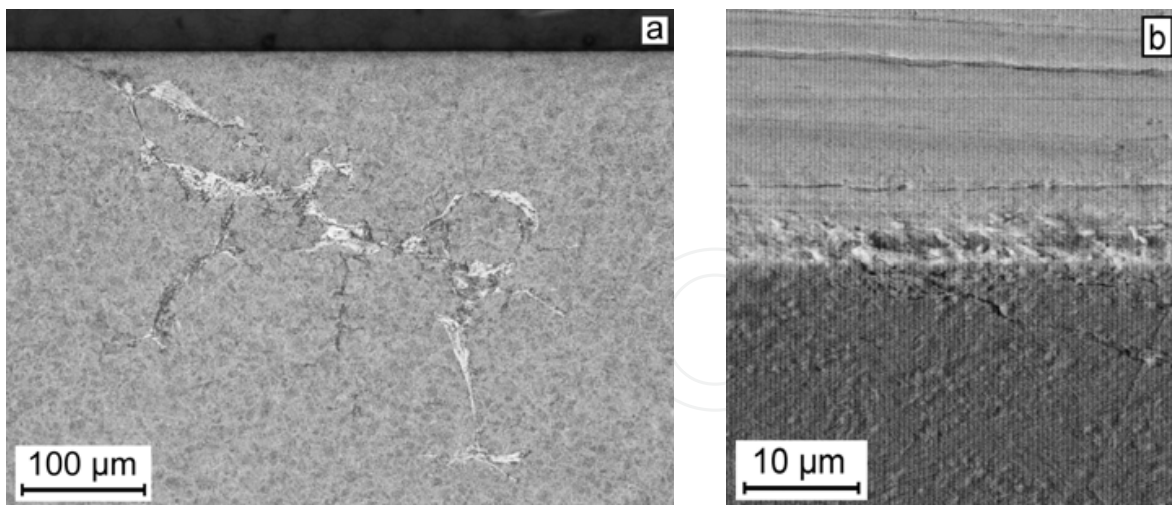
Fig. 53. Investigation of a white etching crack system in the martensitically hardened inner ring of a taper roller bearing from a coal pulverizer revealing (a) a LOM micrograph of the etched radial microsection (overrolling direction from left to right) and (b) a near-surface SEM detail (backscattered electron mode) of the view of the edge of the same microsection

5.5.1 Shear stress induced surface cracking and corrosion fatigue crack growth

Mixed friction in rolling-sliding contact can cause surface cracks on bearing raceways. The shear stress induced initiation mechanism is introduced first. The result of the XRD material response analysis performed on both raceways of a double row spherical roller bearing is depicted in Figures 54a and 54b.
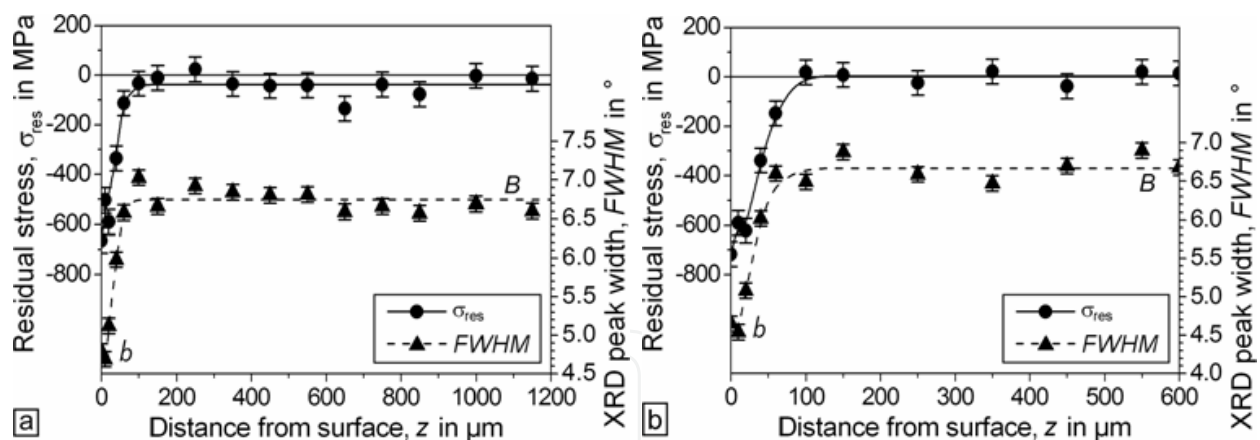

Fig. 54. Material response analysis showing a type A vibration residual stress and XRD peak width distribution below (a) the first and (b) the second raceway surface of the inner ring of a prematurely failed double row spherical roller bearing from a paper making machine

No subsurface changes of the XRD parameters occur. Note that for a Hertzian pressure of p_0=2500 MPa, i.e. incipient plastic deformation in pure radial contact loading, the z_0 depths of maximum v. Mises and orthogonal shear stress equal about 1.15 and 0.85 mm, respectively. Load induced butterfly microstructure transformations on nonmetallic inclusions are not observed in metallographic microsections of this large size roller bearing. Therefore, the maximum applied Hertzian pressure actually does not exceed about 1400 MPa (see section 3.3). Compressive residual stresses are formed near the surface up to a

depth of around 60 μm. The original loading conditions relevant to damage initiation are not obscured by overrolling of spalls at a later stage of failure and only isolated indentations are found on the raceway. The characteristic type A residual stress profile in Figures 54a and 54b thus identifies the impact of vibrations. On the surface, advanced material aging of *b/B*≥0.69 is deduced.

Incipient hairline cracks on the raceway are almost undetectable even in the SEM. The virtually perspective view of the edge of a microsection in Figure 55 provides an example (cf. Figure 53b). A corresponding micrograph of the etched microsection is shown in Figure 56.
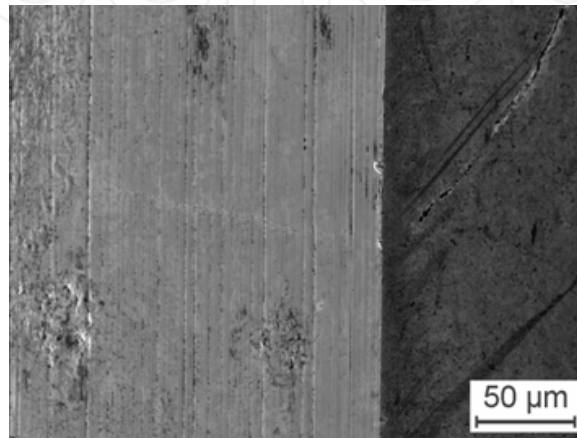

Fig. 55. SEM-SE image of a hairline crack initiation site on the smoothed raceway surface and incipient fatigue crack growth into the material in overrolling direction from bottom to top visible in the cut microsection on the right. The SRB failure of Figure 54 is investigated
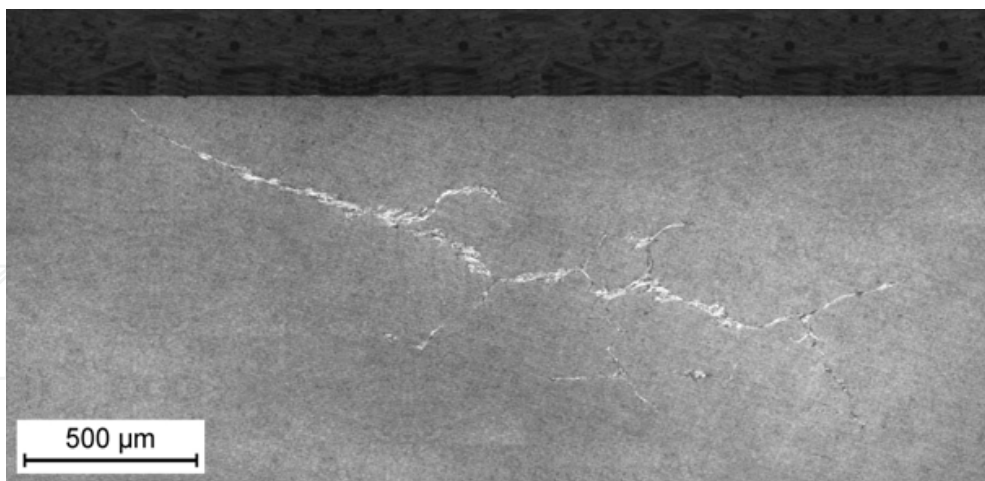

Fig. 56. LOM micrograph of the etched metallographic section on the right of Figure 55. The raceway surface is at the top of the image. The overrolling direction is from left to right

Shear stress control of surface fatigue crack initiation, under varying load and friction-defining slip in the contact area, and subsequent propagation is apparent from crack advance in overrolling direction in a small angle to the raceway tangent. The mechanism is particularly evident from the unbranched crack in Figure 57. The inset zooms in on the edge zone. Compressive residual stresses near the surface (cf. Figure 54) demonstrate the effect of

shear stresses required for crack development. According to Figure 58, extended white etching crack systems up to a depth of more than 1 mm are formed, where crack returns to the raceway result in pitting by break-out of the surface eventually. Note that in Figures 56 to 58, the overrolling direction from left to right strikingly indicates top-down WEC propagation.
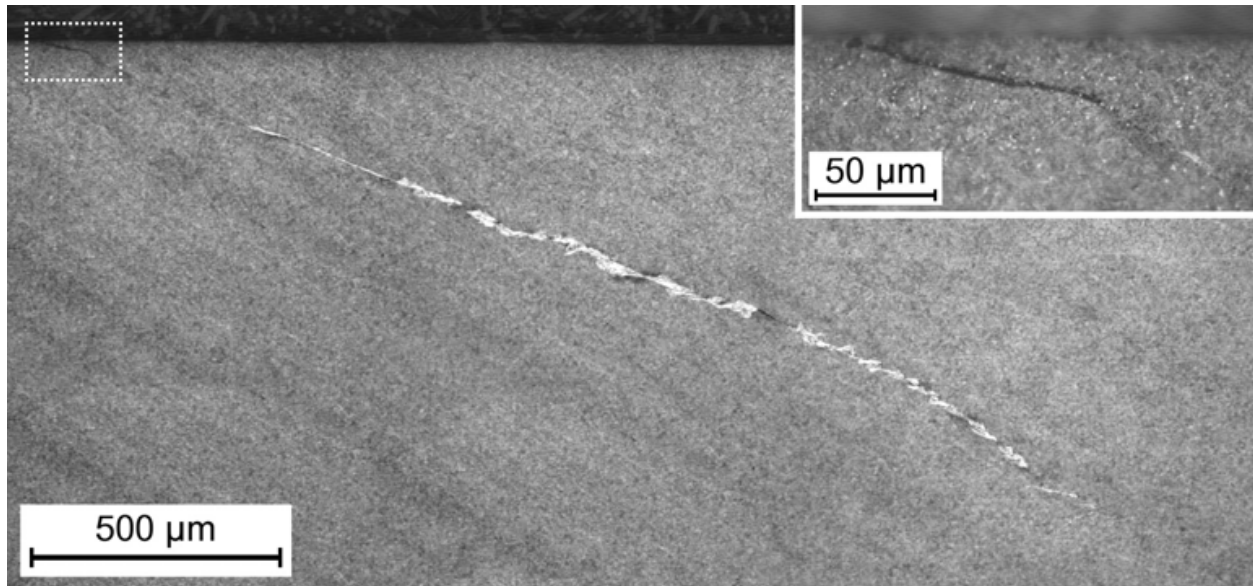

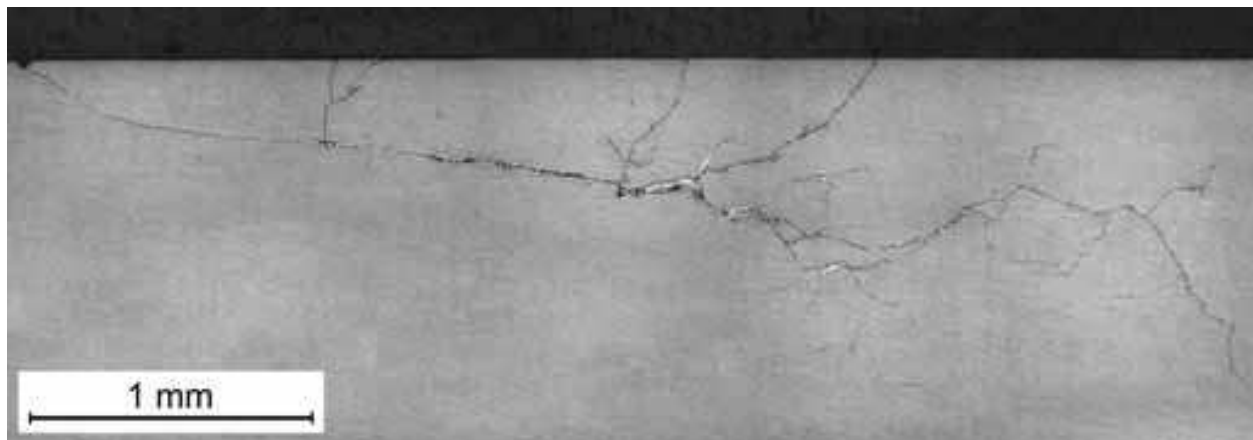Fig. 57. Same as Figure 56, another crack. The overrolling direction is from left to right

Fig. 58. Same as Figure 56, another WEC system. The overrolling direction from left to right and the orientation of repeated branching proves top-down growth of the CFC crack

Pronounced branching and deep, widely spreading propagation of the transcrystalline cracks essentially under moderate mechanical load of typically $p_0 \approx 1500$ MPa reveals corrosion fatigue in rolling contact as the driving force of crack growth. A comparison of Figure 56 and 57 suggests that also fracture of the new brittle ferritic phase can lead to the initiation of side cracks. Local phase transformation into white etching microstructure along the crack paths is caused by hydrogen (HELP mechanism) released from the highly stressed penetrating lubricant to the adjacent steel matrix. Wear between the crack flanks promotes the degradation reactions on blank metal faces (Kohara et al., 2006). Oil additives can

influence the tribochemical release of hydrogen. Accelerated lubricant aging due to vibration loading further supports the chemical assistance of corrosion fatigue cracking (CFC) and microstructure transformation into white etching constituents. Local material aging and embrittlement is manifested in the frequently observed formation of a dark etching region around the cracks. An example is given in the micrograph of Figures 59a. Regular etching induced preparative cracking along the branching CFC path in the corresponding SEM image of Figure 59b reflects plastification in the slip bands of the embrittled DER material.
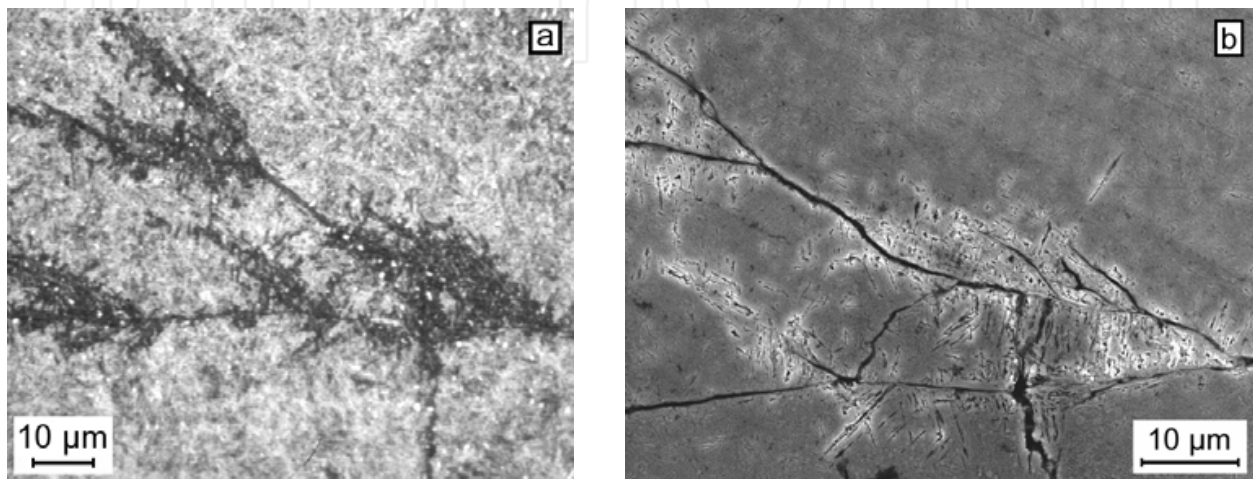

Fig. 59. DER around CFC crack paths indicate localized material aging in (a) a LOM and (b) a SEM micrograph of an etched microsection of the IR of a TRB from an industrial gearbox
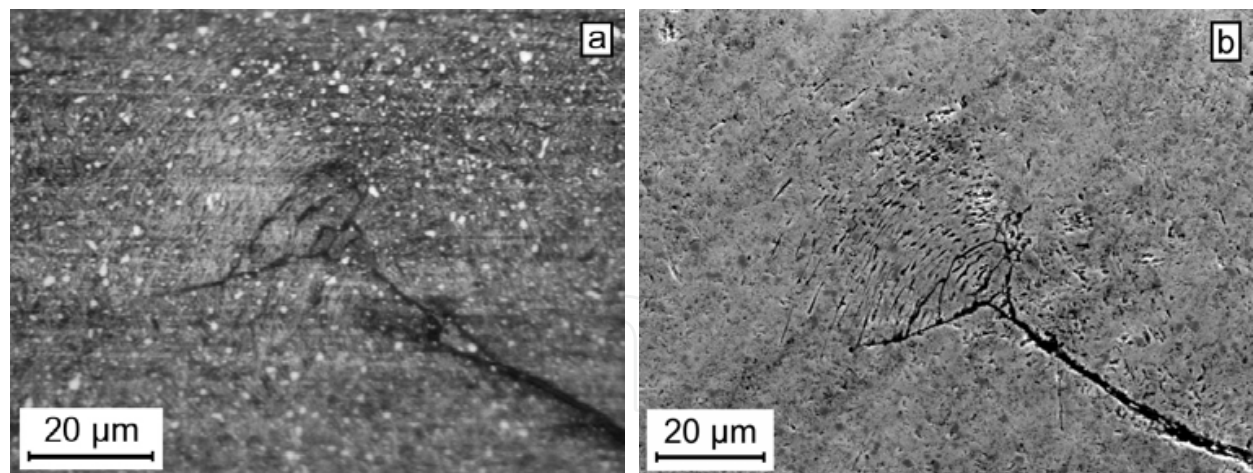
Fig. 60. Carbide dissolution and distinct localized plastification at the multi-branching tip of a CFC crack visible in (a) a LOM and (b) a corresponding SEM micrograph of an etched radial microsection of the inner ring of a cylindrical roller bearing from a weaving machine

Localized fatigue damage is promoted by hydrogen released from decomposition products and possibly contaminations of the lubricant, penetrating through the advancing crack from the raceway surface to the depth. The most intense microstructural changes thus occur on multi-branching sites of CFC cracks (cf. Figure 59). Particularly at these most effective hydrogen sources, pronounced carbide dissolution (see DGSL model, section 4.2) in the

proceeding phase transformation is visible in the microsection. The region of the heavily branching tip of a CFC crack in the LOM micrograph of Figure 60a provides an illustration. Localized plasticity in the area of carbide dissolution is evident from the corresponding SEM image of Figure 60b. Weaker material aging and incipient phase transformation (DER) also occurs along unbranched crack paths. The etching process emphasizes the actual microstructure damage. The secondary hydrogen embrittlement around CFC cracks, linked to DER formation, is reflected in the increased susceptibility of the locally aged steel matrix to preparative stress corrosion cracking, which from its first detection is referred to as *Zang* structure. The example of Figures 61a and 61b documents that the local dark etching region around corrosion fatigue cracks can be perceived as precursor of WEA (see also section 4.3). The developed banana-shaped WEA, surrounded by the preliminary DER structure, nestles to the CFC crack at a multi-branching site. Its harder material (more than 1000 HV) appears smoothed and darker in the SEM detail of Figure 61b, where texturing is indicated by reorientation of the included cracks.

The observation of enhanced, evidently hydrogen induced phase transformation at (multi-) branching sites agrees with regular finding of pronounced white etching area decoration at these positions of WEC systems. Note that in Figure 61, the match of the curved shape of the WEA with the crack path excludes primary WEA evolution.

Fig. 61. Curved white etching area along a multi-branching site of a WEC with surrounding embrittled DER material, identified as WEA precursor, in (a) a LOM and (b) a SEM micrograph of an etched microsection of the inner ring of a TRB from an industrial gearbox
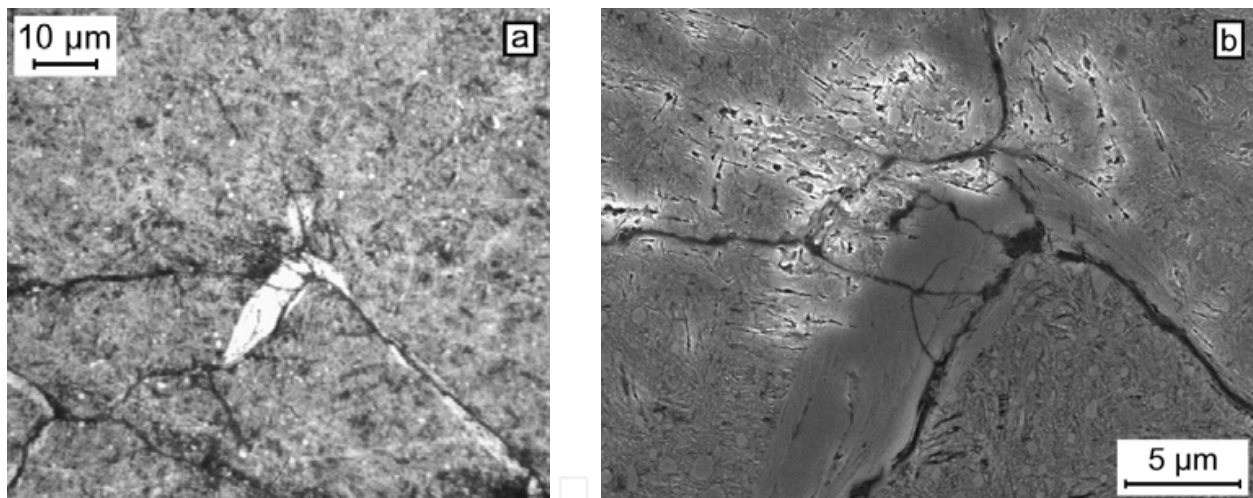
In the outer zone of the overrolled material, the shear stresses for dislocation glide in the described dynamic (nano-) recrystallization process of white etching microstructure formation around CFC cracks, which offer the hydrogen source for accelerated local fatigue aging, increase with depth. This is one reason why the decorating constituents in a WEC are often found less intense near the raceway surface (see, e.g., Figures 52, 56 and 57). The overall hydrogen content of 0.9 ppm measured at the inner ring of Figures 54 to 58 is consistent with the typical delivery condition. This finding reflects the limited damage of the investigated bearing. Depending on the density of the raceway cracks, gradual secondary hydrogen absorption from the surface to the bore is verified at the final stage of service life (Nierlich & Gegner, 2011).

Figure 62 completes the investigation of the SRB failure of Figures 54 to 58. The fracture face of a preparatively opened crack at the initiation site on the surface is shown. The inner ring raceway is visible at the top. Following the brittle incipient crack of about 5 µm depth, dense striations indicate the fatigue nature of crack propagation almost from the surface.
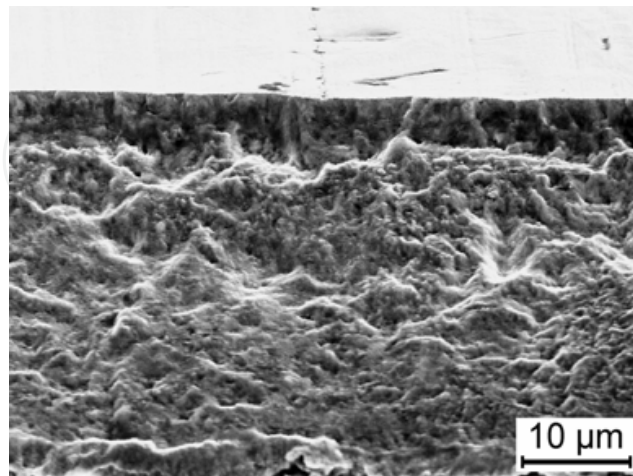

Fig. 62. SEM-SE fractograph of the original fracture surface of a subsequently opened raceway crack on the inner ring of the spherical roller bearing of Figures 54 to 58

5.5.2 Frictional tensile stress induced surface cracking and normal stress hypothesis

Figure 63 reveals a micropit on the smoothed inner ring raceway of a CARB bearing from a paper making machine. Material removal is caused by a brittle Mg-Al-O spinel inclusion that breaks off from the surface under tribomechanical loading of the rolling-sliding contact.
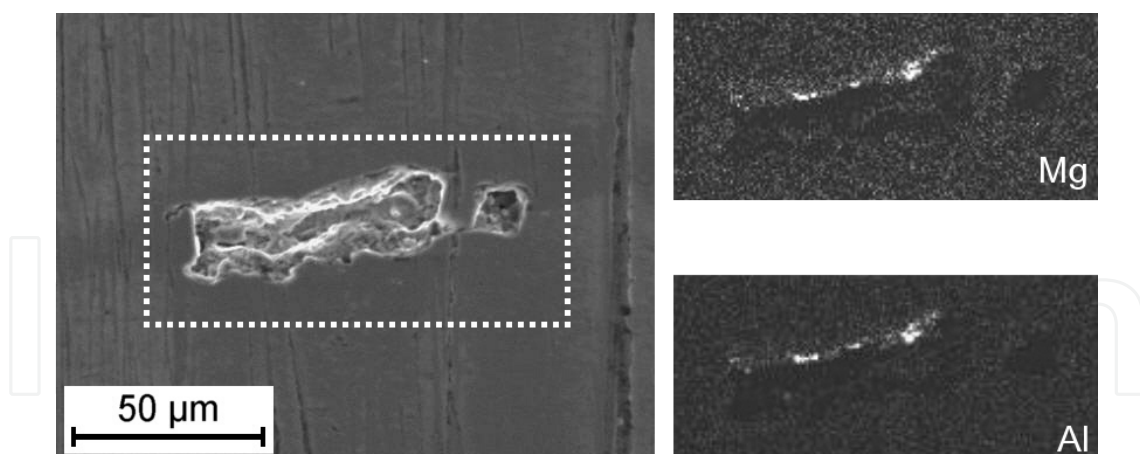
Fig. 63. SEM-SE image of the IR raceway of a CARB bearing and indicated elemental mapping (on the right) revealing an oxide inclusion (Al and Mg detected) that breaks off from the surface under frictional rolling contact loading to cause a micropit eventually

In Figure 63, the demonstrative elemental distribution images of magnesium and aluminum are mapped over the damaged region. Sharp-edged axial surface cracks on tribochemically dissolved MnS inclusions (see section 5.2, e.g. Figure 42a), which advance vertically downwards into the material (Nierlich & Gegner, 2006), as well as grain boundary cleavage (cf. Figure 48) further indicate the action of frictional tensile stresses. Another type of failure

causing loading by differently disturbed bearing kinetics is thus reflected in brittle spontaneous crack initiation on raceway surfaces.

Application of the tribological model introduced in section 5.1 in the inset of Figure 36 allows the estimation of the development of the frictional tangential normal stresses $\sigma_{yy}^{y=-a}$ with depth z. The classical analytical solution of a uniform infinite rolling-sliding line contact (Karas, 1941), for the highest tension level evaluated at the runout $y=-a$, is used for the approximation ($\mu=\mu_>$):

$$\frac{\sigma_{yy}}{p_0} = \sinh\alpha\sin\beta\left(1 - \frac{\sinh 2\alpha + \mu\sin 2\beta}{\cosh 2\alpha - \cos 2\beta}\right) - (\sin\beta - 2\mu\cos\beta)\exp(-\alpha) \tag{7}$$

$$\sinh\alpha = \frac{1}{a}\sqrt{\frac{1}{2}\left[y^2 + z^2 - a^2 + \sqrt{(y^2 + z^2 - a^2)^2 + 4a^2z^2}\right]}, \text{ for } -a \le y \le 0 \tag{8}$$

$$y = a\cosh\alpha\cos\beta, \ \alpha \ge 0 \tag{9}$$

$$z = a\sinh\alpha\sin\beta, \ \beta \ge 0 \tag{10}$$

The relationships of Eqs. (9) and (10) hold for the elliptic coordinates. Figure 64 shows a graphical representation of calculated depth distributions for increased friction coefficients μ of 0.2, 0.3 and 0.4. On the raceway surface at $z=0$, maximum tension of $2\mu p_0$ is reached.
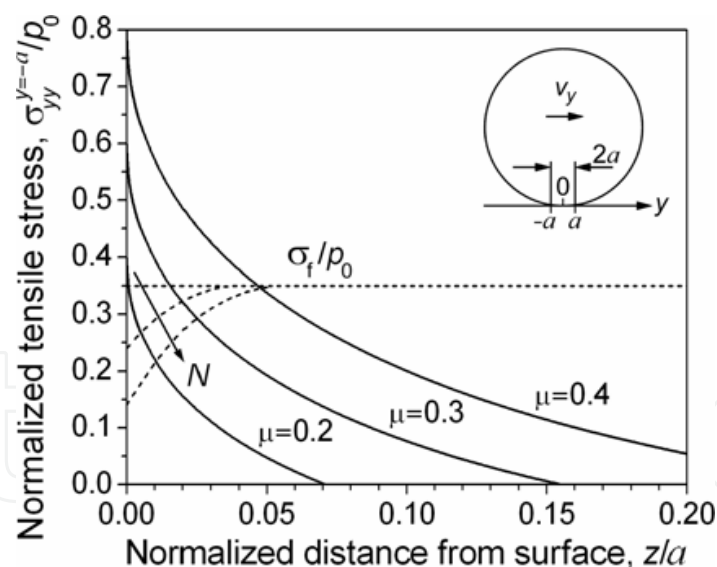
Fig. 64. Normalized distribution of the equivalent normal stress below a rolling-sliding contact (rolling occurs in y direction at velocity v_y, see inset) and indication of the level of the critical fracture strength $\sigma_f \approx R_e$ for typical peak loading with illustration of the expanding failure range by gradual in-service surface embrittlement (cf. section 5.4) with running time

Note that Figure 1 represents the stress field in the center of the Hertzian contact area. At the runout ($y=-a$, see inset of Figure 64), where the maximum sliding friction induced circumferential tensile stresses of Eq. (7) occur in the surface zone of the material, the hydrostatic pressure reduces to zero. A graphical illustration is provided in Figure 65.

Fig. 65. Schematic representation of the macro contact area with elliptical Hertzian distribution of the pressure p (maximum p_0 in the center is indicated)

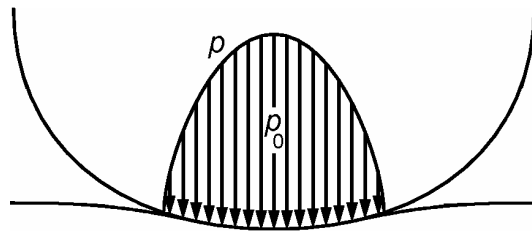Preferential surface cracking occurring vertically in axial direction on raceways of larger roller bearings (providing high a values) that run under (intermittently) increased mixed friction points to the validity of a normal stress fracture criterion (Nierlich & Gegner, 2011):

$$\sigma_e^{nsh} = \sigma_{yy}^{y=-a} \tag{11}$$

Modification of the equivalent normal stress σ_e^{nsh}, for instance by residual stresses (e.g. from surface finishing or cold working, cf. Figures 16a and 23a) or stress raising nonmetallic inclusions, is neglected in Figure 64 for the sake of simplicity. In a rough approximation, the relevant critical fracture strength σ_f of brittle spontaneous crack initiation is, due to almost deformationless material separation (see Figures 66 and 67 later in the text), estimated as the elastic limit $R_e \approx 800$ MPa, which falls significantly below the yield strength for hardened bearing steel. In cyclic tension-compression tests, for instance, the material changes its response from elastic to microplastic at a stress level around 500 MPa (Voskamp, 1996). The failure range of the introduced normal stress hypothesis can then be determined as follows:

$$\sigma_{yy}^{y=-a} \geq \sigma_f \tag{12}$$

As spontaneous incipient crack formation is considered, the illustration of Figure 64 realistically refers to short-term loading of high Hertzian pressure $p_0 \geq 2000$ MPa and friction coefficient $\mu \geq 0.2$. Rough indication of the relative σ_f/p_0 level occurs accordingly. Note that the exact magnitude of the fracture strength $\sigma_f \leq R_{p0.2}$ does not make an essential difference to the validity of the introduced normal stress failure hypothesis but only influences the frequency of the rare events of raceway cracking as critical peak load operating conditions can cause tensile stresses $2\mu p_0 \approx 2000$ MPa on the surface. The length of the brittle mode I propagation of a frictionally initiated cleavage-like raceway crack depends on the stress intensity factor K_I and the fracture toughness K_{Ic} according to $K_I > K_{Ic}$. The depth effect of operational material embrittlement (see section 5.4) on the critical fracture strength σ_f (also valid for K_{Ic}), which increases with the number N of ring revolutions, is schematically included in Figure 64, where larger size bearings with a in the range of 0.5 mm are considered. A concrete calculation example is given in the literature (Nierlich & Gegner, 2011). The semiminor axis a of the contact ellipse influences the extension of the failure range according to Eq. (12) and Figure 64. The micro friction model of Figure 36 is regarded. As deduced in section 5.1 from the effect of the induced equivalent shear stresses on plastification and the resulting type A or B residual stress patterns, vibrational loading can intermittently cause locally increased mixed friction. Under peak load operating conditions, such short-term states generally coincide with the impact of high Hertzian pressures. As the detection of type A residual stress distributions (see Figure 54) indicates, friction coefficients

above 0.3 can occur temporarily in subareas of the rolling contact. Larger size roller bearings are most sensitive to brittle cracking.

Further fractographic verification of normal stress failures is provided in the following. The steep gradient of the causative frictional tensile stress in Figure 64 indicates limited advance and rapid stop of an initiated brittle spontaneous mode I surface crack. The fracture faces of two preparatively opened vertical axial raceway cracks in the SEM images of Figures 66 and 67 confirm this prediction. The development of the (semi-) circular shape of the spontaneous cracks may be described by the depth dependence of the stress intensity factor and an energy balance criterion to minimize the interface energy.
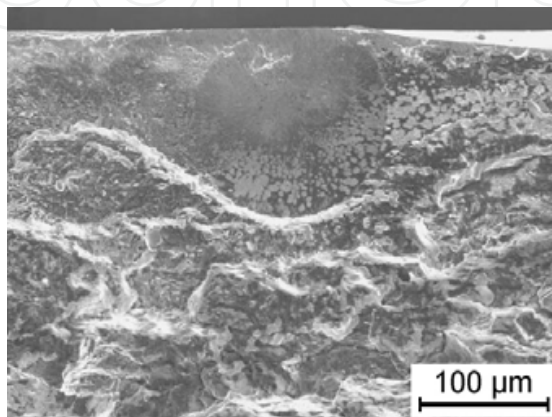

Fig. 66. SEM-SE fractograph of the original fracture surface of a preparatively opened axial crack on the inner ring raceway of a failed taper roller bearing from an industrial gearbox
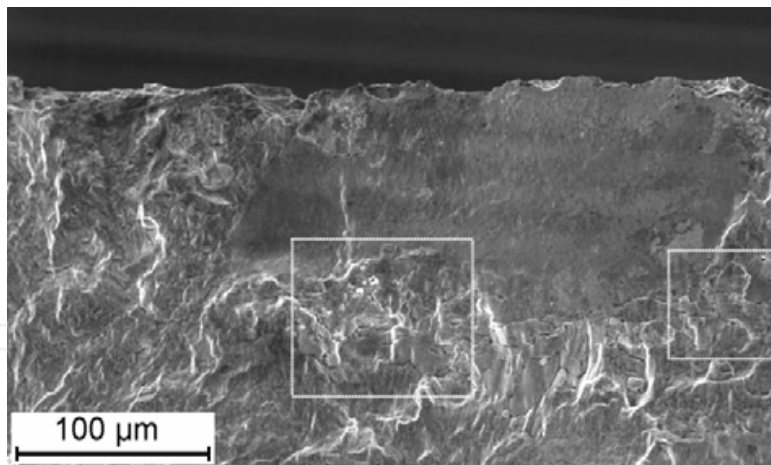
Fig. 67. SEM-SE fractograph of the original fracture surface of a preparatively opened axial crack on the inner ring raceway of a failed taper roller bearing from an industrial gearbox

The low-deformation transcrystalline lenticular cracks of about 150 μm depth act as incipient cracks of subsequent corrosion fatigue cracking into the depth, to the sides and on the surface. The distinct change of the fracture pattern in Figures 66 and 67, respectively with a demarcating bulge or crack network, on the latter of which Figures 68a and 68b zoom in, is evident. The crack arrest indicating numerous side cracks in Figure 68 reflect local material embrittlement as observed in the affected DER microstructure around CFC cracks in the SEM micrographs of etched microsections in Figures 59b and 60b.

Fig. 68. SEM-SE details of Figure 67 as indicated (a) in the lower middle and (b) on the right

In the area of the spontaneous crack of Figure 66, a mixed TiCN-MnS nonmetallic inclusion near the raceway surface in a depth of about 25 μm acts as stress ra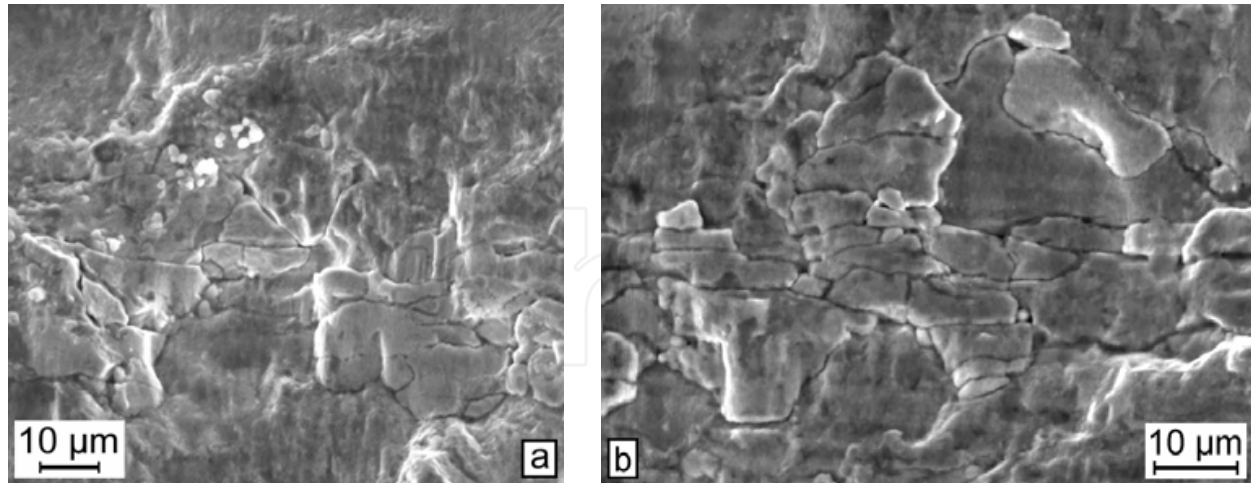ising crack nuclei. The appearance of the microsections, revealing white etching crack systems, is similar to Figures 56 to 61.

Hydrogen releasing aging reactions of the lubricant during corrosion fatigue crack growth are proven by EDX microanalysis on preparatively opened fracture surfaces. As an example, Figure 69a shows an overview of the deep CFC region below the brittle lenticular crack of Figure 67. The area of the performed EDX analysis is marked in the SEM fractograph. Sulfur, phosphorus and zinc in the recorded spectrum of Figure 69b indicate reacted residues of oil additives near the crack tip in a depth of about 1 mm in higher concentration than on the low-deformation spontaneous incipient crack visible at top left of Figure 69a, where chemical attack is restricted to subsequent surface corrosion. Furthermore, numerous side cracks characterize corrosion fatigue fracture faces (see also, for instance, the microsections of Figures 56, 58 and 59). The forced rupture from preparative crack opening stands out clearly at the bottom and bottom left of Figure 69a against the dark original CFC fracture structure.

The bearing applications of Figures 66 and 67 operate under vibrations. The observed local crack initiation on the raceway agrees with the approach of the tribological model in Figure 36 that subdivides the contact area into regions of different loading levels. Brittle spontaneous cracking occurs in subdomains of increased friction coefficient. Compared with the competing fatigue crack initiation mechanism discussed in section 5.5.1, lower slip in the moment of surface cracking is suggested.

It is worth noting that post-machining thermal treatment (PMTT) of ground and honed rings and rollers, previously proposed in the literature for material reinforcement in the mechanically influenced edge zone (Gegner, 2006b; Gegner et al., 2009), is recently reported to be an effective countermeasure against premature bearing failures by white etching crack formation (Luyckx, 2011). The short reheating process of, e.g., 0.5 to 1 h after the finishing operation occurs below the tempering or transformation temperature to avoid undesired hardness loss (cf. section 4.2, Figure 23). As only the plastically deformed material in the outermost layer up to a depth of about 10 μm is microstructurally stabilized, a success of this simple treatment would provide further indication of surface WEC failure initiation.
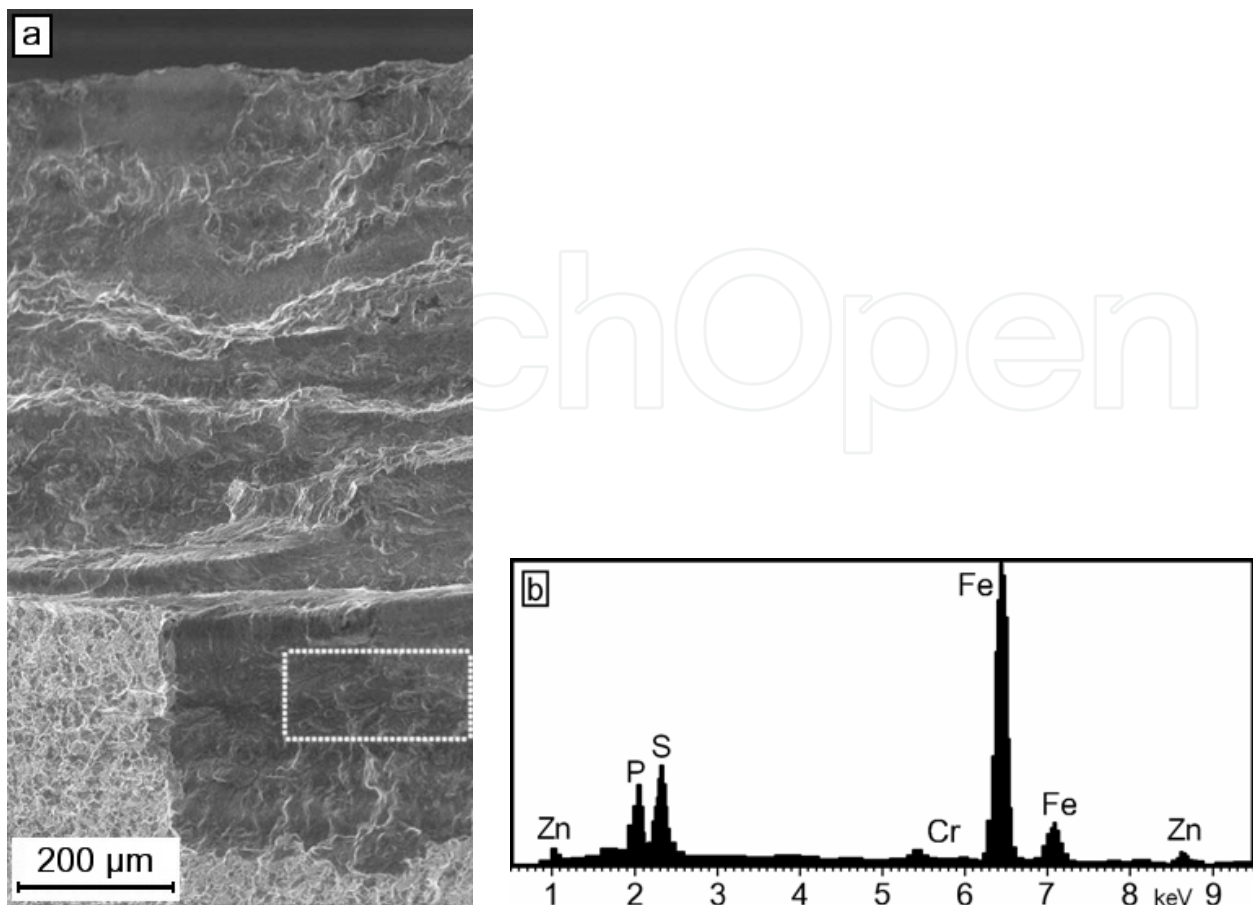
Fig. 69. Investigation of the fracture surface of Figure 67 in the deep corrosion fatigue crack region revealing (a) a SEM-SE fractograph and (b) the EDX spectrum taken at the indicated position where the presence of the tracer elements S, P and Zn of the oil additives proves the assistance of fatigue crack growth by chemical reactions, i.e. CFC, in a depth of 1 mm

6. Conclusion

The present chapter deals with important aspects of rolling contact tribology in bearing failures. Following the introduction, the fundamentals are presented in sections 2 and 3. The subsurface and (near-) surface failure modes of rolling bearings are outlined. X-ray diffraction (XRD) based residual stress analysis identifies the depth of highest loading and provides information about the material response and the stage of damage. The measurement technique, evaluation methodology and application procedure are discussed in detail. The loading induced reduction of the XRD peak width ratio b/B of minimum to initial value is used as a life calibrated measure of material aging to correlate the successive microstructural changes during rolling contact fatigue (RCF) with the Weibull bearing failure distribution. Therefore, it also permits the prediction of gradual alterations of the hardened steel matrix, which are roughly assigned to the corresponding bearing life in the final phase of the three stage model of RCF (shakedown, steady state, instability). Strong indication is given that dark etching regions (DER) from martensite decay act as the precursor of subsequently occurring ferritic white etching areas (WEA). The WEA are formed in regular parallel flat (30°) and steep (80°) bands within the aged matrix or along propagating corrosion fatigue cracks. Rolling contact fatigue in the subsurface region can

also occur on nonmetallic inclusions. The generation and growth of butterflies are briefly discussed, based on recent findings.

Section 4 focuses on classical subsurface RCF, which may lead to fatigue wear. Raceway spalling is initiated by cracks from the depth of the material eventually. The microstructural changes that characterize the progression of subsurface rolling contact fatigue in the steel matrix are metallographically examined, including scanning electron microscopy. A distinction is made from the shakedown stage during the short running-in period, which is identified as a cold working process of local (micro-) plastic deformation. Rapid compressive residual stress formation in this phase, in response to the exceedance of the yield strength by the v. Mises equivalent stress at Hertzian pressures above 2500 to 3000 MPa, occurs without visible microstructural alterations, the development of which requires carbon diffusion. The mechanistic metal physics dislocation glide stability loss (DGSL) model of rolling contact fatigue is introduced and examined by reheating experiments. As a new aspect of material damage by severe in-service high-frequency electric current passage through bearings, continuous absorption of hydrogen is found to accelerate subsurface RCF. Steep white bands that occur not until the L_{50} life (50% failure probability) in pure mechanical loading appear earlier at much lower b/B reduction in chemically promoted rolling contact fatigue. The accelerating effect of dissolved hydrogen is demonstrated by a comparison of the microstructures at $b/B \approx 0.71$, also considering cold working. The chosen reference level is yet above the XRD equivalent value of $b/B \approx 0.64$ of the rating L_{10} bearing life in pure mechanical subsurface rolling contact fatigue. The additional chemical loading accelerates material aging by enhancing the dislocation mobility and microplasticity, as evident from the DGSL model. Hydrogen absorption also causes crack initiation in the pre-embrittled microstructure by interfacial delamination at white etching bands that is not observed in pure mechanical RCF.

In section 5 of the present chapter, the effect of mixed friction in the rolling contact area, which occurs frequently in bearing applications, is discussed in detail. Smoothing of the machining marks by polishing wear on the raceway is a characteristic visual indication. Several mechanisms of mixed friction induced failure initiation are introduced. The impact of externally generated three-dimensional mechanical vibrations represents a common cause of disturbed elastohydrodynamic lubrication conditions. Larger size roller bearings operating typically at low to moderate Hertzian pressure are most susceptible to frictional surface loading. Tangential forces by sliding friction acting on a rolling contact increase the v. Mises equivalent stress and shift its maximum, i.e. the position of incipient plastic deformation, toward the surface. The resulting build-up of compressive residual stresses in the edge zone at Hertzian pressures below 2500 MPa is observed for indentation-free raceways under the action of, e.g. engine, vibrations in operation. Material response is described by a tribological model that partitions the contact area into microscopic subdomains of intermittently different friction coefficients up to peak values above 0.3. The distinguishable type A and B vibrational residual stress distributions are explained. Vibrations can reduce the shear-sensitive viscosity of the lubricant. The generated temperature increase is associated with the contact area related power loss.

Also, mixed friction or lubricant contamination, e.g. by water or wear debris, promotes chemical aging of the oil and its additives. As a consequence, the gradually acidifying fluid attacks the steel surface. Tribochemical dissolution of manufacturing related manganese sulfide inclusion lines leaves crack-like defects on the raceway. Further damage evolution by shallow micropitting occurs similar to gray staining that is also caused by, e.g. vibration

induced, mixed friction. Reasons are given for the hypothesis that the crack propagation mechanism is a variant of corrosion fatigue in rolling contact. The material shows indication of in-service (near-) surface embrittlement.

White etching cracks can cause premature bearing failures in specific susceptible applications. The development of heavily branching and widely spreading transcrystalline crack systems at essentially low to moderate mechanical load indicate chemically assisted crack growth by corrosion fatigue under the influence of the penetrating aging lubricant. Released hydrogen locally induces collateral microstructural changes (HELP, DGSL) resulting in the decorating white etching constituents around parts of the crack paths eventually. Surface failure initiation by mixed friction is detected. Shear and tensile stress controlled damage mechanisms are identified. The formation of fatigue microcracks on the surface, comparable with gray staining, and initial crack extension in overrolling direction at a small angle to the raceway tangent are caused by the variation of load and friction-defining slip in the contact area. The characteristic orientation of crack propagation reveals failure promoting shear stresses. The established tribological model also explains competing frictional tensile stress induced failure initiation in rolling-sliding contact. Vertical brittle spontaneous hairline cracking of limited depth and surface length of respectively about 0.1 to 0.2 mm occurs mainly in axial direction on the raceway. The normal stress hypothesis is thus proposed. Illustrative case examples are discussed. Failure metallography, fractography and residual stress analysis are applied. Whereas the circumferential tensile stress in the affected subdomains, referring to the introduced tribological model, must be high (maximum on the surface, $\propto \mu p_0$) to initiate cleavage-like raceway cracks, the contact area related frictional power loss ($\propto \mu p_0 v_s$) is limited so that no smearing (adhesive wear) occurs. This interrelation leads to the conclusion that the rare events of brittle spontaneous raceway cracking in premature bearing failures can be considered as a consequence of specific (three-dimensional) vibration conditions of high Hertzian pressure p_0 and local friction coefficient μ at low sliding speed v_s (*gluing* effect). The shear stress induced inclined flat fatigue-like incipient microcracks, in contrast, are characterized by lower frictional tensile stresses, i.e. smaller μp_0 value (v_s less important). From both of these crack initiation mechanisms, smearing is clearly differentiated by the much higher contact area related power loss.

7. References

Balzar, D. (1999). Voigt Function Model in Diffraction-line Broadening Analysis. In: *Defect and Microstructure Analysis by Diffraction*, R. Snyder, J. Fiala, H.J. Bunge (Eds.), Oxford University Press, Oxford, Great Britain, pp. 94-126

Birnbaum, H.K. & Sofronis, P. (1994). Hydrogen-Enhanced Localized Plasticity − a Mechanism for Hydrogen Related Fracture. *Materials Science and Engineering*, Vol. A176, No. 1/2, pp. 191-202

Böhm, K.; Schlicht, H.; Zwirlein, O. & Eberhard, R. (1975). Nonmetallic Inclusions and Rolling Contact Fatigue. In: *Bearing Steels: The Rating of Nonmetallic Inclusions*, ASTM STP 575, J.J.C. Hoo, P.T. Kilhefner, J.J. Donze (Eds.), American Society for Testing and Materials (ASTM), West Conshohocken, Pennsylvania, USA, pp. 96-113

Böhmer, H.-J.; Hirsch, T. & Streit, E. (1999). Rolling Contact Fatigue Behaviour of Heat Resistant Bearing Steels at High Operational Temperatures. *Material Science and Engineering Technology*, Vol. 30, No. 9, pp. 533-541

Bragg, W.H. & Bragg, W.L. (1913). The Reflection of X-rays by Crystals. *Proceedings of the Royal Society of London*, Vol. 88A, No. 605, pp. 428-438

Broszeit, E.; Heß, F.J. & Kloos, K.H. (1977). Werkstoffanstrengung bei oszillierender Gleitbewegung. *Zeitschrift für Werkstofftechnik*, Vol. 8, No. 12, pp. 425-432

Broszeit E.; Preussler, T.; Wagner, M. & Zwirlein, O. (1986). Stress Hypotheses and Material Stresses in Hertzian Contacts. *Zeitschrift für Werkstofftechnik*, Vol. 17, No. 7, pp. 238-246

Brückner, M.; Gegner, J.; Grabulov, A.; Nierlich, W. & Slycke, J. (2011). Butterfly Formation Mechanisms in Rolling Contact Fatigue. *Proceedings of the 5th International Conference on Very High Cycle Fatigue*, pp. 101-106, C. Berger, H.-J. Christ (Eds.), DVM German Association for Materials Research and Testing, Berlin, Germany, June 28-30, 2011

Ciavarella, M.; Monno, F. & Demelio, G. (2006). On the Dang Van Fatigue Limit in Rolling Contact Fatigue. *International Journal of Fatigue*, Vol. 28, No. 8, pp. 852-863

Dally, J.W. & Riley, W.F. (2005). *Experimental Stress Analysis*, College House, Knoxville, Tennessee, USA

Desimone, H.; Bernasconi, A. & Beretta, S. (2006). On the Application of Dang Van Criterion to Rolling Contact Fatigue. *Wear*, Vol. 260, No. 4-5, pp. 567-572

Fajdiga, G. & Srami, M. (2009). Fatigue Crack Initiation and Propagation under Cyclic Contact Loading. *Engineering Fracture Mechanics*, Vol. 76, No. 9, pp. 1320-1335

Faninger, G. & Wolfstieg, U. (1976). Aufnahmeverfahren, Auswertung der Interferenzlinien und $d_{\varphi\psi}/\varepsilon_{\varphi\psi}$, $\sin^2\psi$-Zusammenhang. *Härterei-Technische Mitteilungen*, Vol. 31, No. 1-2, pp. 13-32

Fougères, R.; Lormand, G.; Vincent, A.; Nelias, D.; Dudragne, G.; Girodin, D.; Baudry, G. & Daguier, P. (2002). A New Physically Based Model for Predicting the Fatigue Life Distribution of Rolling Bearings. In: *Bearing Steel Technology*, ASTM STP 1419, J.M. Beswick (Ed.), American Society for Testing and Materials (ASTM), West Conshohocken, Pennsylvania, USA, pp. 197-212

Furumura, K.; Murakami, Y. & Abe, T. (1993). The Development of Bearing Steels for Long Life Rolling Bearings under Clean Lubrication and Contaminated Lubrication. In: *Creative Use of Bearing Steels*, ASTM STP 1195, J.J.C. Hoo (Ed.), American Society for Testing and Materials (ASTM), West Conshohocken, Pennsylvania, USA, pp. 199-210

Gegner, J. (2006a). Materialbeanspruchungsanalyse und ihre Anwendung auf Prüfstandsversuche zum Oberflächenausfall (Nierlich-Schadensmodus) von Wälzlagern. *Materialwissenschaft und Werkstofftechnik*, Vol. 37, No. 3, pp. 249-259

Gegner, J. (2006b). Post-Machining Thermal Treatment (PMTT) of Hardened Rolling Bearing Steel. *Proceedings of the 4th International Conference on Mathematical Modeling and Computer Simulation of Material Technologies*, Vol. 1, Chap. 2, pp. 66-75, College of Judea and Samaria, Ariel, Israel, September 11-15, 2006

Gegner, J.; Hörz, G. & Kirchheim, R. (1996). Hydrogen Interaction with 0-, 1-, and 2-Dimensional Defects. In: *Hydrogen Effects in Materials*, A.W. Thompson, N.R. Moody (Eds.), TMS The Minerals, Metals and Materials Society, Warrendale, Pennsylvania, USA, pp. 35-46

Gegner, J.; Kuipers, U.; Mauntz, M. (2010). Ölsensorsystem zur Echtzeit-Zustandsüberwachung von technischen Anlagen und Maschinen. *TM Technisches Messen*, Vol. 77, No. 5, pp. 283-292

Gegner, J.; Nierlich, W. & Brückner, M. (2007). Possibilities and Extension of XRD Material Response Analysis in Failure Research for the Advanced Evaluation of the Damage Level of Hertzian Loaded Components. *Material Science and Engineering Technology*, Vol. 38, No. 8, pp. 613-623

Gegner, J. & Nierlich, W. (2008). Operational Residual Stress Formation in Vibration-Loaded Rolling Contact. *Advances in X-ray Analysis*, Vol. 52, pp. 722-731

Gegner, J. & Nierlich, W. (2011a). Mechanical and Tribochemical Mechanisms of Mixed Friction Induced Surface Failures of Rolling Bearings and Modeling of Competing Shear and Tensile Stress Controlled Damage Initiation. *Tribologie und Schmierungstechnik*, Vol. 58, No. 1, pp. 10-21

Gegner, J. & Nierlich, W. (2011b). Hydrogen Accelerated Classical Rolling Contact Fatigue and Evaluation of the Residual Stress Response. *Materials Science Forum*, Vol. 681, pp. 249-254

Gegner, J. & Nierlich, W. (2011c). Sequence of Microstructural Changes during Rolling Contact Fatigue and the Influence of Hydrogen. *Proceedings of the 5th International Conference on Very High Cycle Fatigue*, pp. 557-562, C. Berger, H.-J. Christ (Eds.), DVM German Association for Materials Research and Testing, Berlin, Germany, June 28-30, 2011

Gegner, J.; Schlier, L. & Nierlich, W. (2009). Evidence and Analysis of Thermal Static Strain Aging in the Deformed Surface Zone of Finish-Machined Hardened Steel. *Powder Diffraction*, Vol. 24, No. 2-supplement, pp. 45-50

Gentile, A.J.; Jordan, E.F. & Martin, A.D. (1965). Phase Transformations in High-Carbon, High-Hardness Steels under Contact Loads. *Transactions AIME*, Vol. *233*, No. 6, pp. 1085-1093

Gohar, R. (2001). *Elastohydrodynamics*, Imperial College Press, London, Great Britain

Harada, H.; Mikami, T.; Shibata, M.; Sokai, D.; Yamamoto, A. & Tsubakino, H. (2005). Microstructural Changes and Crack Initiation with White Etching Area Formation under Rolling/Sliding Contact in Bearing Steel. *ISIJ International*, Vol. 45, No. 12, pp. 1897-1902

Harris, T.A. (2001). *Rolling Bearing Analysis*, Wiley, New York, USA

Hauk, V. & Wolfstieg, U. (1976). Röntgenographische Elastizitätskonstanten. *Härterei-Technische Mitteilungen*, Vol. 31, No. 1-2, pp. 38-42

Hauk, V.M. & Macherauch, E. (1984). A Useful Guide for X-ray Stress Evaluation (XSE). *Advances in X-ray Analysis*, Vol. 27, pp. 81-99

Hauk, V.M., (Ed.), (1997). *Structural and Residual Stress Analysis by Nondestructive Methods – Evaluation, Application, Assessment*, Elsevier, Amsterdam, The Netherlands

Hiraoka, K.; Nagao, M. & Isomoto, T. (2006). Study on Flaking Process in Bearings by White Etching Area Generation. *Journal of ASTM International*, Vol. 3, No. 5, Paper ID JAI14059

Holweger, W. & Loos, J. (2011). Interaction of Rolling Bearing Fatigue Life with New Material Phenomenons of Special Applications. *Proceedings of the 14th Heavy Drive Train Conference*, pp. 223-238, G. Jacobs, K. Hameyer, C. Brecher (Eds.), Apprimus, Aachen, Germany, RWTH Aachen University, Aachen, Germany, March 29-30, 2011

Hooke, C.J. (2003). Dynamic Effects in EHL Contacts. In: *Tribological Research and Design for Engineering Systems*, D. Dowson, A.A. Lubrecht, M. Priest (Eds.), Tribology Series, Vol. 41, Elsevier, Amsterdam, The Netherlands, pp. 69-78, Proceedings of the 29th Leeds-Lyon Symposium on Tribology, Leeds, Great Britain, September 03-06, 2002

Ioannides, E. & Harris, T.A. (1985). A New Fatigue Life Model for Rolling Bearings. *ASME Journal of Tribology*, Vol. 107, No. 3, pp. 367-378

Iso, K.; Yokouchi, A. & Takemura, H. (2005). Research Work for Clarifying the Mechanism of White Structure Flaking and Extending the Life of Bearings. In: *Engine Lubrication and Bearing Systems*, SAE SP-1967, Paper No. 2005-01-1868, Society of Automotive Engineers (SAE), SAE International, Warrendale, Pennsylvania, USA

Jagenbrein, A.; Buschbeck, F.; Gröschl, M. & Preisinger, G. (2005). Investigation of the Physical Mechanisms in Rolling Bearings during the Passage of Electric Current. *Tribotest*, Vol. 11, No. 4, pp. 295-306

Jatckak, C.F. & Larson, J.A. (1980). *Retained Austenite and Its Measurement by X-ray Diffraction*, SAE SP-453, Society of Automotive Engineers (SAE), Warrendale, Pennsylvania, USA

Johnson, K.L. & Jefferis, J.A. (1963). Plastic Flow and Residual Stresses in Rolling and Sliding Contact. *Proceedings of the Institute of Mechanical Engineers*, Vol. 177, No. 25, pp. 54-65

Johnson, K.L. (1985). *Contact Mechanics*, Cambridge University Press, Cambridge, Great Britain

Jones, A.B. (1946). Effect of Structural Changes in Steel on Fatigue Life of Bearings. *Steel*, Vol. 119, No. 9, pp. 68-70 and 97-100

Karas, F. (1941). Die äußere Reibung beim Walzendruck. *Forschung auf dem Gebiet des Ingenieurwesens*, Vol. 12, No. 6, pp. 266-274

Kino, N. & Otani, K. (2003). The Influence of Hydrogen on Rolling Contact Fatigue Life and its Improvement. *JSAE Review*, Vol. 24, No. 3, pp. 289-294

Kohara, M.; Kawamura, T. & Egami, M. (2006). Study on Mechanism of Hydrogen Generation from Lubricants. *Tribology Transactions*, Vol. 49, No. 1, pp. 53-60

Kotzalas, M.N. & Doll, G.L. (2010). Tribological Advancements for Reliable Wind Turbine Performance. *Philosophical Transactions of the Royal Society A*, Vol. 368, No. 1929, pp. 4829-4850

Kudish, I.I. & Covitch, M.J. (2010). *Modeling and Analytical Methods in Tribology*, Chapman and Hall, CRC Press, Boca Raton, Florida, USA

Lindahl, E. & Österlund, R. (1982). 21/2D Transmission Electron Microscopy Applied to Phase Transformations in Ball Bearings. *Ultramicroscopy*, Vol. 9, No. 4, pp. 355-364

Lundberg, G. & Palmgren, A. (1947). *Dynamic Capacity of Roller Bearings*, Acta Polytechnica, Mechanical Engineering Series, Vol. 1, No. 3, Royal Swedish Academy of Engineering Sciences, Stockholm, Sweden

Lundberg, G. & Palmgren, A. (1952). *Dynamic Capacity of Roller Bearings*, Acta Polytechnica, Mechanical Engineering Series, Vol. 2, No. 4, Royal Swedish Academy of Engineering Sciences, Stockholm, Sweden

Luyckx, J. (2011). WEC Failure Mode on Roller Bearings: From Observation via Analysis to Understanding and a Solution. *Proceedings of the VDI Symposium Gleit- und Wälzlagerungen: Gestaltung, Berechnung, Einsatz*, VDI-Berichte 2147, VDI Wissensforum, Düsseldorf, Germany, pp. 31-42, Schweinfurt, Germany, May 24-25, 2011

Macherauch, E. & Müller, P. (1961). Das $\sin^2\psi$-Verfahren der röntgenographischen Spannungsmessung. *Zeitschrift für angewandte Physik*, Vol. 13, No. 7, pp. 305-312

Macherauch, E. (1966). X-ray Stress Analysis. *Experimental Mechanics*, Vol. 6, No. 3, pp. 140-153

Martin, J.A.; Borgese, S.F. & Eberhardt, A.D. (1966). Microstructural Alterations in Rolling Bearing Steel Undergoing Cyclic Stressing. *Transactions ASME Journal of Basic Engineering*, Vol. 88, No. 3, pp. 555-567

Marx, K.-W. (1966). *Röntgenographische Eigenspannungsmessungen an einem gehärteten und angelassenen Wälzlagerstahl 100 Cr Mn 6*, Thesis, Aachen University of Technology, Aachen, Germany

Muro, H. & Tsushima, N. (1970). Microstructural, Microhardness and Residual Stress Changes due to Rolling Contact. *Wear*, Vol. 15, No. 5, pp. 309-330

Muro, H.; Tsushima, N.; Nunome, K. (1973). Failure Analysis of Rolling Bearings by X-ray Measurement of Residual Stress. *Wear*, Vol. 25, No. 3, 1973, pp. 345-356

Nierlich, W.; Brockmüller, U. & Hengerer, F. (1992). Vergleich von Prüfstand- und Praxisergebnissen an Wälzlagern mit Hilfe von Werkstoffbeanspruchungsanalysen. *Härterei-Technische Mitteilungen*, Vol. 47, No. 4, pp. 209-215

Nierlich, W. & Gegner, J. (2002). Material Response Analysis of Rolling Bearings Using X-ray Diffraction Measurements. *Proceedings of the Materials Week 2001, International Congress on Advanced Materials, their Processes and Applications*, CD-ROM, Paper No. 413, Werkstoffwoche-Partnerschaft, Frankfurt, ISBN 3-88355-302-6, Munich, Germany, October 1-4, 2001

Nierlich, W. & Gegner, J. (2006). Material Response Models for Sub-Surface and Surface Rolling Contact Fatigue. *Proceedings of the 4th International Conference on Mathematical Modeling and Computer Simulation of Material Technologies*, Vol. 1, Chap. 1, pp. 182-192, College of Judea and Samaria, Ariel, Israel, September 11-15, 2006

Nierlich, W. & Gegner, J. (2008). X-ray Diffraction Residual Stress Analysis: One of the Few Advanced Physical Measuring Techniques that have Established Themselves for Routine Application in Industry. *Advances in Solid State Physics*, Vol. 47, pp. 301-314

Nierlich, W. & Gegner, J. (2011). Einführung der Normalspannungshypothese für Mischreibung im Wälz-Gleitkontakt. *Proceedings of the VDI Symposium Gleit- und Wälzlagerungen: Gestaltung, Berechnung, Einsatz*, VDI-Berichte 2147, VDI Wissensforum, Düsseldorf, Germany, pp. 277-290, Schweinfurt, Germany, May 24-25, 2011

Noyan, I.C. & Cohen, J.B. (1987). *Residual Stress – Measurement by Diffraction and Interpretation*, Springer, New York, New York, USA

Olver, A.V. (2005). The Mechanism of Rolling Contact Fatigue: An Update. *Proceedings of the Institution of Mechanical Engineers, Part J Journal of Engineering Tribology*, Vol. 219, No. 5, pp. 313-330

Österlund, R.; Vingsbo, O.; Vincent, L. & Guiraldenq, P. (1982). Butterflies in Fatigued Ball Bearings - Formation Mechanisms and Structure. *Scandinavian Journal of Metallurgy*, Vol. 11, No. 1, pp. 23-32

Palmgren, A. (1964). *Grundlagen der Wälzlagertechnik*, Franckh, Stuttgart, Germany, 1964

Prashad, H. (2006). *Tribology in Electrical Environments*, Elsevier, Amsterdam, The Netherlands

Rollmann, J. (2000). *Wälzfestigkeit von induktiv randschichtgehärteten bauteilähnlichen Proben*, Thesis, Darmstadt University of Technology, Shaker, Aachen, Germany

Schlicht, H. (2008). Über adiabatic shearbands und die Entstehung der „Steilen Weißen Bänder" in Wälzlagern. *Materialwissenschaft und Werkstofftechnik*, Vol. 39, No. 3, pp. 217-226

Schlicht, H.; Schreiber, E. & Zwirlein, O. (1987). Ermüdung bei Wälzlagern und deren Beeinflussung durch Werkstoffeigenschaften. *Wälzlagertechnik*, No. 1, pp. 14–22

Schlicht, H.; Schreiber, E. & Zwirlein, O. (1988). Effects of Material Properties on Bearing Steel Fatigue Strength. In: *Effect of Steel Manufacturing Processes on the Quality of Bearing Steels*, ASTM STP 987, J.J.C. Hoo (Ed.), American Society for Testing and Materials (ASTM), West Conshohocken, Pennsylvania, USA, pp. 81-101

Schreiber, E. (1992). Analyse realer Beanspruchungsverhältnisse im Wälzkontakt. In: *Randschichtermüdung im Wälzkontakt*, F. Hengerer (Ed.), Association for Heat Treatment and Materials Technology (AWT), Wiesbaden, Germany, pp. 35-51

Shibata, M.; Gotoh, M.; Oguma, N. & Mikami, T. (1996). A New Type of Micro-Structural Change due to Rolling Contact Fatigue on Bearings for the Engine Auxiliary Devices. *Proceedings of the International Tribology Conference*, Vol. 3, pp. 1351-1356, Japanese Society of Tribologists, Tokyo, Japan, Yokohama, Japan, October 29-November 2, 1995

Shiga, T.; Umeda, A. & Ihata, K. (2006). *Method and Apparatus for Designing Rolling Bearing to Address Brittle Flaking*, United States Patent, Assignee: Denso Corporation, Publication No.: US 2006/0064197 A1, Publication Date: March 23, 2006

Swahn, H.; Becker, P.C. & Vingsbo, O. (1976a). Martensite Decay during Rolling Contact Fatigue in Ball Bearings. *Metallurgical Transactions A*, Vol. 7A, No. 8, pp. 1099-1110

Swahn, H.; Becker, P.C. & Vingsbo, O. (1976b). Electron Microscope Studies of Carbide Decay during Contact Fatigue in Ball Bearings. *Metal Science*, Vol. 10, No. 1, pp. 35-39

Takemura, H. & Murakami, Y. (1995). Rolling Contact Fatigue Mechanism (Elasto-plastic Analysis around Inclusion). In: *Fatigue Design 1995*, G. Marquis, J. Solin (Eds.), VTT Manufacturing Technology, Espoo, Finland, pp. 345-356

Vincent, A.; Lormand, G.; Lamagnère, P.; Gosset, L.; Girodin, D.; Dudragne, G. & Fougères, R. (1998). From White Etching Areas Formed around Inclusions to Crack Nucleation in Bearing Steels under Rolling Contact Fatigue. In: *Bearing Steels: Into the 21st Century*, ASTM STP 1327, J.J.C. Hoo, W.B. Green (Eds.), American Society for Testing and Materials (ASTM), West Conshohocken, Pennsylvania, USA, pp. 109-123

Voskamp, A.P. (1985). Material Response to Rolling Contact Loading. *ASME Journal of Tribology*, Vol. 107, No. 3, pp. 359-366

Voskamp, A.P. (1987). Rolling Contact Fatigue and the Significance of Residual Stresses. In: *Residual Stresses in Science and Technology*, Vol. 2, E. Macherauch, V.M. Hauk (Eds.), Deutsche Gesellschaft für Metallkunde (DGM) Informationsgesellschaft, Oberursel, Germany, pp. 713-720

Voskamp, A.P. (1996). *Microstructural Changes during Rolling Contact Fatigue – Metal Fatigue in the Subsurface Region of Deep Groove Ball Bearing Inner Rings*, Thesis, Delft University of Technology, Delft, The Netherlands

Voskamp, A.P. (1998). Fatigue and Material Response in Rolling Contact. In: *Bearing Steels: Into the 21st Century*, ASTM STP 1327, J.J.C. Hoo, W.B. Green (Eds.), American Society for Testing and Materials (ASTM), West Conshohocken, Pennsylvania, USA, pp. 152-166

Wielke, B. (1974). Hysteresis Loop of an Elastic-Plastic $\lambda/2$ Oscillator. Physica Status Solidi, Vol. 23, No. 1, pp. 237-244

Yhland, E. (1983). Statische Tragfähigkeit – Shakedown. Kugellager-Zeitschrift, Vol. 56, No. 211, pp. 1-8

Yoshioka, T. (1992). Acoustic Emission and Vibration in the Process of Rolling Contact Fatigue (4th Report): Measurement of Propagation Initiation and Propagation Time of Rolling Contact Fatigue Crack. Japanese Journal of Tribology, Vol. 37, No. 2, pp. 205-217

Yoshioka, T. & Fujiwara, T. (1988). Measurement of Propagation Initiation and Propagation Time of Rolling Contact Fatigue Cracks by Observation of Acoustic Emission and Vibration. In: Interface Dynamics, D. Dowson, C.M. Taylor, M. Godet, D. Berthe (Eds.), Tribology Series, Vol. 12, Elsevier, Amsterdam, The Netherlands, pp. 29-33, Proceedings of the 14th Leeds-Lyon Symposium on Tribology, Lyon, France, September 08-11, 1987

Zika, T.; Buschbeck, F.; Preisinger, G. & Gröschl, M. (2007). Electric Erosion − Current Passage through Bearings in Wind Turbine Generators. *Proceedings of the 6th Chinese Electrical Machinery Development Forum,* pp. 85-99, Shanghai, China, October 10, 2007

Zika, T.; Gebeshuber, I.C.; Buschbeck, F.; Preisinger, G. & Gröschl, M. (2009). Surface Analysis on Rolling Bearings after Exposure to Defined Electric Stress. *Proceedings of the Institution of Mechanical Engineers, Part J: Journal of Engineering Tribology*, Vol. 223, No. 5, pp. 778-787

Zika, T.; Buschbeck, F.; Preisinger, G.; Gebeshuber, I.C. & Gröschl, M. (2010). Surface Damage of Rolling Contacts Caused by Discrete Current Flow. *Tribologie und Schmierungstechnik,* Vol. 57, No. 3, pp. 11-14
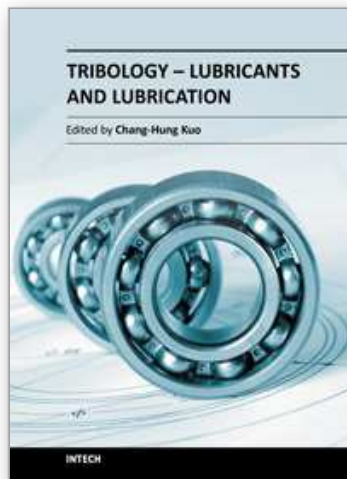
Tribology - Lubricants and Lubrication

Edited by Dr. Chang-Hung Kuo

In the past decades, significant advances in tribology have been made as engineers strive to develop more reliable and high performance products. The advancements are mainly driven by the evolution of computational techniques and experimental characterization that leads to a thorough understanding of tribological process on both macro- and microscales. The purpose of this book is to present recent progress of researchers on the hydrodynamic lubrication analysis and the lubrication tests for biodegradable lubricants.

How to reference

In order to correctly reference this scholarly work, feel free to copy and paste the following:

Jürgen Gegner (2011). Tribological Aspects of Rolling Bearing Failures, Tribology - Lubricants and Lubrication, Dr. Chang-Hung Kuo (Ed.), ISBN: 978-953-307-371-2, InTech, Available from: http://www.intechopen.com/books/tribology-lubricants-and-lubrication/tribological-aspects-of-rolling-bearing-failures

INTECH
open science | open minds